Water Cooling for the Frontend Electronics and a modular Phase Separator for the COMPASS Silicon Detectors and Alignment for the 2012 Primakoff Run

Diploma Thesis
by
Bernd Holzgartner

Physik Department E18
Technische Universität München

Abstract

The COMPASS experiment at CERN uses silicon microstrip detectors for beam definition and vertex reconstruction. Since 2009, the detectors are operated at cryogenic temperatures to minimize radiation damage. This thesis describes the development of a new, modular phase separator for the liquid nitrogen cooling system of the detector modules as well as the construction and the commissioning of a water cooling system for the frontend electronics of these detectors. In addition, results of the alignment studies for the 2012 Primakoff run are presented.

Contents

List of Figures

List of Tables

1. Introduction

COMPASS[1] is a high-luminosity fixed-target experiment at the SPS accelerator[2] at CERN[3], Geneva. The physics programs, the spectrometer design as well as the analysis tools are presented in Chapter 2.

For most physics issues, the experiment relies heavily on silicon microstrip detectors, as they are used for beam definition in muon and hadron programms and furthermore for vertex definition in hadron programs. The design and the commissioning of the COMPASS silicon microstrip detectors are described in Chapter 3.

Chapter 4 gives a brief motivation for the development of an improved phase separator for the liquid nitrogen cooling system of the silicon microstrip detectors. After this introduction to the topic, the design principles and the progress of prototype testing are presented.

As the frontend electronics of the detector system needs to be cooled as well, a water cooling system for the repeater cards of the silicon microstrip detectors is presented in Chapter 5. At the beginning of this chapter, the needs and requirements for a front-end cooling system are introduced and based thereupon, the design of the system is described. The chapter concludes with an overview of the performance of the cooling system throughout the operational time during the 2012 Primakoff run at COMPASS.

The measurement of pion polarizabilities via the Primakoff effect demands a precise spectrometer alignment. Chapter 6 introduces the COMPASS alignment procedure and presents results of the performed alignment.

[1] **CO**mmon **M**uon and **P**roton **A**pparatus for **S**tructure and **S**pectroscopy
[2] **S**uper **P**roton **S**ynchrotron
[3] **C**onseil **E**uropéen pour la **R**echerche **N**ucléaire - European Organization for Nuclear Research

2. The Compass experiment

In addition to the four large experiments ALICE[4], ATLAS[5],CMS[6] and LHCb[7] located at the world's highest-performance accelerator LHC[8] at CERN, there are several other big experiments currently taking data. One of them is the COMPASS experiment [1], a high-luminosity, fixed-target experiment situated in the CERN North Area. Muon and hadron beams are used to study a wide field of physics from nucleon spin structure to hadron spectroscopy. In this chapter, the physics program as well as the various spectrometer configurations, depending on the physics to be investigated, are presented. At the end of this chapter, attention is drawn to the COMPASS analysis chain.

2.1. Site

Founded in 1954, CERN was intended to study fundamental physics. With physics developping, the attention of CERN's experiments moved from the reaserach of nuclear and atomar structure via the examination of the nuclei's constituents over to the investigation of today's most fundamental particles known. Pushing the limits of technology and focussing on smaller and smaller consituents of matter, the number and the ability of accelarators increased accordingly. Today, CERN is running eight accelarators (Fig. 2.1), including the LHC and the SPS, to which the COMPASS experiment is connected via the M2 beamline.

2.2. The COMPASS physics programm

As acronym COMPASS already tells us, the spectrometer was designed for two different physics programms, nucleon structure and hadron spectroscopy [3]. These two programms are distinguished mainly by the type of incoming beam particles used. For understanding the various configurations of the spectrometer, one needs to know the physics goals of COMPASS.

[4]**A** **L**arge **I**on **C**ollider **E**xperiment
[5]**A** **T**oroidal **L**HC **A**pparatu**S**
[6]**C**ompact **M**uon **S**olenoid
[7]**L**arge **H**adron **C**ollider **b**eauty
[8]**L**arge **H**adron **C**ollider

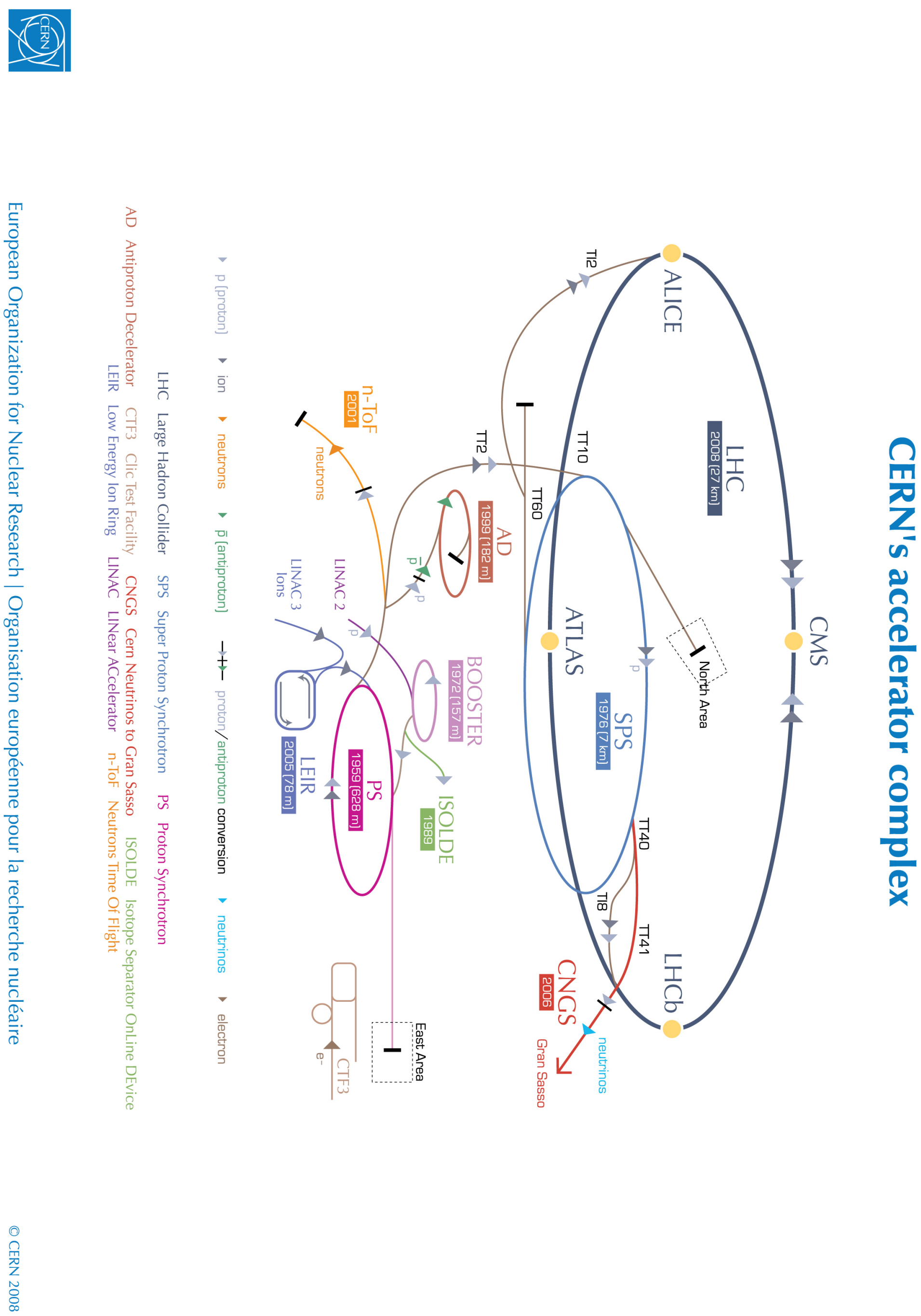

Figure 2.1.: The CERN accelerator chain [2]

2.2.1. Physics with muon beams

- **Gluon Polarization**
  The QPM[9] describes the total spin of a nucleon like

$$\tfrac{1}{2} = \tfrac{1}{2}\Delta\Sigma + \Delta G + L_q + L_G,$$

where $\Delta\Sigma$ is the sum of all quark and anti-quark spins, ΔG is the contribution of the gluon spin and $L_{q,G}$ is the orbital angular momentum of the quarks and gluons respectively. The QPM predicts that the quarks carry 60 % of the nucleon spin [4]. But several experiments, beginning with the EMC[10], observed that only a fraction of the nucleon spin is actually carried by the quarks [4]. The experiments observed a quark contribution of $\sim$ 33 %. ΔG was expected to contribute part of the missing nucleon spin and its determination was one of the main goals of COMPASS.

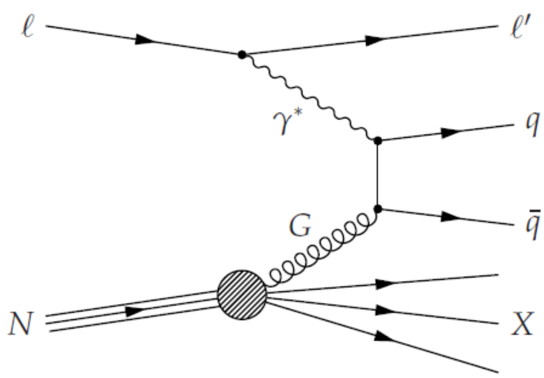

Figure 2.2.: The Feynman diagramm for a PGF [5]

As the virtual photon is not able to interact directly with the gluons in the target nucleon, at least second order processes are necessary. One such process is the PGF[11] process $\gamma^* G \to q\overline{q}$ (see Fig. 2.2) where the virtual photon interacts with the gluon by way of an intermediate quark line. It allows to access the gluon polarization $\Delta G/G$ via the measurement of the cross section helicity asymmetries. In the experiment, the PGF processes must be selected by the final state, thus a semi-inclusive measurement is obligatory. COMPASS provides two approaches for the gluon polarization measurement:

  - **Open Charm**
    The, produced $q\overline{q}$ pair is a $c\overline{c}$ pair and one of the charm quarks fragments into a D meson.

[9] **Q**uark-**P**arton **M**odel
[10] **E**uropean **M**uon **C**ollaboration
[11] **P**hoton-**G**luon **F**usion

  - **High p_t**
    Events with two hadrons at high transverse momentum p_t.

- **Longitudinal spin structure**
  With semi-inclusive measurements of DIS[12] of a polarised muon beam (in general of polarised leptons) off a longitudinally polarized deuteron target, one is able to study the deuteron longitudinal spin asymmetry A_1^d and the deuteron's spin dependent structure function g_1^d [6, 7]. High precision measurement of g_1^d allows to determine the quark contribution to the nucleon spin [8]: $\Delta\Sigma = 0.33 \pm 0.03(stat) \pm 0.05(sys)$. Furthermore, COMPASS was able to determine polarised valence quark distributions [9] and flavour seperated helicity distributios [10].

- **Transverse spin structure**
  Determining the single spin asymmetries for semi-inclusive DIS of leptons on transversely polarised nucleons[13] by detecting the hadron with highest momentum originating from the extraction vertex allows to study the Collins and Sivers mechanisms.

  In COMPASS, the Collins and Sivers asymmetries for outgoing pions and kaons on a polarised deuterium target have been measured. The determined asymmetries are small and compatible with zero within the error margins [11, 12]. In measurements on a proton target, non-zero Collins asymmetries for large values of the Bjorken variable x and positive Sivers asymmetries for positive hadrons over almost the measured x range were observed [13, 14].

- **Generalized Parton Distributions**
  GPDs[14] are an ansatz to gather information about the angular momentum of partons by combining parton distributions and elastic form factors of a hadron. In DVCS[15], a high-energetic photon which is almost on mass-shell, scatters off a parton. This allows access to these distributions as the virtual photon becomes real due to the small momentum transfer. With DVMP[16], a complementary measurement to cover different linear combinations of GPDs is provided.

- **Λ and $\overline{\Lambda}$ Polarization**
  The simplest way to produce a polarized Λ is to scatter an unpolarized muon off a unpolarized target. The polarization relates to the hadronization process and is not yet fully understood. COMPASS, with its beam and target both polarized, is able to study the dynamics of the spin transfer from partons to Λ hyperons [5].

[12] **D**eeply **I**nelastic **S**cattering
[13] with respect to the beam polarisation
[14] **G**eneralized **P**arton **D**istribution
[15] **D**eeply **V**irtual **C**ompton **S**cattering
[16] **D**eeply **V**irtual **M**eson **P**roduction

2.2.2. Physics with hadron beams

- **Primakoff reactions**
  In a Primakoff reaction, a high energetic hadron scatters off the Coulomb field of a target nucleus and a hard photon is emitted:

$$\pi^- Z \to \pi^- Z\gamma \tag{2.1}$$

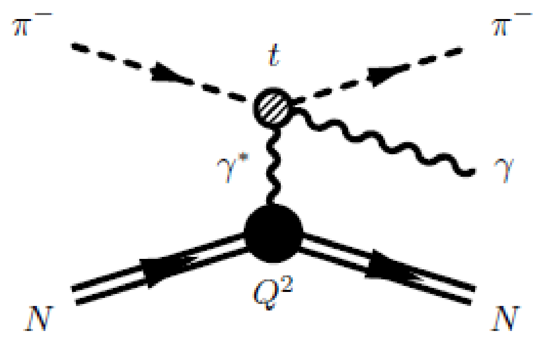

Figure 2.3.: The Feynman diagramm for a Primakoff reaction [15]

In COMPASS the electric and magnetic polarisabilities of the pion are measured via the Primakoff effect, where the production of the real photon is conform to pion Compton scattering with inverse kinematics and is thus sensitive to the pion polarisabilities. By measuring these quantities, one is able to test predictions made by ChPT[17]. From 2009 data, COMPASS determined the pion polarisability to $\alpha_\pi = -\beta_\pi = 1.9 \pm 0.7_{stat} \pm 0.8_{syst} \times 10^{-4}\,\mathrm{fm}^3$ [16], which is in conformity with the ChPT prediction.

Apart from Primakoff Compton scattering reactions with a photon in the final state, COMPASS allows for the measurement of Primakoff reactions with charged or neutral mesons in the final state:

$$\pi^- Z \to \pi^- Z\pi^+\pi^- \tag{2.2}$$
$$\pi^- Z \to \pi^- Z\pi^0 \tag{2.3}$$
$$\pi^- Z \to \pi^- Z\pi^0\pi^0 \tag{2.4}$$
$$\pi^- Z \to \pi^- Z\eta \tag{2.5}$$

After a pilot run in 2004 and a 2-week Primakoff run in 2009, a high-statistics measurement aiming at a precision measurement of the pion polarisabilities was

[17] **Ch**iral **P**erturbation **T**heory

performed in 2012. Moreover similar reactions as in equations 2.1 to 2.5 are accessible induced by Kaons, e.g. COMPASS attempts a first measurement of the electromagnetic polarisability of the charged kaon, using CEDARs[18] to identify the kaons [17].

- **Exotic states**
  The constituent quark model describes mesons as $q\overline{q}$ states and and baryons as qqq states. In QCD[19], these are just the most simple bound states for quarks. The theory provides a much wider range of possible states, the so called exotic states, which can no longer be described by the simple constituent quark model.

  One of these predicted exotic states is the glueball, a bound state made entirely of gluons without any valence quarks. LQCD[20] predicts a lowest glueball mass within a range of 1.5 to 1.8 GeV/c^2 for a $\mathrm{J}^{\mathrm{PC}} = 0^{++}$ state. It is possible to identify these exotics via their production characteristics, their decay patterns and by their relation to other mesons having identical parity- and spin-quantum numbers.

  Another of these exotics are the so called hybrids ($qg\overline{q}$), a mesonic system ($q\overline{q}$) coupled to excitations of the gluon string binding q and $\overline{q}$. To separate these states from mesonic states, one has to investigate quantum number combinations which are not allowed for $q\overline{q}$ systems made up of the three light quarks.

  Other even more exotic predicted states are tetraquarks ($qq\overline{q}\overline{q}$), pentaquarks ($qqqq\overline{q}$) or hexaquarks ($qqqqqq$ or $qqq\overline{q}\overline{q}\overline{q}$). These states, predicted by theory and claimed by respective experiments [18, 19, 20], are still under discussion [21, 22].

  For each of the states mentioned above, it is fundamental to know the energy regions around the desired states to be able to factor the exotic signals out of the recorded data. COMPASS is able to investigate charged exotic states via diffractive scattering and neutral exotic states by way of central production mechanism and photo-production. Determining the quantum numbers of the observed states is challenging and done by PWA[21], i.e. fragmenting observed angular distributions into partial waves and thus identifying resonances (see e.g. [5, 22]).

- **Drell-Yan muon pair production**
  A Drell-Yan reaction describes the annihilation of a quark and an antiquark from beam and target particles into a virtual photon or a Z-boson, decaying into two leptons [17]. With this process PDF[22]s of hadrons can be investigated and, in

[18] **Ch**__E__erenkov **D**ifferential counter with **A**chromatic **R**ing focus
[19] **Q**antum **C**hromo **D**ynamics
[20] **L**attice **Q**antum **C**hromo **D**ynamics
[21] **P**artial **W**ave **A**nalysis
[22] **P**arton **D**istribution **F**unction

combination with the polarized target of COMPASS, also spin dependent effects can be studied.

2.3. The COMPASS spectrometer

COMPASS is a fixed target experiment and requires high luminosity and high statistics. To achieve the requirement of high luminosity, the experimental set-up needs a high data rate capability, particle identification and a wide angular as well as momentum acceptance. Furthermore, precise kinematic reconstruction of events and good mass resolution are essential. The necessary high statistics is obtained one the hand via beam rates in the order of 10^7 - 10^8 particles per SPS cycle and on the other hand through high trigger rates up to 30 kHz. High precision is provided through the two stage spectrometer (see Fig. 2.4).

The COMPASS spectrometer can be divided into three regions:

- region upstream of the target
- Large Angle Spectrometer (LAS)
- Small Angle Spectrometer (SAS)

In the region upstream of the target, the BMS[23] is located in the final part of the beam line (details of the beam line are described in section 2.3.1). For the BMS a bending magnet of the beam line is used to measure the momentum of the incoming particles. It is only used for muon beams because of its material budget. For hadron beams, two CEDARs are used to tag kaons in the pion beam. A beam telescope, consisting of three silicon detector stations, is utilized for beam definition. In case of a muon beam, the silicon detectors are combined with two SciFi[24] stations. In addition to the aforementioned detectors, several trigger and trigger veto detectors are placed upstream of the target to ensure triggering on nothing else but beam particles.

The LAS is arranged downstream of and close to the target. It covers a momentum range of roughly $1 - 20$ GeV and has a polar acceptance of 180 mrad. The center of the LAS is a dipole magnet (SM1) with a field integral of 1 Tm, which is sandwiched by tracking detectors. The RICH[25] is placed successive to identify charged hadrons with momenta of several ten GeV/c. The RICH is followed by a first electromagnetic calorimeter (ECAL1) and a first hadronic calorimeter (HCAL1). The LAS is concluded by a muon filter (MW1).

[23]**B**eam **M**omentum **S**tation
[24]**Sci**ntillating **Fi**ber
[25]**R**ing **I**maging **CH**erenkov detector

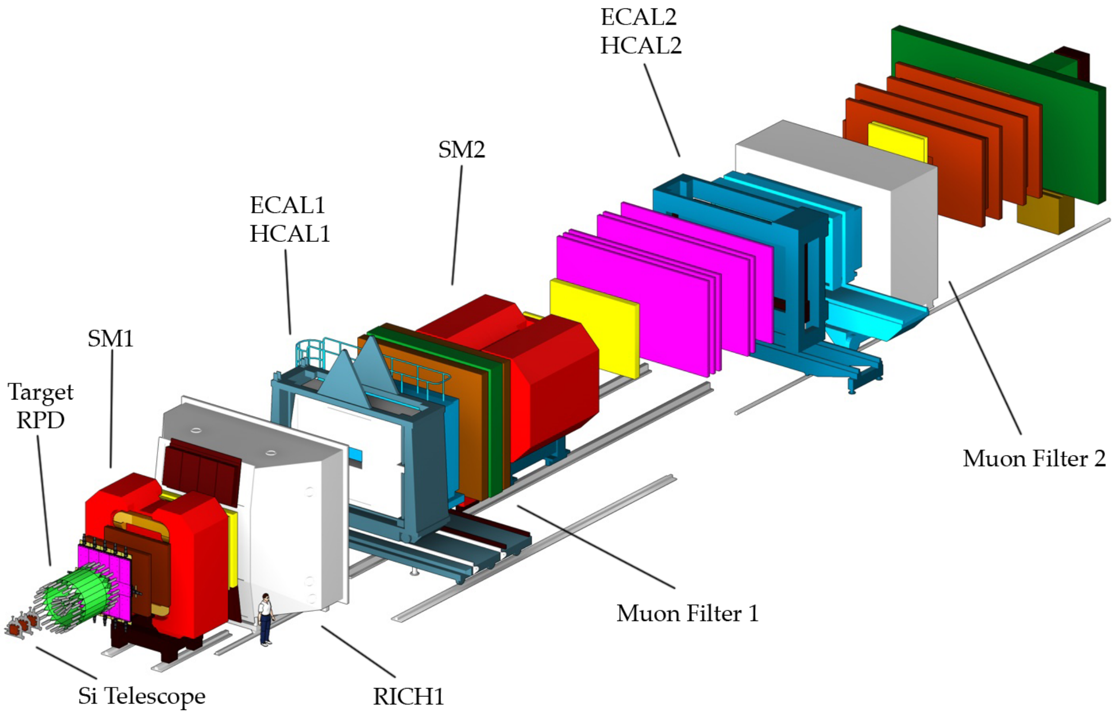

Figure 2.4.: 3D view of the COMPASS spectrometer (2008/09 hadron set-up) [23]

The LAS is followed by the SAS to detect particles within an angle of 30 mrad (with respect to the beam direction) and momenta above 5 GeV/c. The SAS has almost the same configuration as the LAS. The SAS's center is a second dipole magnet (SM2) with a field integral of 4.4 Tm, which is again sandwiched by tracking detectors. There is no RICH in the SAS, thus the tracking detectors are directly followed by the secondary electromagnetic (ECAL2) and hadronic calorimeters (HCAL2). Further downstream, another muon filter, trigger hodoscopes and muon detectors are placed. The whole assembly is completed by a beam dump to absorb the remaining beam particles. Due to the scarce muon absorption of the beam dump, the muons can leave the experimental hall and enter the surrounding ground.

2.3.1. The M2 beam line

As already mentioned, the COMPASS experiment is connected to the SPS via the M2 beamline. The schematic of the M2 beamline is shown in Fig. 2.5. A primary beam of 400 GeV/c Protons, coming from the SPS, impinges on the T6 production target (labeled "50 cm Be Target" in Fig. 2.5), consisting of berrylium rods of different lengths. Per 30−45 s super-cycle, a 9.6 s beam spill is provided to the experimental hall of COMPASS.

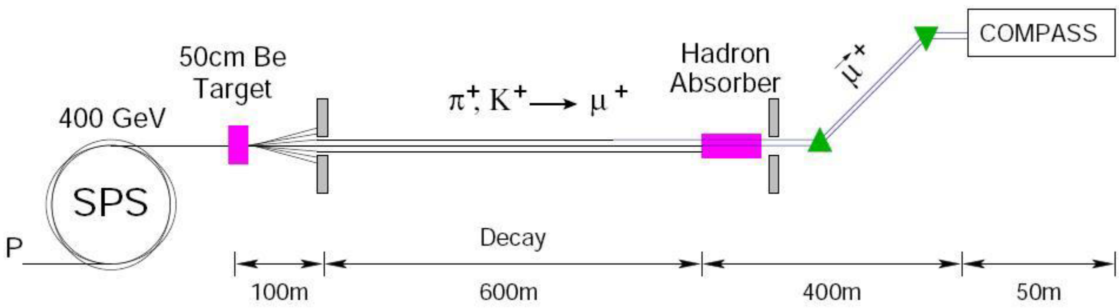

Figure 2.5.: The M2 beamline schematics (muon set-up) [24]

The produced secondary particles, mostly hadrons (π^+ and K^+ in Fig. 2.5), are following a roughly one km long beamline containing a variety of bending magnets, absorbers, collimators and focusing quadrupol magnets and get focused onto the COMPASS experiment.

This beam mainly consisting of pions with a mixture of kaons and (anti-)protons is the source for the muon respectively hadron beam with which the experiment is run.

- The muon beam consists of muons created by the decay of pions along the 600 m long decay line. In addition to that the remaining hadrons are stopped by another 9.9 m long berrylium absorber after the decay line. With this set-up a beam with a nominal beam momentum of 160 GeV/c and a flux of $2 \cdot 10^8$ muons per SPS cycle is provided.

- The hadron beam can either be chosen negatively charged or positively charged. Thus consisting of mostly π^- and a fraction of K^- and $\overline{p}$ or respectively mainly p with a fraction of π^+ and K^+. In both cases electrons are present at the few percent level. The beam momentum is up to 225 GeV/c with a flux of several 10^7 hadrons per SPS cycle. For the 2012 Primakoff program a momentum of 190 GeV/c with a flux of $5 \cdot 10^7$ hadrons per spill is chosen.

- An electron beam is also available for the calibration of the electromagnetic calorimeters. It is produced by focusing low energy particles ($<$ 100 GeV) on a lead converter target. The nominal momentum of the electron beam can be chosen $15 - 40$ GeV/c with a flux up to several $\sim 10^3$ electrons per SPS cycle.

2.3.2. Target

As said prior to this, COMPASS studies different fields of physics and uses different types of beams for this investigations. These matters of fact also affect the targets which are used.

When using muon beams, effects depending on the spin configuration are measured. Therefore,it is necessary to polarize the target. Deuterons (^{6}LiD) or protons (NH_3) are employed as target material. As nuclei cannot be polarized in a direct manner, one has to polarize the electrons and transfer their polarization by a microwave field. Hence, it is essential to operate at temperatures below 1 K and to apply a strong and homogeneous magnetic field. The polarized target at COMPASS therefore uses a longitudinal magnetic field of 2.5 T with transverse holding field of 0.42 T over a cylindrical region of 50 mm in diameter and 1500 mm in length. Thus, a homogeneity of better than 20 ppm is achieved. Adequate temperature is provided by a ^{3}He/^{4}He dilution refrigerator which has the ability to reach temperatures below 90 mK.

For hadronic runs, liquid hydrogen targets are used. In addition to that, the target is surrounded by a RPD[26], detecting the recoiling proton. It consists of two layers of scintillators arranged inside a metal barrel of 1620 mm in diameter. For Primakoff studies, thin targets with a thickness of ~ 0.3 radiation lengths are needed. Thus, nickel discs of different thickness, placed in a target support assembly, are used. For the measurement of the π^0 lifetime, tungsten foils are used. Diffractive measurements are done with a carbon target foil.

2.3.3. Tracking

Measuring the path of charged particles through the spectrometer is done by tracking detectors. These detectors can be classified into three groups.

- **Very Small Area Trackers (VSAT)**
  These detectors are used for a precise beam definition and for vertex detection. In COMPASS SciFis and silicon detectors are used, as they provide an excellent spatial resolution ($< 10\,\mu$m for silicons) and an accurate time resolution (~ 400 ps for SciFis). Furthermore these detectors can stand high beam intensities in their active areas.

- **Small Area Trackers (SAT)**
  For the detection of particles with distances greater than 2.5 cm from the nominal beam axis, Micromega[27] and GEM[28] detectors are employed. Both types use microstructures for gas amplification and a strip readout. Moreover, PixelGEMs and PixelMicroemegas are used, GEM respectively Micromega detectors with a pixelised readout area in the center, which can be operated when exposed to the full beam.

[26]**R**ecoil **P**roton **D**etector
[27]**Microme**sh **ga**sseous structure
[28]**G**as **E**lectron **M**ultiplier

- **Large Area Trackers (LAT)**
  To cover the large angle acceptance of the spectrometer, detectors with a large active area are mandatory. In COMPASS different gaseous detectors are used. Drift chambers, using the drift time of the induced ionization for a precise position measurement, as well as MWPC[29]s and straw tubes are operated.

2.3.4. Calorimetry

Calorimeters are used for energy measurements and photon detection. Four calorimeters - two electromagnetic and two hadronic ones - are present at COMPASS.

The electromagnetic calorimeters ECAL1 and ECAL2 are made up of lead glass blocks which are arranged in a matrix around a hole for the beam. Impinging electrons and photons induce an electromagnetic shower inside the lead glass. These showers send out Cherenkov light which is collected by a PMT[30] at the end of each block. The collected light is proportional to the energy deposited by the impinging particle.

Hadronic calorimeters HCAL1 and HCAL2 are built up of alternating layers of hadron absorber material (iron, steel) and scintillation material. When a hadron passes the absorber material, an hadronic interaction is induced and an hadronic shower develops. The absorbed energy is transfered into photons in the scintillator material and the produced light is again detected by PMTs.

2.3.5. Particle identification

Muon identification is done by muon filters which consist of an absorber layer sandwiched between tracker stations. The absorber has to be thick enough to stop incoming hadrons. If both tracker stations, before and after the absorber, find a track, the particle is declared a muon.

Another important detector for particle identification is the RICH. Its vessel has a volume of $80\,\mathrm{m}^3$ and is filled with C_4F_{10} as radiator gas. The Cherenkov photons emitted by passing particles are reflected by two spherical mirror surfaces and detected by MWPCs with photocathodes on top and bottom. Thus, hadrons can be separated into pions, kaons and protons in an energy range between $5 - 50\,\mathrm{GeV/c}$.

For Primakoff studies, the RICH is not operated but pions, protons or kaons in the beam are tagged by CEDARs. In contrast to the RICH, CEDARs are only sensitive to a certain angle of Cherenkov light. Pressure changes of the radiator gas allow to adjust the sensitivity to a certain angle and thus to a certain type of particle.

[29]**M**ulti **W**ire **P**roportional **C**hamber
[30]**P**hoto**M**ultiplier **T**ube

2.3.6. Trigger

A trigger ensures recording of all relevant events while keeping the amount of accumulated data manageable. For the two different beam types, different trigger set-ups are used.

With muon beams, the trigger detectors are mostly hodoscopes located behind the muon filters because the triggers relies heavily on the outgoing muon's track. By combining geometrical arrangement and coincidence, triggering on muons only originating from inside the target volume is provided. This is performed for squared four-momentum transfers $Q^2 > 0.5\,\mathrm{GeV}^2/\mathrm{c}^2$. For lower transfers, hodoscopes, which trigger on the energy loss of the beam muon by considering the deflection angle in the magnetic field, are used.

For hadron beams, two scintillating counters, run in coincidence mode, trigger on incoming beam particles and a veto detector sorts out events where the target was not hit. The RPD, surrounding the target, triggers on events, where enough energy is transfered to the recoil proton to leave the target. This allows cleaner triggering on interactions inside the target volume. A multiplicity counter, downstream of the target, allows to trigger on events for diffractive studies.

Primakoff events are triggered by ECAL2, as a trigger is initiated when a certain amount of energy is deposited in the central part of the calorimeter [25].

2.3.7. Data acquisition

For data collection a DAQ[31] system is provided (see Fig. 2.6). The data produced by the detectors is digitalized via ADC[32] and/or TDC[33] modules and transfered to GeSiCA[34], HotGeSiCA[35] and CATCH[36] modules, where the data is concentrated. By way of optical fibres, the concentrators are connected to ROB[37]s, where the collected data is buffered before an EVB[38] sorts the data by its event number and groups together all pieces of data belonging to a single event. Events are stored in chunks of 1 GB size and then written on the CASTOR[39] tape storage, wherein a single event produces ~ 35 kB of data.

The DAQ is able to provide trigger rates up to 30 kHz, depending on the number of connected detectors and the event size. Per day more than 10 TB of data are written

[31]**D**ata **A**c**Q**usition
[32]**A**nalog to **D**igital **C**onverter
[33]**T**ime to **D**igital **C**onverter
[34]**GE**M and **Si**licon **C**ontrol and **A**cquisition module
[35]**HOT**Link **GE**M and **Si**licon **C**ontrol and **A**cquisition module
[36]COMPASS **A**ccumulate, **T**ransfer and **C**ontrol **H**ardware
[37]**R**ead**O**ut **B**uffer
[38]**EV**ent **B**uilder
[39]CERN **A**dvanced **STOR**age manager

onto the CASTOR tape storage, i.e. several 100 TB of data are recorded per year of data taking.

2.4. The COMPASS analysis

To handle the amount of data produced during by the spectrometer, a variety of software was developed by CERN and the COMPASS collaboration. They are introduced subsequent and a brief introduction is given how raw data becomes a physics event.

- **Cinderella**
  The online filter Cinderella [26] is basically a software trigger, as it achieves a cleaning of the trigger and an efficient way of data collection.As a side effect, the filter is very sensitive to detector performances and therefore, the filter rate, which is calculated after each SPS cycle, can be an indication for detector problems.

- **ROOT**
  ROOT [27] is an object orientated framework, that was developed at CERN as a successor to the Fortran based PAW[40]. It is writte in C++ and designed for the needs of high energy physics, hence being able to deal with a huge amount of data. Root provides many necessary tools for the analysis and the presentation of data, like histograms, fitting algorithms and compression methods to save disk space. It is therefore used used in most of the successive described programs.

- **COOOL**
  COOOL[41] is an online monitoring tool, which allows to access online data as well as offline data. It is based on ROOT and provides displaying histograms and basic fitting tolls. COOOL is heavily used to monitor data quality during beam time.

- **COMGEANT**
  COMGEANT[42] is based on the GEANT simulation program and is used to simulate the behaviour of particles in the COMPASS spectrometer. Variable interaction generators may be used, geometry files with the detector positions for the usage in CORAL can be generated and tracks as well as secondary tracks propagating through the spectrometer can be simulated.

- **CORAL**
  CORAL[43] is an event reconstruction software. The raw data are read and are converted through a multi-step process into hits in time and space. Thereafter,

[40]**P**hysics **A**nalysis **W**orkstation
[41]COMPASS **O**ject **O**riented **O**n**L**ine
[42]**COM**PASS **GE**ometry **AN**d **T**racking
[43]**CO**MPASS **R**econstruction and **A**na**L**ysis project

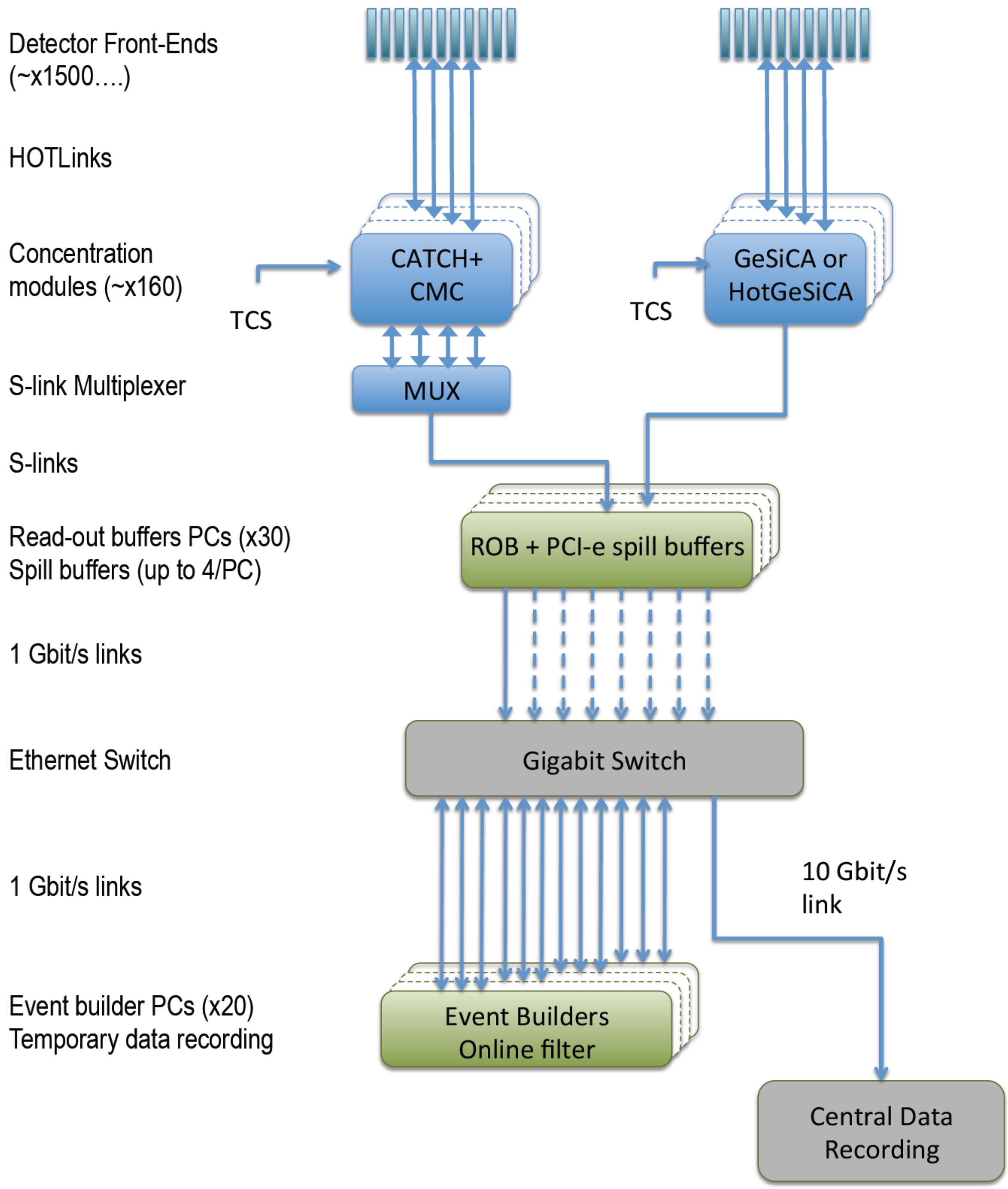

Figure 2.6.: Overview of the COMPASS DAQ system [23]

tracks and vertices are reconstructed. The output mDST[44] files can further be analyzed by PHAST.

- **PHAST**
  PHAST[45] is a toolkit for the analysis of data at mDST level. Users may define functions to apply cuts, event selections or the like on the processed data from CORAL to e.g. select data for special needs of the analysis or to reduce the amount of data. PHAST produces DST files which can be further processed within the ROOT framework.

[44] **m**ini **D**ata **S**ummary **T**able
[45] **PH**ysics **A**nalysis **S**oftware **T**ools

3. The COMPASS silicon microstrip detectors

3.1. Principles of a semiconductor particle detector

The main part of a semiconductor particle detector is a p-n junction, which is operated in reversed bias mode. A p-n junction forms at the contact surface of p-type and n-type materials in a semiconductor. In this area, the free charge carriers, electrons of the n-type material and holes of the p-type material, recombine and generate the so called depletion zone, where no free charge carriers exist and an electric field is present. Applying a bias voltage in reverse direction on the junction, allows to extend the depletion in size up to several millimeters. A particle, passing this arrangement, deposits energy and thus generates electron hole pairs. If this occurs in the depletion zone, the generated holes and electrons are separated by the electric field and transported to the corresponding ends of the depletion zone. The generated current signal enables the position determination of the penetrating particle.

A typical silicon microstrip detector[46] consists of a bulk of either n- or p-type silicon and strip shaped implants on either one or on both sides. The doping concentration of the implants is much higher than the concentration of the opposite type bulk material (e.g. p^+ implants for a n-type bulk) and hence form the junction. The diverging concentration also affects the dispersion of the depletion zone as it extends far into the bulk, while expansion into the implants is small. On top of the implant stripes a SiO_2 layer is applied onto which a metal strip is metalized. As the SiO_2 is electrically insulating, the metal strip is capacitively coupled to the silicon and an induced charge in the bulk layer, which is collected by the implant strip, therefore generates a signal in the metal strip. The pitch is typically around $50\,\mu$m.

3.2. The COMPASS silicon microstrip detectors

3.2.1. Requirements

In COMPASS, silicon microstrip detectors are used for beam definition and vertex detection. Radiation-hard detector design and excellent time resolution are mandatory due to

[46] For a detailed description consider e.g. [28]

the high beam rates in the order of 10^8 per spill. Furthermore, the material budget has to be minimized to accomplish high resolution measurements, as the spatial resolution is dominated by multiple scattering contributions. In the hadron program angles down to $100\,\mu$rad [29] need to be resolved, hence a good spatial resolution is needed. Another point is, that the active area of the wafer needs to fit the rather broad beam spot of the muon beam.

3.2.2. Operation at cryogenic temperatures

Radiation damage is a major item, when considering the operation of semiconductor detectors in high intensity particle beams. Apart from the energy loss process described in Sec. 3.1, NIEL[47] is important for the lifetime of semiconductor detectors [30]. NIEL is Rutherford scattering of impinging particles off a nucleus in the semiconductor material. This may cause the nucleus to leave its lattice position, hence leaving a vacancy. Both, nucleus and vacancy, can cause further defects, depending on the transferred energy to the nucleus.

Such defects may act as acceptors, thus the effective charge carrier concentration changes. Moreover, lattice defects may form trapping or recombination centers, which means loosing charge carriers, generated by passing particles, before they can be collected at the terminal. As a consequence the Charge Collection Efficiency (CCE) decreases (see equation 3.1).

$$CCE = \frac{collected\ charge}{generated\ charge} \tag{3.1}$$

Further problems may arise from the wafer's surrounding structures as e.g. biasing resistors may be damaged causing increased noise due to the build-up of immobile charge carriers in the oxide. Furthermore, radiation damages may reduce the silicon bulk's resistivity and thereby increase the leakage current.

Driven by the findings in [31], the original design goal of the detector system for COMPASS was to operate the wafers at a temperature of 130 K to face the aforementioned problems and thus improve the persistence of the silicons and to ensure a consistent performance for several years of operation. As shown in Fig. 3.1, the CCE of irradiated wafers increases at lower temperatures [31].

For this purpose, a cooling system using liquid nitrogen was developed (see also sec. 3.2.6). Additionally, a more stable read out was achieved as it is no longer affected by day-night or seasonal temperature fluctuations [32]. Moreover, the noise level decreased compared to non-cryogenic operation and time resolution as well as spatial resolution

[47] **N**on-**I**onizing **E**nergy **L**oss

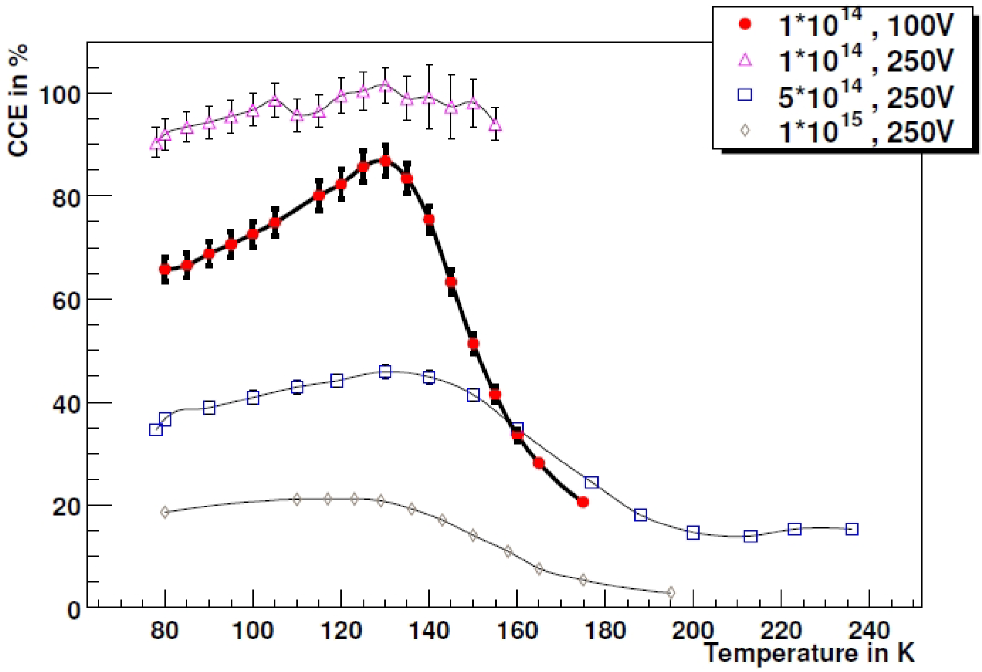

Figure 3.1.: Charge collection efficiency of three highly irradiated silicon detectors at cryogenic temperatures [31]

improved [33].

3.2.3. Wafer design

The silicon wafers[48] used at COMPASS were originally designed and developed for the HERA-B experiment [36]at DESY[49]. The wafer was developed by the HLL[50] of the Max-Planck-Institutes in Munich and produced by SINTEF[51].

The 280 μm thick n-type wafer has a $5 \times 7\,\mathrm{cm}^2$ sized active area and a resistivity of about $2 - 3\,\mathrm{k}\Omega\mathrm{cm}$. It is designed for a double-sided readout and thus reduces the material budget by a factor of two, compared to a single-sided readout. The 1280 strips on the n-side (pitch $54.6\,\mu$m) are perpendicular to the 1024 strips of the p-side (pitch $51.7\,\mu$m). The strips are tilted by $2.5\,^\circ$ with respect to the wafer edge (see Fig. 3.6).

Into the n-type bulk, n^+ and p^+ strip implants are realized on the n- and accordingly on the p-side. The p^+ strip implants and the n-type bulk form the p-n junction. The

[48]For a detailed description consider [34] and [35]
[49]**D**eutsches **E**lektronen-**SY**nchrotron, Hamburg, Germany
[50]**H**alb**L**eiter **L**abor
[51]**S**tiftelsen for **IN**dustriell og **TE**knisk **F**orskning, a Scandinavian research organisation

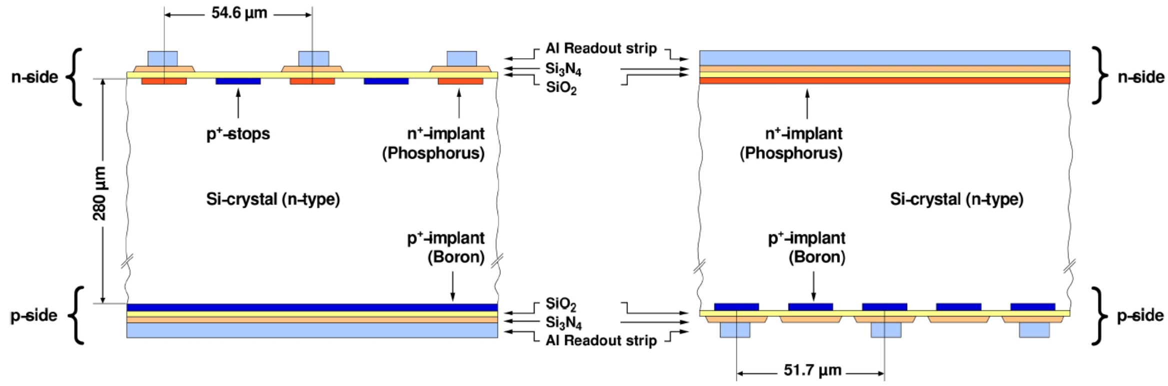

Figure 3.2.: Cross section through the COMPASS silicon detectors

strips, on both sides, are cladded with layers of Si_3N_4 and SiO_2 to separate them from the readout strips, made of aluminium. Such a capacitively coupled readout is required due to high leakage currents induced by radiation damages[52] [38]. On both sides, intermediate strips are provided for several reasons. On the n-side it is necessary to insulate the n^+ strip implants from each other to avoid short circuits through the bulk. Therefore p^+-stop implants are placed in between the n^+ strip implants. The presence of p^+ intermediate strips on the p-side improves the spatial resolution as they apportion their collected charge to the neighboring strips.

Polysilicon resistors with a resistance of $1\,\mathrm{M\Omega}$ are used to apply the bias voltage. Therefore, the active area is further enclosed with a multi-guard ring structure which enables controlled gradual drop of the potential from the detector rim to the undepleted substrate. In this configuration, the detector can be operated at voltages up to 500 V [38].

3.2.4. Detector module

The silicon wafer (described in sec. 3.2.3) is glued in between two L-shaped PCB[53]s (the so called L-Boards) with silicone glue. It is worth mentioning that only one of the two edges of the L-Boards is used for gluing, so that the wafer can move in order to avoid thermal stress.

The L-Boards are equipped with APV25-S1[54] readout chips [39], which are bonded to the PCB. These chips are connected to the wafer via a pitch adapter, which adjusts the wafer pitch (51.7 μm, 54.6 μm) to the APV analog input pitch (44 μm) and provides the

[52]The wafers are designed to withstand an annual flux of $3 \cdot 10^{14}$ minimum ionizing particles (MIPs) per cm^2 [37]

[53]**P**rinted **C**ircuit **B**oard

[54]**A**nalogue **P**ipeline **V**oltage mode ASIC

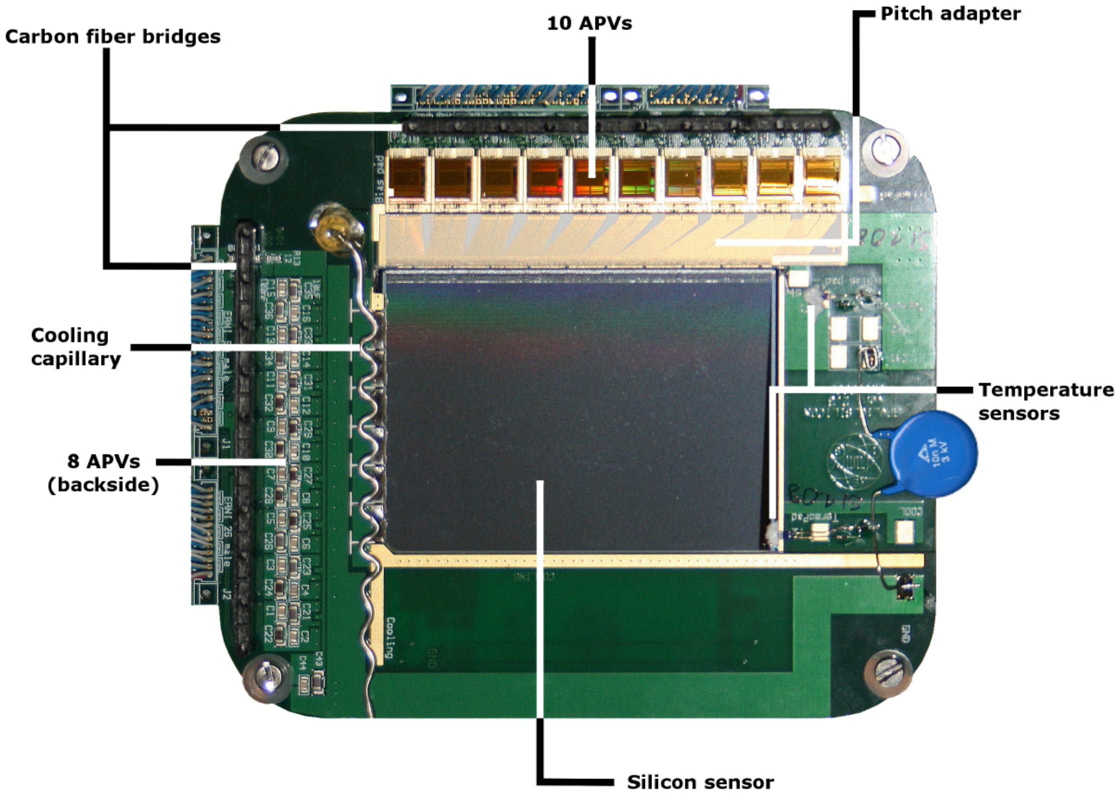

Figure 3.3.: The COMPASS silicon detector module [40]

fan-out, necessary because of the inter-chip distance. One APV chip provides 128 analog input channels, thus 10 chips are needed to read out the n-side and 8 chips for the p-side.

The assembled module[55] is cooled by two, nitrogen flushed, capillaries[56], which are bent in a wave shape and soldered to the PCB. The capillaries are connected via epoxy connectors to which they are glued. Three Pt100[57] temperature sensitive resistors are used for monitoring the temperature. Two are glued onto the L-Board, while the third is directly glued onto the wafer, where it is not occupied by readout strips.

Cables are used to connect the Boards to the outside. They are soldered directly to the L-Boards. In previous versions, connectors were used to connect the cables, but this solution did not prove save for cryogenic operation, as the connectors deform under the temperature change. Soldering the cables instead of using connectors worsened the rigidity of the L-Boards, therefore bridges made up of CRP[58] were attached to the L-Boards to stabilize them.

[55] each APV chip dissipates 0.3 W on average, thus the whole module $\sim 5.4\,\mathrm{W}$ [41]
[56] 1.3 mm inner diameter, 1.6 mm outer diameter, Material: Alloy 400 [42]
[57] a temperature sensitive platin resistor with a resistance of $100\,\Omega$ at $0\,^{\circ}\mathrm{C}$
[58] **C**arbon-fiber**R**einforced **P**olymer

3.2.5. Cryostats

In order to enable an operation of the detector modules at cryogenic temperatures, they are mounted inside cryostats. Two different embodiments of cryostats are in use, the upstream cryostats, which are placed upstream of the target, and the conical cryostat, which is positioned downstream of the target inside the RPD.

The upstream cryostat

The upstream cryostat (see Fig. 3.4 and Fig. 3.5) provides an ashlar-formed clearance with a volume of 240 mm $\times$ 240 mm $\times$ 82 mm (H x W x D). Three connectors of different size are provided at the cryostat's bottom, which are used for the installation of a venting valve, a vacuum pump and a vacuum gauge. The cryostat also features two ports, for the installation of feedthroughs, on its top, its left and on its right side.

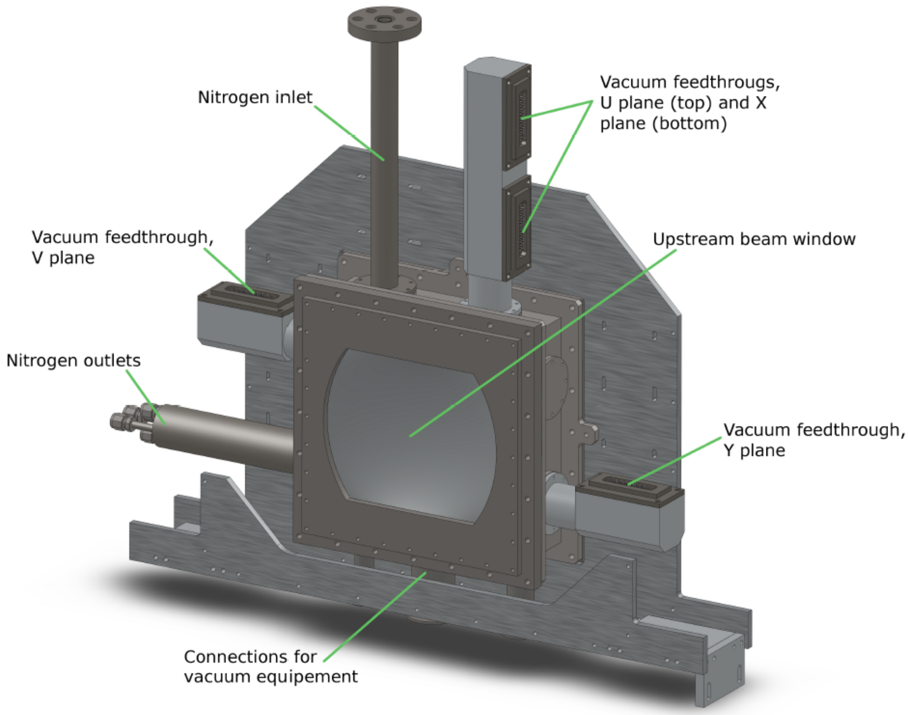

Figure 3.4.: Perspective CAD model of an upstream cryostat [32]

Three of the ports are usually equipped with attachments offering a D-sub DD-50M connector. These attachments are typically connected to one port on the left side of the cryostat and one port on the right side respectively. The right port on top of the cryostat is assembled with an extension and offers two D-sub connectors. These four connectors are used for the read out of the two detector modules and the phase separator, which are mounted inside the cryostat.

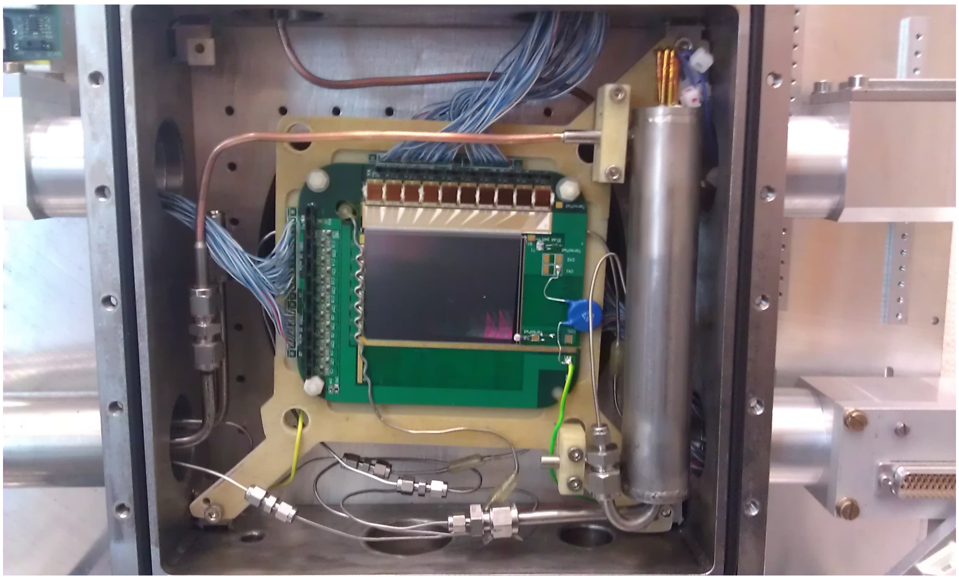

Figure 3.5.: Completely assembled, open upstream cryostat (with Pt100 phase separator)

The nitrogen inlet is installed at the left port on top of the cryostat. It is designed as 300 mm long pipe, that is connected to the inside of the cryostat and therefore under vacuum. Inside the pipe, a nozzle is foreseen to receive the end of the transfer line. Hence, vacuum insulation between the end of the transfer line and the cryostat walls is ensured. The outlets for the nitrogen are usually installed at the lower left port, inside a 190 mm long pipe to ensure reliable operation of the O-ring seal between port and the outlet pipe[59].

The front side and the backside of the cryostat housing are closed with bulkheads, which are mounted to flanges. During operation in the beam, bulkheads with so called beam windows are in use. Therefore, the bulkhead provides a cavity in the center region, where a carbon fiber mesh, which is covered with an aluminized Mylar[60] foil, is applied. Thus, a minimal material budget in the center area (active area) is achieved. In lab conditions, where the material budget is irrelevant, steel plates are employed as bulkheads.

The mounting of the detector modules is done via a GRP[61] support structure, named

[59]The temperature drop at the seal is thereby lowered and consequently the function of the O-ring is not harmed; the O-ring should be operated at room temperature).
[60]biaxially-orientated polyethylene terephthalate
[61]**G**lass-**R**einforced **P**lastic

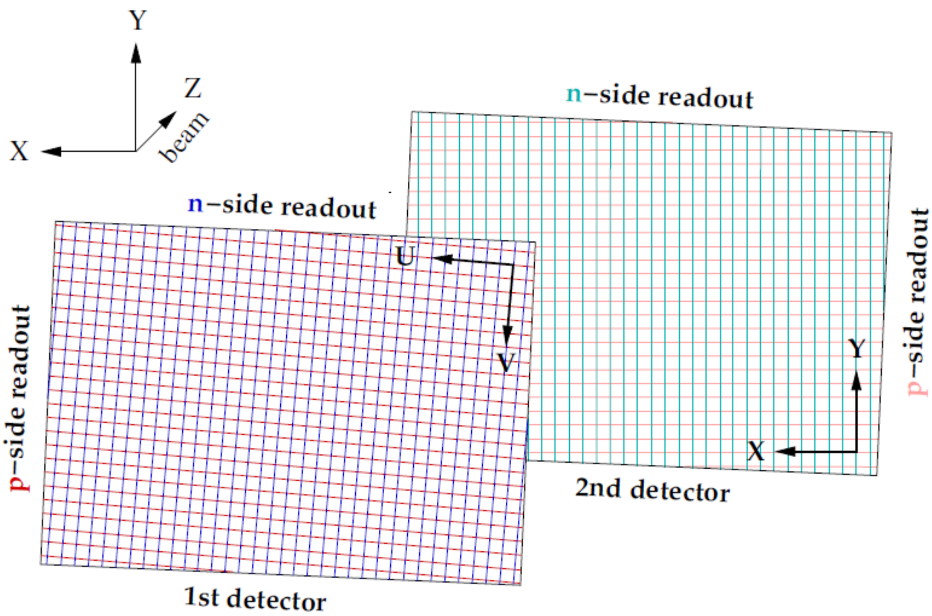

Figure 3.6.: Scheme of the silicon detectors' geometry (when mounted in a cryostat) [15]

shuriken. For each cryostat, one shuriken is mounted holding two detector modules (see Fig. 3.5). The modules are mounted back to back, such that the module sides with 10 APV-chips are facing the bulkheads. Both modules are tilted by 2.5 °, so that the strips of the downstream module are parallel and accordingly perpendicular to the plumb line while the strips of the upstream module are tilted by 5 °. This configuration provides the four readout planes U, V, X, Y (see Fig. 3.6).

The conical cryostat

Before the introduction of the RPD, vertex detection with silicon detectors was done with two silicon stations placed on an optical bench downstream of the target[62]. With the RPD installed at the COMPASS spectrometer a new design for a cryostat housing the silicon detectors became necessary in order to be able to integrate them into the RPD. Therefore, the conical cryostat (see Fig. 3.7) was developed, which fits, due to its conical shape, into the RPD's inner scintillator ring. For installation, the conical cryostat is fixed to movable rails and the RPD is moved out of the beam line. The rails with the assembled cryostat are then inserted and affixed.

The inner volume of the conical cryostat is in the acceptance of the spectrometer. Therefore, the design goal was to minimize the material budget, resulting in especially designed CRP support frames, which hold the four detector modules. Furthermore the phase separator was transfered from the cryostat itself to the outside, into the so called

[62]only for hadron runs

phase separator box, which is attached to a separate set of rails. The phase separator box is equipped with a nitrogen inlet and a phase separator equal to those of the upstream cryostats, but the separator provides liquid nitrogen to two instead of one detector module.

The conical cryostat is completed by removable CRP beam windows at its back- and front side respectively. The cryostat further features eight ports, where one is used for the interjunction with the phase separator box, while two ports are used as nitrogen outlets and four of the remaining five contacts are employed for the connection of vacuum pumps.

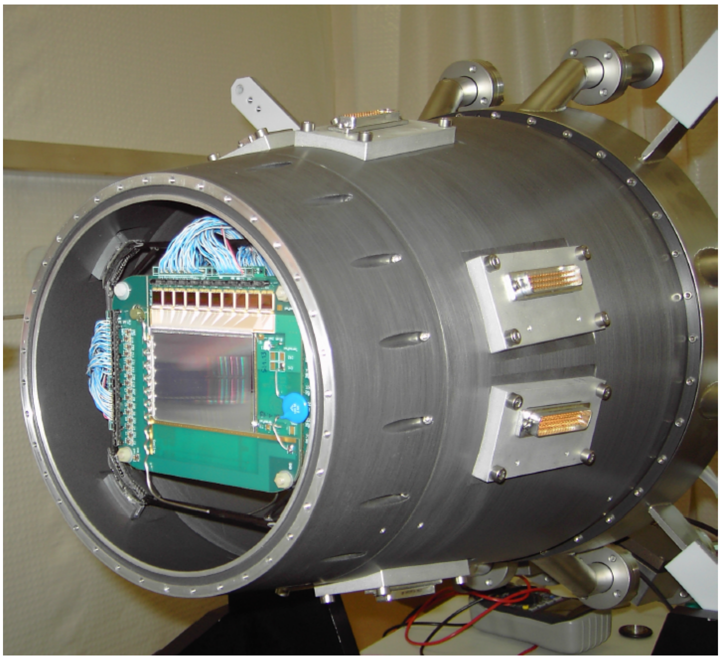

Figure 3.7.: Conical cryostat (open) with an assembled detector module

3.2.6. Cooling system

As mentioned in Sec. 3.2.2 it is desired to operate the silicon detectors at 130 K. Therefore, a nitrogen distribution system with an according electronic control system and data acquisition was developed.

The experimental hall of COMPASS is connected to a central liquid nitrogen supply. From the central COMPASS dewar the valve box is fed by a 100 m long vacuum insulated flexible transfer line. This box serves as a buffer volume as well as a distribution system, that ensures a steady flow of liquid nitrogen with appropriate pressure to the silicon stations. Its core is a 50 l liquid nitrogen reservoir, whose fill level is regulated between

35 - 70 % and kept at 1.8 bar absolute pressure. A circular tube is affiliated to the bottom of the basin, wherein four cryogenic valves are connected to the tube to regulate the nitrogen flow to the stations. The whole assembly is enclosed by a passive thermal screen made of copper and cooled by the gaseous nitrogen exhaust.

The valves are followed by four connections, which are able to incorporate flexible transfer lines to route the liquid nitrogen to the stations. Moreover, the valve box provides a variety of pressure, temperature and level sensors to ensure a stable and reliable operation.

The transfers lines from the valve box are connected to the nitrogen inlets of the individual stations and the liquid nitrogen is further guided to the phase separator via a copper tube. The phase separator is necessary, because during the travel along the transfer line part of the liquid nitrogen evaporates due to heat input into the transfer line. Thus a mixture of liquid and gaseous nitrogen arrives at the separator. To avoid negative influence on the cooling stability, the phase separator is used to ensure that only liquid nitrogen is provided to capillaries soldered to the detector modules, while the gaseous nitrogen is released to the outside. At the moment, two phase separator designs are present at COMPASS, old ones which are controlled by a valve and one of a newer design, regulating the fill level via Pt100 temperature sensitive resistors [32].

As already mentioned in sec. 3.2.4 the detectors modules dissipate 5.4 W on average, but for safety reasons a cooling capacity of 8 W was chosen. To adjust this capacity, the flow through the capillaries has to regulated via integrated flowmeters. They are controlled via an analog voltage to set the desired flow and further provide an analogue voltage corresponding to the actual flow. These flowmeters are placed at the liquid nitrogen outlets of the individual detectors, respectively, at the phase separator's gas exhaust and provide a maximal flow of 5l/min and 20 l/min, accordingly.

The whole cooling system[63] is controlled by a Siemens SIMATIC S7-300 industrial automation system with a modular design[64]. Thus, a stable operation of the detectors at desired temperatures within ±2 K is provided [23]. Undesirable and possibly dangerous situations to personnel and equipment are detected automatically and emergency procedures are set in motion. Furthermore, automatically generated e-mail and SMS notifications are sent to the responsible persons.

3.2.7. Set-up at COMPASS

The positioning of the silicon stations was already mentioned in sections 2.3.3 and 3.2.5. In this section, the positioning of the stations within the spectrometer shall be explained

[63] temperature sensors, vacuum gauges, flowmeters, etc.

[64] A more detailed description and further information on the working principle can be found in e.g. [32]

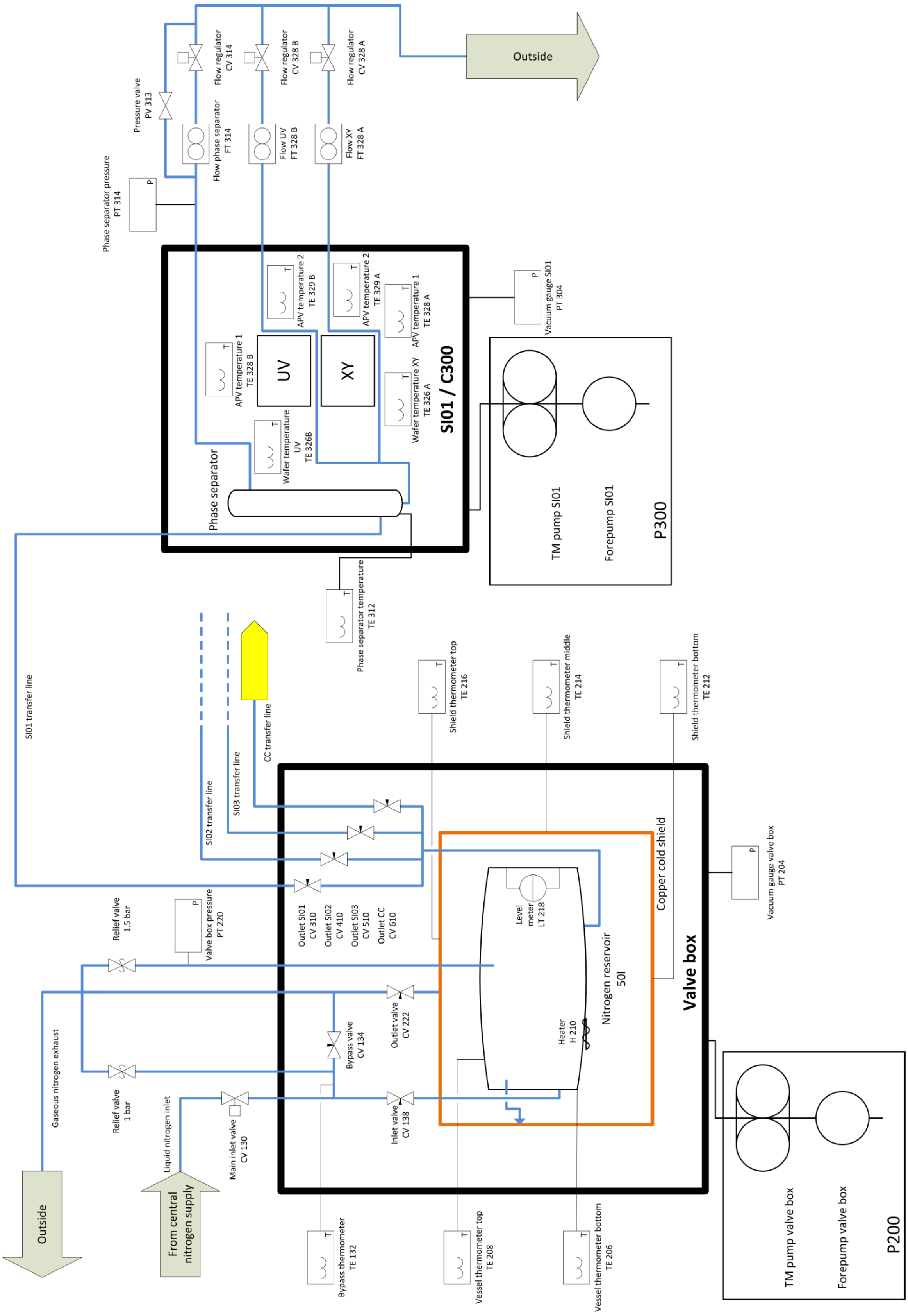

Figure 3.8.: Process flow diagram of the cooling system (for the upstream cryostats)

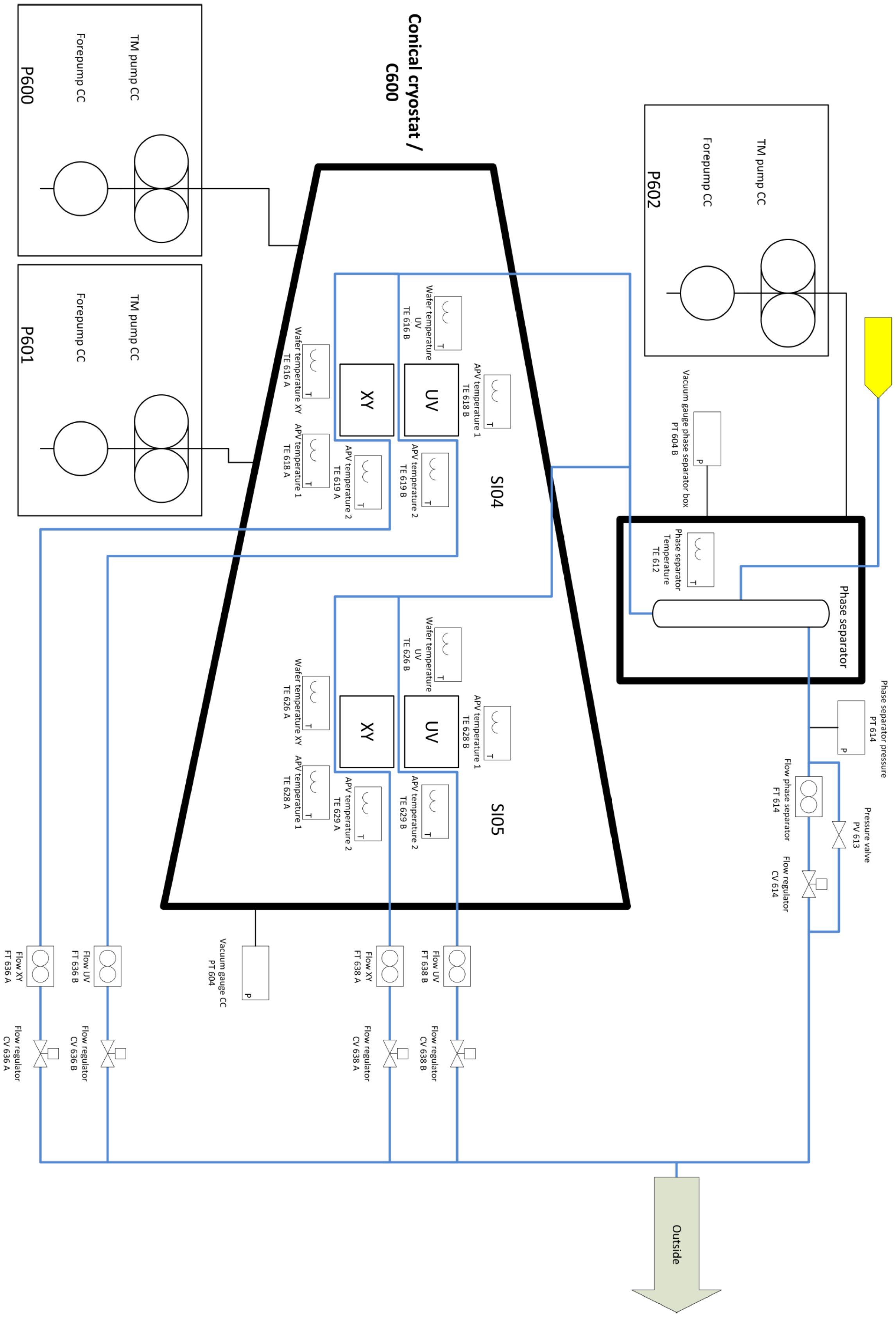

Figure 3.9.: Process flow diagram of the cooling system (for the conical cryostat); the yellow arrow connects to its counterpart in Fig. 3.8

more detailedly.

For hadron runs, three upstream stations are used for beam definition and the conical cryostat, effectively a double station, is used for vertex detection, whereas for muon runs only the three upstream stations are employed as beam telescope.

For the description of the conical cryostat's positioning reference is drawn to sec. 3.2.5 and sec. 5.1.2. However, the discussion shall focus on the upstream stations. They are placed upstream of the target with the consequence that they have to be removed every year to allows access to the target[65]. Therefore, the installation and the displacement of the stations has to be done with a reasonable amount of time and work.

Due to this requirement, concrete blocks are placed on the experimental hall's floor to an elevated platform. This height serves as basis for another, smaller layer of concrete blocks and as working platform. On top of this second layer of concrete blocks, an optical bench is placed, which is kept in position by metal clamps and provides two granite rails where the cryostats are mounted to. The optical bench allows to adjust the cryostats' position in all six degrees of freedom, in order to align and center the detectors' active areas to the beam axis. The valve box and the electrical cabinet of the Siemens system reside on a second platform next to the one of the silicons. From there, the transfer lines are guided to the individual stations via a metal railing, which is fixed to the second elevation of concrete blocks. In case, the conical cryostat is installed, a second railing is used to guide a longer transfer line to the RPD. The nitrogen outlets of the stations are connected to a gas exhaust rail, which leads out of the hall and releases the nitrogen into the environment. Furthermore, the gaseous nitrogen from the valve box's gas exhaust is conducted into the environment via a transfer line.

Furthermore, the beam windows of the cryostats are equipped with a thin film of polyethylene, whereupon the interspace between beam window and polyethylene film is flushed with gaseous nitrogen at room temperature. Thereby, icing of the beam windows is prevented.

3.2.8. Readout chain

The readout chain (see Fig. 3.10) begins with the APV25 chips on the detector itself which are connected to the repeater card. These cards supply on the one hand the APV chips with a low voltage of $\pm 3.3\,\mathrm{V}$ and on the other hand, the analogue output signals of the APV25 chips are repeated by a unity gain amplifier and sent further to the ADC. Furthermore, the repeater cards feed the detector modules with high voltage (see section 5.1.1 for further details).

[65] The target can only be equipped or unloaded with target material if the upstream stations are removed.

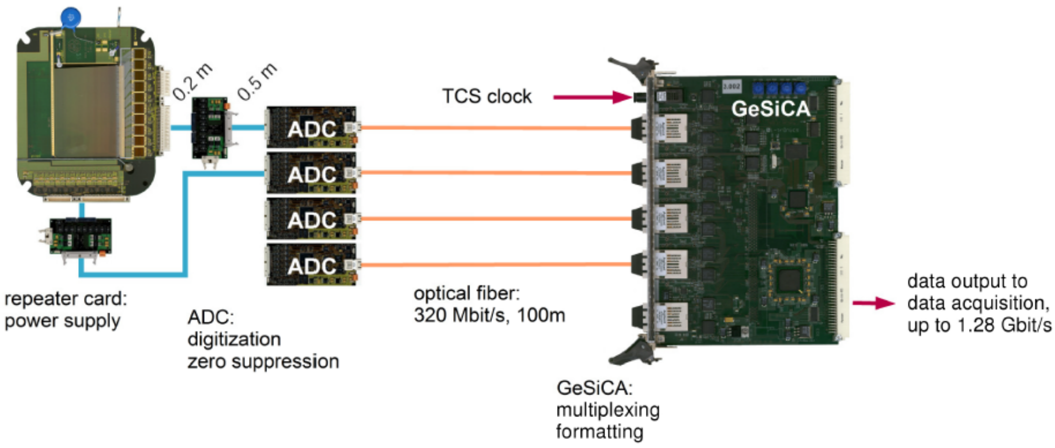

Figure 3.10.: Readout chain of the COMPASS silicon detector [15]

By the ADC, the analogue signals are digitized by 10 bit ADCs with a sampling rate of 40 MHz and further processed to FPGA[66]. There, the data is reduced via pedestal substraction and zero suppression [43]. In principal, a (previously recorded) pedestal value is subtracted from the value for each channel and the remaining value is compared to a (previously recorded) noise level of the channel. If the signal is significantly higher[67] than the noise level, it is considered to be a hit and further processed to FIFO[68] buffers. Moreover, another correction concerning the collective changes of the pedestals, the common noise, is applied to correct fluctuations of all 128 channels of an APV due to small fluctuations of the APV's supply voltage [44].

The data buffered in the FIFOs are then sent to the GeSiCA[69] via optical link. Here, the incoming data stream is multiplexed and the TCS[70] event header, which identifies the event the data is belonging to, is added. The data are then reformatted for the transmission via an optical fiber and thus sent to the ROBs.

The GeSiCA modules distributes trigger signals, TCS clock and and reset signals to the ADCs and from there to the APVs, thus the opposite way through the readout chain. Also programming ADCs and FPGAs as well as setting APVs and ADCs is possible via this transmission line.

[66]**F**ield **P**rogrammable **G**ate **A**rray
[67]usually by a factor of 4
[68]**F**irst **I**n **F**irst **O**ut
[69]One GeSiCA is able to deal with the input of four ADCs, i.e. of one silicon station.
[70]**T**rigger **C**ontrol **S**ystem

3.2.9. Performance

The important parameters to characterize a particle detector are spatial resolution, time resolution and efficiency[71]. A residual distribution (see Fig. 3.11) allows to determine the spatial resolution by its RMS. The average intrinsic spatial resolution of the COMPASS silicon detectors is 5.3 μm for the p-side and 6.9 μm for the n-side.

The time resolution(see Fig.3.12) is better than 2.5 ns for each single plane with an average resolution of $\langle\sigma_t\rangle = 2.1$ ns. An average efficiency above 99 % is achieved, where hits within a spatial window of $\pm 3\,\sigma$ around the extrapolated track position are accepted (see Fig.3.13).

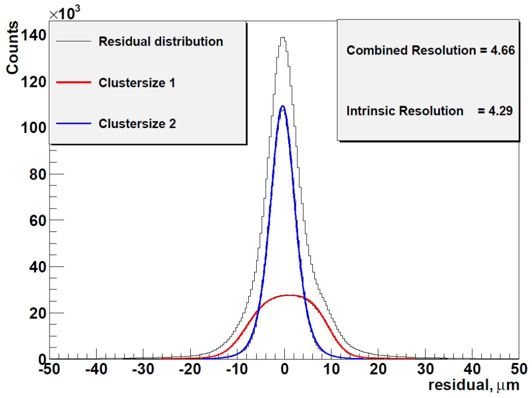

Figure 3.11.: Typical residual distribution for a silicon plane [23]

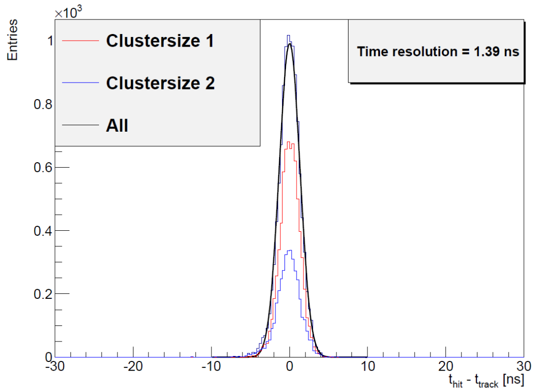

Figure 3.12.: Typical time distribution for a silicon plane [23]

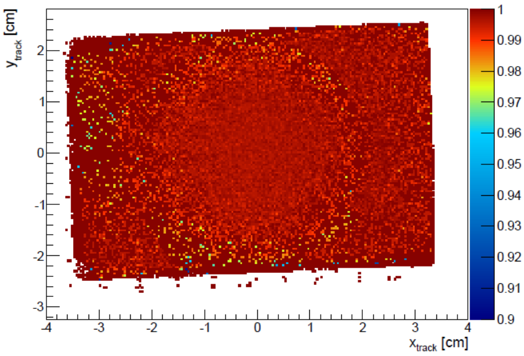

Figure 3.13.: Typical efficieny for a silicon plane [23]

[71] All values are taken from [23]

4. The modular phase separator

The phase separator, being an essential component of the liquid nitrogen cooling system of the silicon microstrip detectors, has been subject to many research activities of the COMPASS silicon group. Various designs have been tested whereas only a small number of designs are employed in the actual experimental setup. The latest attempt before the start of this thesis is described in [32], where also a brief history of the phase separators of the COMPASS silicon detectors is given.

This chapter discusses the motivation for further improving the design of the phase separator. Furthermore, a newly developed design is presented, and the evaluation progress as well as the obtained results of the tests are described.

4.1. Motivation

4.1.1. Relevance of the phase separator for the silicon detectors

In the description of the cryogenic cooling system (see Fig. 4.1 or Figs. 3.8 and 3.7) in Section 3.2.6, it was mentioned that during the transfer of the liquid nitrogen from the valve box to the individual stations part of the liquid vaporizes due to heat input into the transfer line. For cooling one station, the flow through the transfer line has to be significantly lower than the maximum possible flow. Hence, the liquid nitrogen has to flow comparatively slow through the line. Despite a vacuum in the order of $10^{-5} - 10^{-6}$ mbar in the isolating part of the transfer line to minimize heat conduction, there remains a small heat input into the liquid guiding part of the transfer line causing the liquid nitrogen to evaporate. Consequently, the longer the liquid nitrogen takes to pass the transfer line, the more heat is assimilated by a given volume and thus, a larger fraction of the liquid vaporizes on its way to the cryostat. With the aforementioned small flow of nitrogen for the individual silicon stations, a large amount of gaseous nitrogen is produced inside the transfer lines in order to keep them cryogenic and guided to the stations.

This liquid/gas mixture arriving at the nitrogen inlet of the cryostat is not suitable for stable cooling of a detector. For this reason, a device was introduced in order to separate the gaseous from the liquid part of the nitrogen and therefore enable stable cooling of the detector modules with liquid nitrogen. At COMPASS, two designs of a phase separator are present, older bobbin-valve phase separators (which will not be discussed here, a description can be found in [32]) and a newer Pt100 phase separator, introduced by [32].

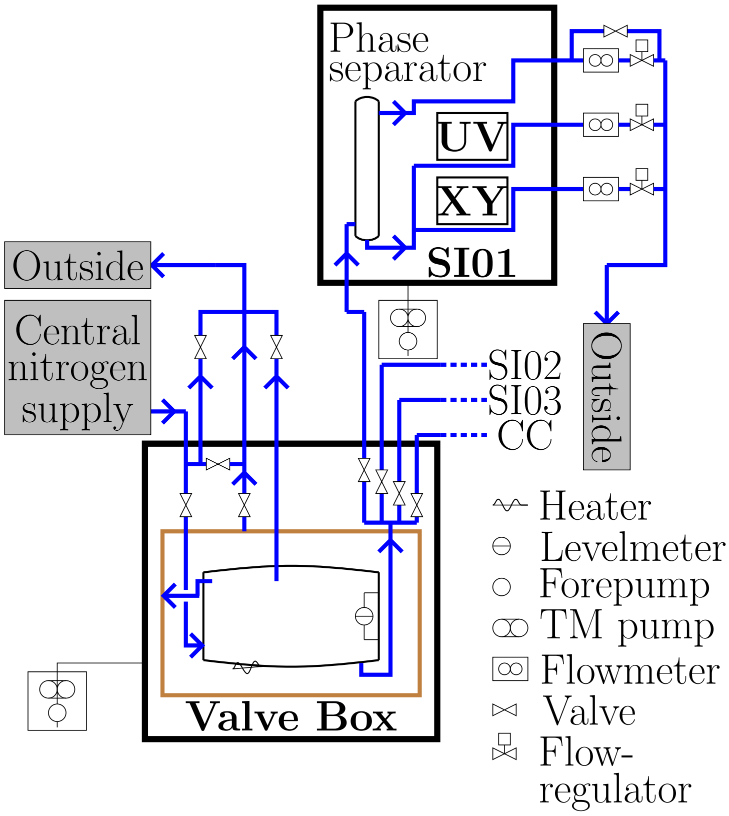

Figure 4.1.: Simplified flow diagram of the nitrogen cooling system

While the Pt100 regulated phase separator features advantages over the bobbin-valve phase separators, there are still several shortcomings in the design which show room for improvement and which will be discussed in the next section.

4.1.2. Shortcomings of the previous development

The phase separator introduced by [32] (see Fig. 4.2), includes a tube made of stainless steel having two connections at the bottom for the connection of the cooling capillaries of the two silicon modules per cryostat. Furthermore, the phase separator holds a nitrogen inlet and a gaseous nitrogen outlet at the upper part of the cylindrical body. Inside the tube, a glass fibre rod is placed, which carries four Pt100 resistors that are used to regulate the fill level in the cylinder. The electrical connections are guided to the outside via a feedthrough (see Fig. 4.2(b)) which is welded into a ring (shown blue in Fig. 4.2(a)) at the upper end of the tube.

For operating the Pt100 phase separator, a PLC[72] system is needed to read out the

[72]**P**rogrammable **L**ogic **C**ontroller

Pt100 resistors and to regulate the nitrogen flow via a flowmeter depending on the temperature measured at different filling levels of the phase separator.

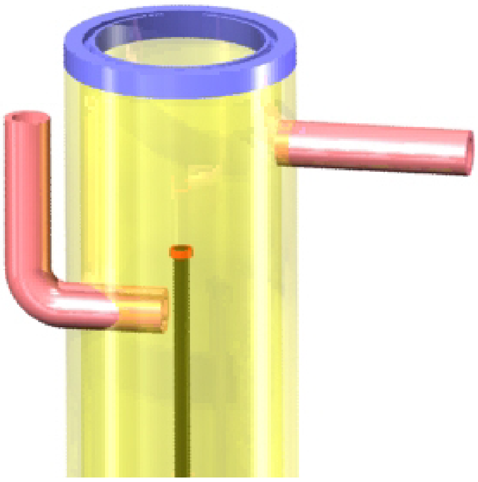

(a) Perspective CAD detail view of the Pt100 phase separator

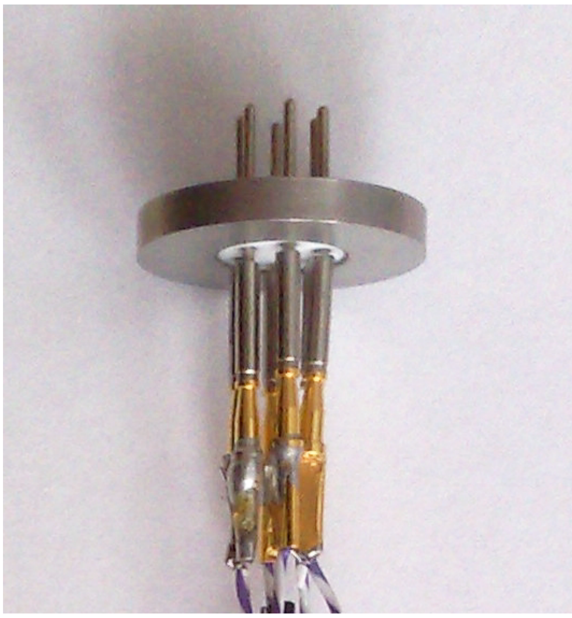

(b) Close view of the vacuum feedthrough

Figure 4.2.: Pt100 phase separator as treated in [32]

Though being a nice and simple apparatus to separate the different phases of nitrogen, it became apparent that welding the feedthrough to the separator's body is not ideal. As a first point, the welding is a delicate action since the welding connection between feedthrough and ring is very fragile due to the size of the welding joint and the maximum heat input permitted into the feedthrough which is partially made of ceramic, and prone to cracking. Further, the ring, that the feedthrough is welded into, has to be perfectly matched to the feedthrough itself to provide for a stress-free welding. For the construction of the separator used in SI02, the ring contorted due to the heat when it was welded to the steel tube, and it was not re-worked after welded to the steel tube. This caused mechanical stress on the feedthrough and thus on its ceramic part. As the ceramic is extremely rigid, and thus does not elastically deform, the stress caused by the deficient ring led to a leak which allows nitrogen to leave the separator, degrading the vacuum in the cryostat. For the foregoing reasons, it is desired to have a phase separator which uses a less delicate feedthrough, and which is easier to construct.

Another disadvantage of welding the feedthrough to the separator's body is that the fixation is irreversible. When constructing the prototype separator used in [32], one of the Pt100 temperature sensors used for the fill level regulation was lost during the welding process. Due to the permanent fixation of the feedthrough to the body, it was not possible to replace the Pt100 temperature sensor without cutting the cylinder and consequently permanently destroying the phase separator. Having only destructive access to the interior for replacement or repair is a huge drawback since a sloppy soldering joint or the failure of one or more Pt100 sensors might render the whole device unusable. This is, on the one hand, an issue concerning labour costs since welding specialists and other technicians are involved. On the other hand, also material costs play an important role: the feedthrough only, being a highly developed part, costs more than € 100. Moreover, the costs of the other components are not negligible, either. Hence, it is desired to have a phase separator allowing access to its interior for maintenance purposes and enabling replacement of components.

4.2. Design

Having in mind the drawbacks of the latest phase separator development, it was proposed to replace the ceramic feedthrough with a non-permanent feedthrough. Though encountering several challenges when using epoxy resin as a closure for previous generations of phase separators, it was decided to go forward with another attempt using this versatile material since it has proven its basic applicability by its use in capillary connectors within the silicon project and its usage in cryogenic applications even with liquid helium.

The final design is shown in Fig. 4.3(a). The phase separator consists of a stainless steel tube (shown semi-transparent) having an outer diameter of 30 mm, a wall thickness of 2 mm and a height of 157 mm. The bottom side of the tube is closed by cylindrical disk having two recess clearances for the liquid nitrogen outlets where the capillaries are connected[73]. The disk is further equipped with a holding fixture for the glas fibre rod, replacing the elaborate spacer constructions used in [32] or for the separator of SI02. On the upper left side of the tube, the nitrogen inlet guiding the liquid/gaseous nitrogen mixture into the separator is shown. The inlet is done in a way that the nitrogen is guided tangential to the inner wall of the tube in order to reduce spraying of the liquid. The gas exhaust is shown on the upper right side of the tube. Further, on the lower right side of the separator, a stainless steel rod which allows the fixation of the phase separator to the shuriken inside the cryostat is attached.

The newly designed feedthrough (for details see Figs. 4.4(a) and 4.4(b)) consists of two parts. On the one hand, the upper closure of the stainless tube which is in principle a cylindrical disc with a recess clearance having a tubular extension with a wall thickness of 250 μm. The upper end of the tubular extension is provided with a radially extending lip, wherein the lip and and part of the tubular extension are segmented. The second part of the feedthrough is an end cap made of epoxy [45] which is molded around the tubular extension through which a glas fibre rod together with the electrical connections

[73]all non-permanent pipe connections are done via Swagelok® connectors

(a) Perspective CAD view of the modular phase separator (b) Close view of the rod carrying the Pt100 temperature sensors

Figure 4.3.: Modular phase separator

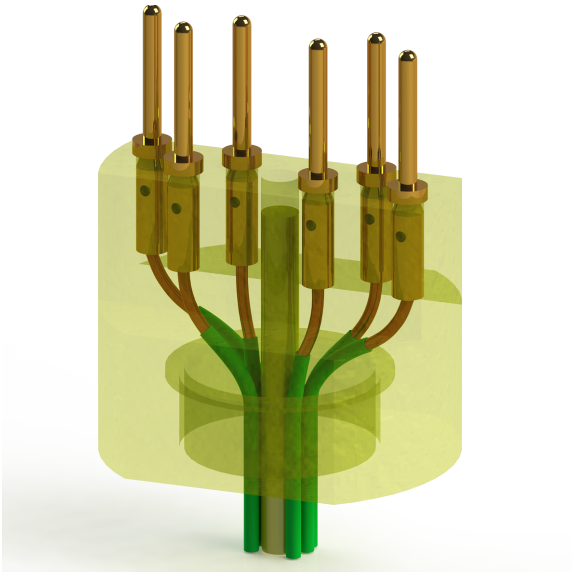

(a) Perspective CAD view of the epoxy end cap (semi-transparent)

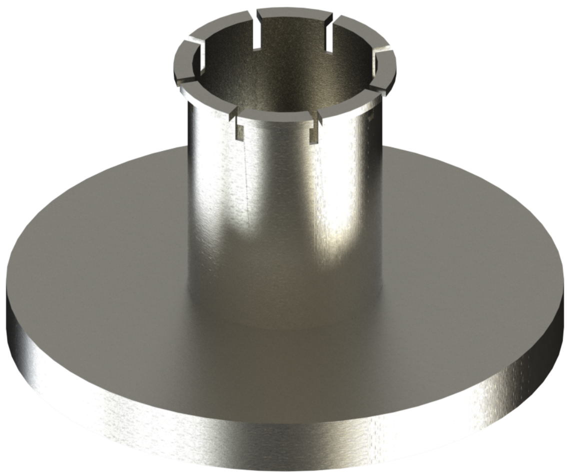

(b) Perspective CAD view of the feedthrough, the end cap is glued to

Figure 4.4.: Feedthrough

of the Pt100 temperature sensors extend laterally. The epoxy end cap acts as a vacuum feedthrough for the electrical connections and for stability reasons, its lower part contains a portion of carbon fibre[74].

Owing to the characteristics of the epoxy [45], it is possible to detach the epoxy end cap, if desired, by the following method. Exposing the epoxy to temperatures around 200 °C for several hours makes the epoxy lose adhesiveness and allows to remove it from the tubular extension, hence allowing access to the interior of the phase separator. In case of problems with the temperature sensors or the epoxy end cap itself, the end cap can be removed and one is able to fix the problem.

For the fill level regulation, four Pt100 temperature sensitive resistors are used, which are glued to the glass fibre rod. For compatibility with the separator used in SI02, the same electrical configuration of the Pt100 temperature sensors as in [32] was chosen, which means that two sensors share their electrical ground. Since the precision achieved in this way is sufficient, the two-wire readout of the sensors is used instead of a more precise four wire readout.

[74] $7-10$ cm of a single carbon fibre cut into small pieces for 2.2 g epoxy.

4.3. Evaluation and results

The first step of evaluation of the new phase separator concept was the investigation of the epoxy end cap's geometry. After a rather massive block geometry was discarded, the end cap was chosen with the geometry as shown in Fig. 4.4(a). Furthermore, the mixing ratio of the individual components of the epoxy adhesive was investigated and fixed to a ratio of 1.2 weight parts of hardening agent to 1.0 weight part of binding agent in order to achieve a resilient end cap. First cooling test were done with a separator dummy made of stainless steel, simulating the top part of the phase separator. The separator dummy was exposed to liquid nitrogen in order to simulate a filled phase separator and afterwards, an optical inspection of the end cap as well as a test of vacuum tightness of the assembly were done[75]. After testing a couple of end caps, it became evident that end caps made of pure epoxy are not suitable as a feedthrough for a phase separator since these end caps always cracked. Therefore, a portion of carbon fibre was added the lower part of the end cap in order to increase the stability[76]. Cooling test of several of these more advanced end caps, with varying portions of carbon fibre, did not show cracks on the particular end caps or any vacuum degradation, compared to vacua measured before cooling the particular assemblies, for a certain amount of carbon fibre. Hence, a complete phase separator was assembled holding an end cap with a fraction of carbon fibre found suitable in the course of the foregoing tests.

For the evaluation of this fully assembled phase separator, the cryogenic test bench introduced by [32] was used (see Fig. 4.5). As the general functionality of Pt100 regulated phase separators was already proven in [32], the main focus was the leak tightness of the newly designed feedthrough. Therefore, only a minimized setup inside the cryostat was chosen, namely the phase separator and a capillary connected to the separator without any dedicated thermal load[77] (see Fig. 4.6).

Cooling down the phase separator revealed a cryo leak in the setup. Fig. 4.7(a) shows how the vacuum inside the cryostat (CVx14) degrades when the phase separator reaches a temperature (TE_x14) of approx. 180 K. After in-deep investigation, the newly designed feedthrough was identified to hold the cryo leak.

An optical inspection of the epoxy end cap did not show any cracks or visible damage. Therefore, the end cap was detached from the feedthrough allowing an insight into it. It was recognized that most probably the Teflon coatings of the wires, which connect the Pt100s with the pins, triggered the cryo leak. The Teflon coatings were extending up to the lower end of the pins, thus allowing the liquid nitrogen to rise to the pins, probably escaping via small air pockets or hairline trenches along the pins, when the adhesion of

[75]The test were done when the assembly was back at room temperature.

[76]One cannot add carbon fibre to the upper part of the end cap since the carbon fibre might short circuit the electrical connections.

[77]Electrical resistors may be used to introduce an adjustable thermal load simulating the presence of a detector module, however this is not needed for the first step of commissioning the phase separator.

Figure 4.5.: Setup of the test bench

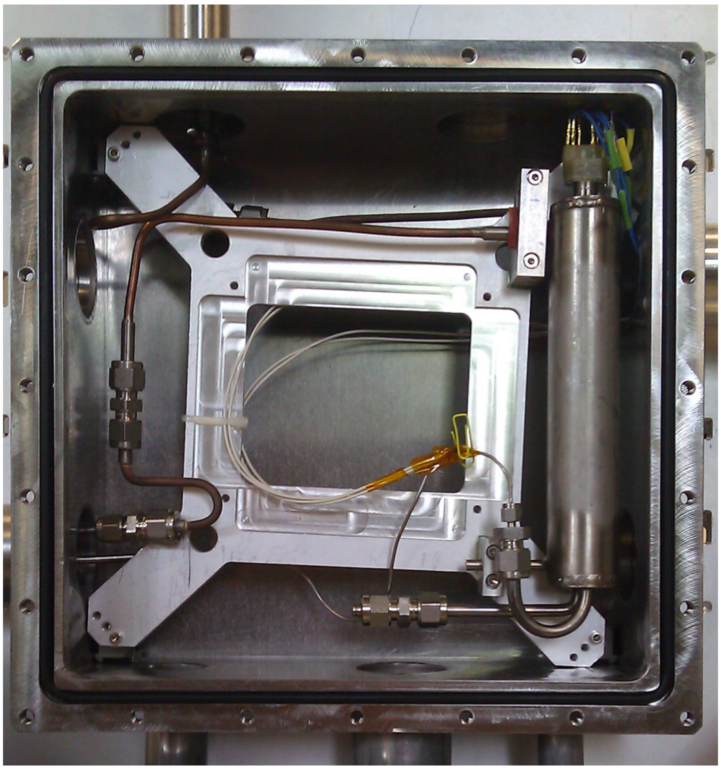

Figure 4.6.: Inside the cryostat

the epoxy resin to the pins is not perfect. Furthermore, there is practically no adhesion to be expected between the Teflon and the epoxy. As shown in Fig. 4.4(a), the coating of the wires has to end several millimeters before the wires are soldered to the pins in order to achieve a sufficient pressure separation between cryostat and phase separator.

Based on the gathered experience, a second phase separator was assembled. Thereby, the glas fibre rod and the Pt100 resistors, attached thereto, could be reused, proving the nondestructive accessibility to the phase separator's interior. The Teflon coating of the wires was removed for the last part of each wire (approx. 7 mm), which translates into approx. 5 mm of naked wire when the wire is soldered to the pin. Having bare wires, special care has to be taken that the wires do not touch and therefore render the attached Pt100 resistors inoperative. Moreover, it is important that the bare wires were molded with pure epoxy resin to avoid short circuiting wires via a carbon fibre portion.

The cooling diagram for the second phase separator is shown in Fig. 4.7(b). The vacuum pressure inside the cryostat improves to approx. $2 \cdot 10^{-5}$ mbar during the cool down of the phase separator and slightly increases to approx. $7 \cdot 10^{-5}$ mbar afterwards depending on the pressure inside the cooling circuit. One may state the phase separator is in principal leak tight as the vacuum remains stable at approx. $7 \cdot 10^{-5}$ mbar. However, it seems that the vacuum inside the cryostat is slightly related to the pressure inside

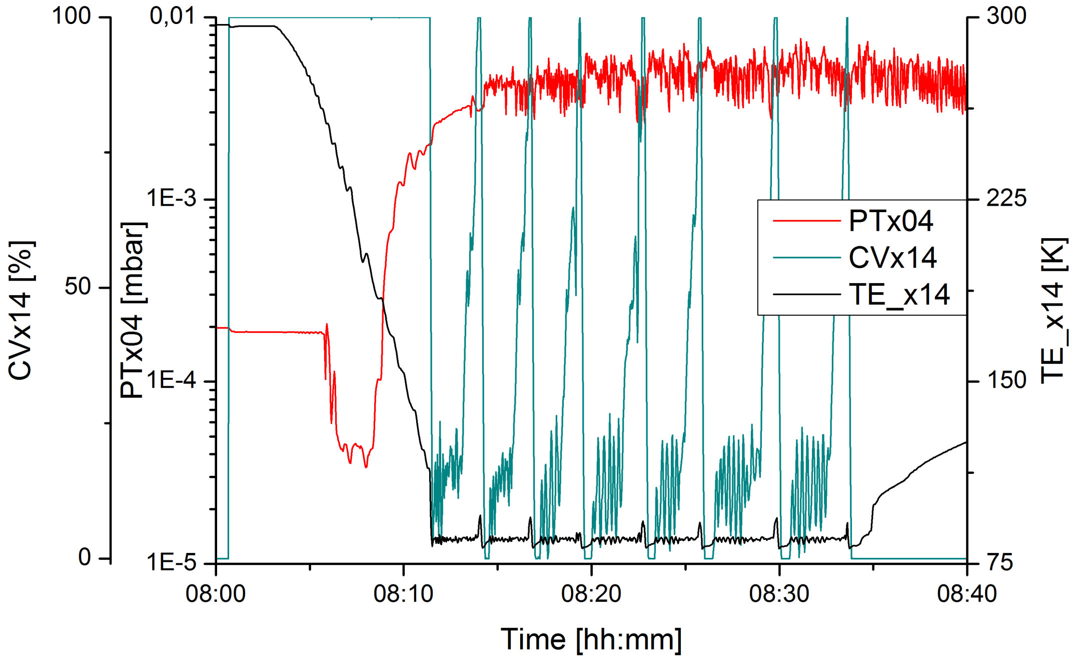

(a) Cooling diagram for the phase separator holding the cryo leak

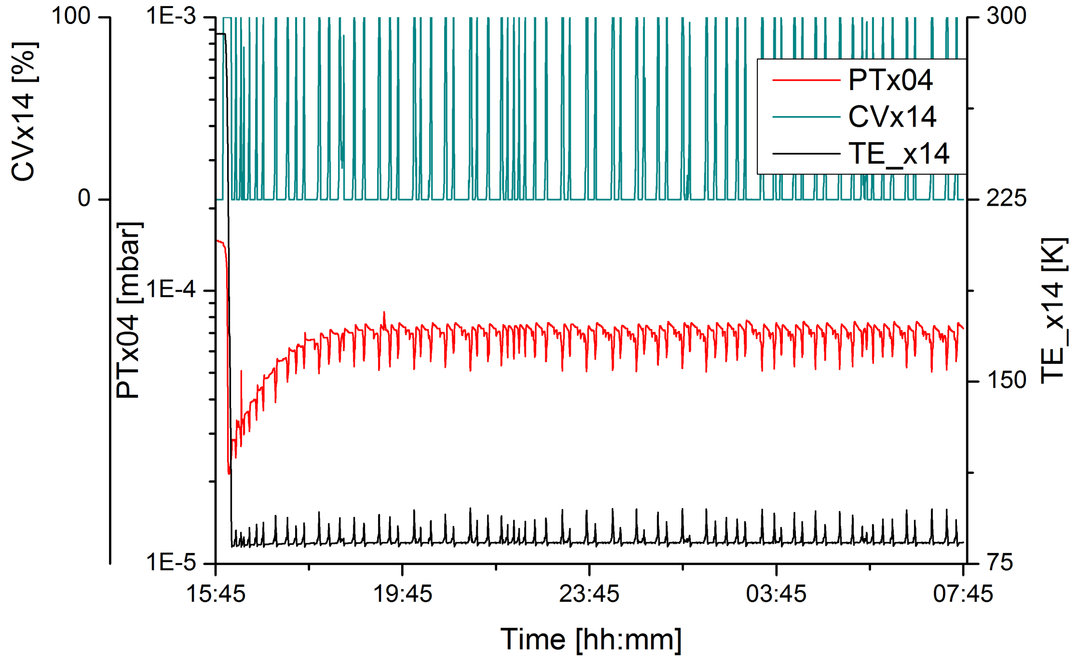

(b) Cooling diagram for the second phase separator

Figure 4.7.: Cooling diagrams

the phase separator as the vacuum improves once the flowmeter (CVx14) opens, which corresponds to a pressure drop in the phase separator, and decreases when the flowmeter closes, which means that the pressure inside the phase separator increases. The vacuum pressure dependence on the pressure in the cooling circuit indicates a remaining cryo leak in the cooling circuit. However, the cryo leak is comparatively small and does not impede the cryogenic operation of a silicon detector with this new type of phase separator.

4.4. Conclusions

The newly developed design for a phase separator with a non-permanent feedthrough has proven applicability. Further improvement of the phase separator's leak tightness may be achieved by applying slight constructional changes to the feedthrough. For example, the surface of the feedthrough may be roughened to improve the adhesion between epoxy end cap and feedthrough. In addition to that, the lateral extension of the segmentation cuts that are provided at the end of the feedthrough may be shortened and a second lip placed several millimeters apart from lip extending radially at the end of the feedthrough may improve the leak tightness, as they increase the distance between surfaces exposed to the pressure inside the phase separator and surfaces exposed to the vacuum in the cryostat. In order to simplify the production process of the phase separator, the molding assembly should be redone in a way, that the glas fibre rod is fixed to the molding assembly, omitting a spacer inside the phase separator and allowing easier access to the pins during the preparatory work for the molding process.

As the COMPASS silicon microstrip detectors will not be operated in 2013 and 2014, one may enhance the design of the phase separator as described above and make it a valuable alternative to the other designs employed at COMPASS.

5. A water cooling system for the repeater cards of the COMPASS silicon microstrip detectors

For most part of the 2012 beam time, measurement of Primakoff reactions was done. In order to measure these reactions, it is of paramount importance to have detectors with a very good spatial resolution, placed directly after the target. Hence, COMPASS uses silicon microstrip detectors which offer a very good spatial resolution, as already described in Section 3.2.9. Four such detector modules are housed in the conical cryostat. The repeater cards, described in Section 5.1.1, are plugged into connectors on the cryostat. Since the repeater cards produce quite some waste heat, adequate cooling is necessary to ensure stable operation. With the air cooling system used in 2009 showing poor performance, it was decided to assemble and install a water cooling system for the repeater cards, which is described in detail in this chapter.

5.1. Requirements

The first part of this chapter focuses on the requirements for a water cooling system for the repeater cards. The design of the repeater cards and the consequences and needs for a cooling system are described. Furthermore, the situation inside the RPD is given, explaining why passive cooling is problematic and introducing the general framework for the cooling system.

5.1.1. The repeater cards of the COMPASS silicon microstrip detectors

As already mentioned in Section 3.2.8, a repeater card (see Fig. 5.1) is the second link in the readout chain of the silicon detectors. Each repeater card is plugged into a vacuum feedthrough on the cryostats, connecting it to one detector plane. A ribbon cable connects the repeater card with the ADC.

The repeater card receives analogue output signals from eight or ten (for V/Y- and U/X-planes, respectively) APV25 chips. The signals from each APV25 chip are amplified by a unity gain amplifier and sent further to the ADC. The transmission of signals

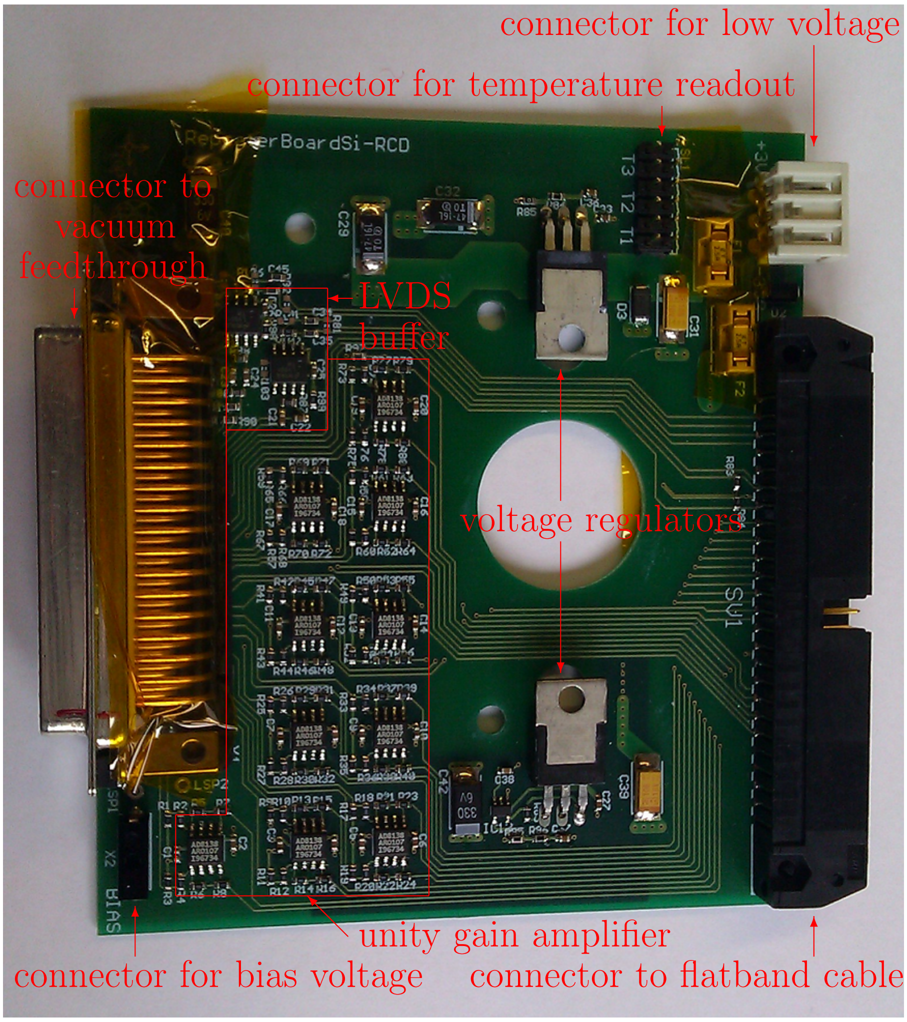

Figure 5.1.: Top view of a repeater card with components labeled

is also possible in the other direction via two LVDS[78] buffers, allowing to program and reset the APV25 chips and distributing trigger signals or TCS clock.

Apart from its function as a signal retransmitter, the repeater card distributes the bias voltage to the detector module. V- and Y-planes are put to ground, whereas U- and X-planes are put to their respective high voltages.

The APV25 chips reading out the detector receive their supply voltage via the repeater cards, too. The repeater card is connected to a CAEN A1518A power supply module. The APV25 chips of a plane need a positive and a negative voltage of 3.3 V and a current of 0.5 A to 0.7 A in reset condition. After the settings are loaded, the chips of a single plane consum in total currents of 1.4 A to 1.7 A for U- and X- planes (ten chips)

[78]**L**ow **V**oltage **D**ifferential **S**ignaling

and 1.1 A to 1.4 A for V- and Y-planes (eight chips) [46].

Voltage regulators are used to make sure that the APV25 chips are provided with exactly 3.3 V as cable lengths and instabilities in the power supply modules render a direct connection unstable.

These voltage regulators are the main source of heat on the repeater cards. If the regulators are not cooled, they may reach temperatures of more than 60 °C. With heat dispersing through the whole repeater card, the temperatures of the amplifiers and the buffers rise as well. With temperatures around 50 °C to 60 °C, the amplifiers gradually loose the characteristic of linear amplification causing differing signal amplitudes compared to regular operation conditions. Moreover, it is not possible to operate the amplifiers stably during a complete beam time, especially during summer months when high environment temperatures intensify heat problems [29].

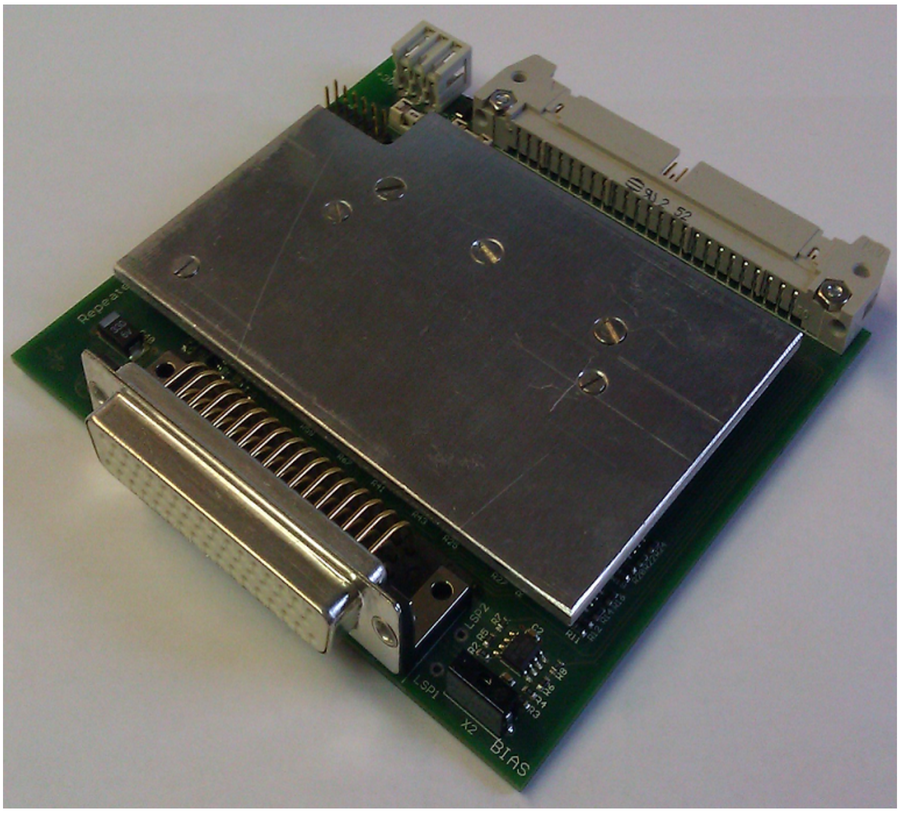

Figure 5.2.: Perspective view of a repeater card equipped with aluminium cooling plates

To alleviate these heat problems, the repeater cards were equipped with passive cooling plates made of aluminium (see Fig. 5.2). With this passive cooling solution, the voltage regulators are in thermal contact with a first aluminium plate mounted on the front side of the repeater card to increase the contact surface with surrounding air which in turn increases the heat dissipation to the environment. Additionally, the aluminium plate is thermally connected via a cylindrical heat conductor, made of aluminium, with a second aluminium plate. With this configuration it is possible to keep the temperatures on the repeater cards in range between approximately 35 °C and 45 °C, provided that the repeater cards are exposed to enough circulating air as it is the case for the upstream stations.

In the next chapter it is explained, why this cooling concept does not work properly in the RPD and why another solution is mandatory.

5.1.2. The situation inside the RPD

In Section 2.3.2 it is already described, that the RPD (see Fig. 5.3) is a barrel with 1620 mm in diameter, housing two rings of scintillators, the target(s) mounted along its longitudinal axis and the conical cryostat immediately downstram of the targets. As one can nicely see in Fig. 5.3, the conical cryostat is surrounded by the inner scintillator ring and extends through the downstream marguerite.

The marguerite is an aluminium disc, placed in the RPD, perpendicular to its longitudinal axis, with a variety of cutouts. The conical cryostat is mounted on four rails which are fixed to the marguerite. It is, in it's final position inside the RPD, also directly screwed to the marguerite. Like this, the position of the conical cryostat is determined by the position of the marguerite. Moreover, the rails for the phase separator box, the ADCs of the silicon detectors and the bases for the PMTs[79] of the inner scintillator ring are all mounted on the marguerite.

In Fig. 5.4 one can see that the repeater cards (water cooled version) are placed in between the light guides of the inner scintillator rings. In priniciple, the distance in between the light guides is not a problem for placing repeater cards. However, the PMTs connected to the light guides limit the thickness of a fully equipped repeater card to approximately 25 mm, since the repeater cards have to traverse the gaps between the PMTs when moving the conical cryostat from its mounting to its final position.

Regarding Figs. 5.3 and 5.4, one may guess already that cooling the repeater cards with surrounding air might not be a promising approach. The direct vicinity of the repater card is populated rather densely and air circulation inside the RPD is in practicably absent. Furthermore, one has to consider the heat dissipation of the scintillator's PMTs. As a consequence, the air temperature inside the RPD is on average higher than the air temperature of the experimental hall. Therefore, a satisfying passive cooling is not achieved.

[79]**P**hoto**M**ultiplier **T**ube

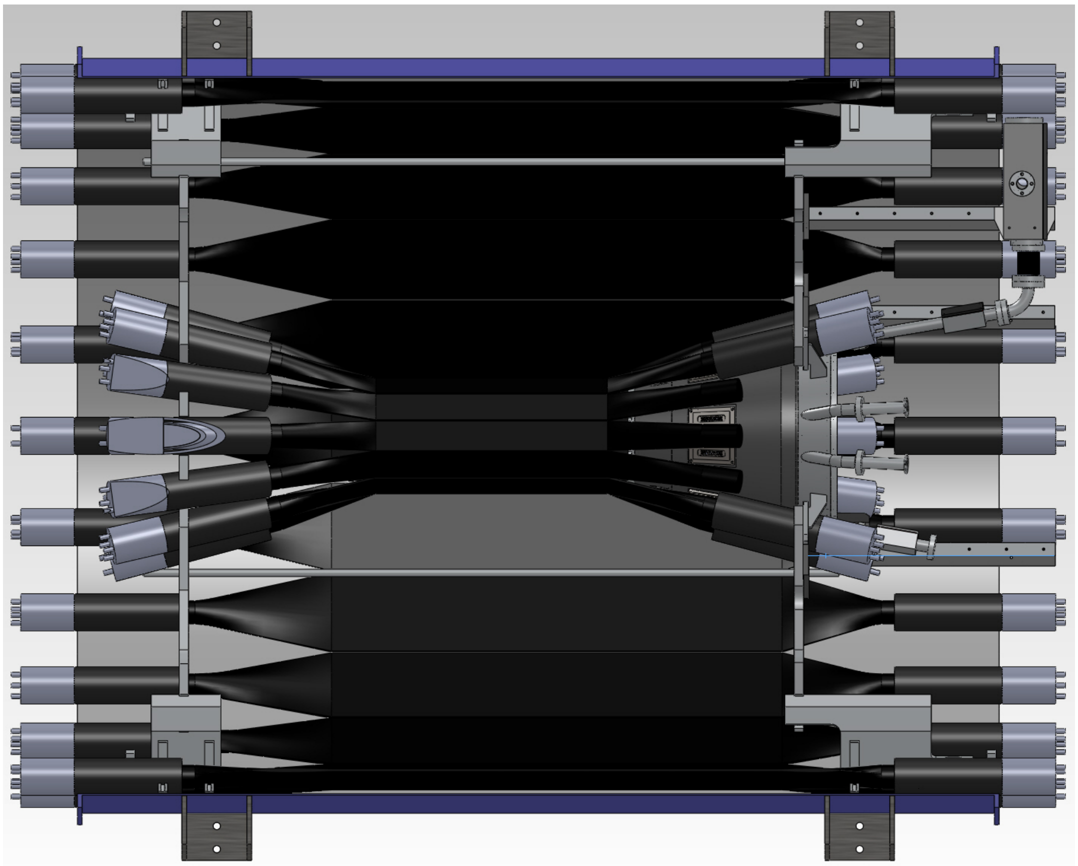

Figure 5.3.: Cross-sectional view of the RPD; some photomultipliers (of the inner scintillator ring) on the right side hidden

The first approach to the problem, used in 2009, was the use of air blowers (see Fig. 5.5) to create an artificial air flow to the repeater cards. A blower was placed on the platform under the barrel and the air flow was guided to the repeater cards via plastic tubes which were attached to various parts of the assembly. But this cooling solution holds a variety of disadvantages. A first point is that due to the design of the RPD it is rather complicated to guide the artificial flow directly to the repeater cards, since no real mounting structure for such a system is foreseen. Another point is, that the air cooling system did not offer any possibility to monitor the status of the cooling equipment or the repeater cards' temperature.

One of the most striking points is, that cooling with air is inefficient compared to water due to the four thousand times lower specific heat capacity of air ($c_{air} \approx 1.2\,{}^{J}/_{1K}$) compared to water ($c_{water} \approx 4173\,{}^{J}/_{1K}$)[80]. Another very important point is the fact that during the summer months, when the environment temperatures are highest, the heat transport off the repeater cards through air lowers due to the smaller temperature difference. During spring and fall, the temperature of the surrounding air is lower and thus

[80]values taken from [47]

heat transport is better. The system offers the lowest cooling power when in fact the highest cooling power is required and provides the highest cooling power when a lower cooling power compared to summer time is needed.

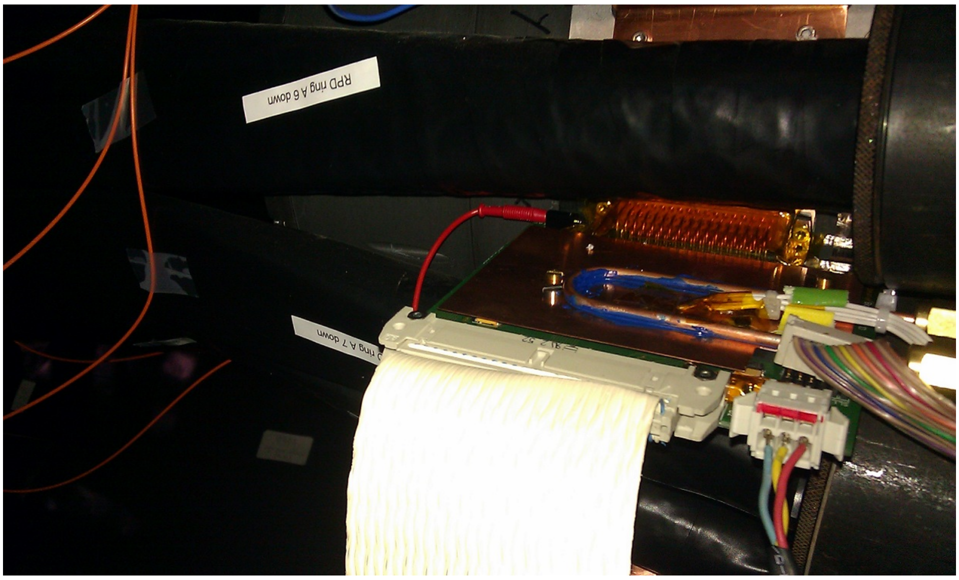

Figure 5.4.: Fully equipped repeater card (water cooled version) mounted between the light guids of the inner scintillator ring

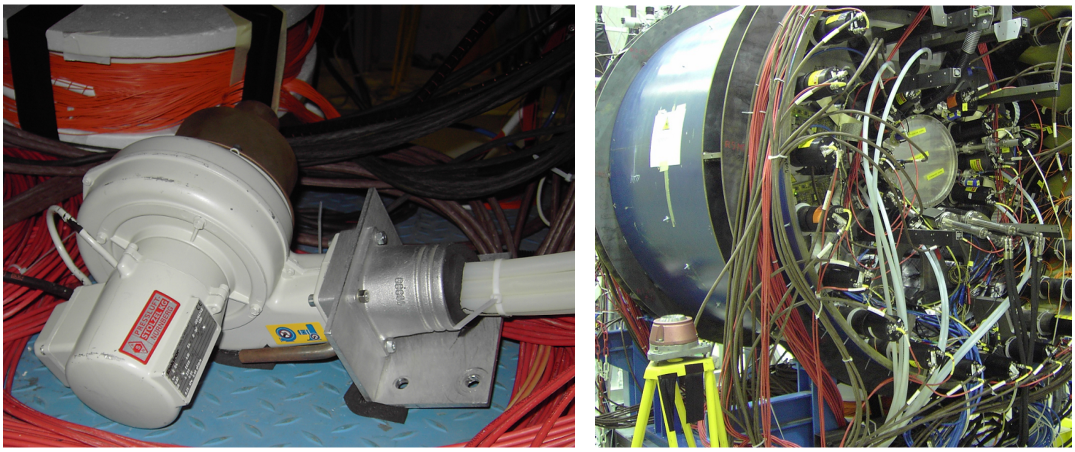

(a) Blower placed under the barrel

(b) Tubes (white) guiding the air flow to the repeater cards

Figure 5.5.: Air cooling system used in 2009

In order to overcome the aforementioned problems and moreover, to operate the repeater cards on a constant temperature throughout the whole year, it was decided to change to a water cooling system, which is described in detail below.

5.2. Design

5.2.1. General principle

When starting with the design for a water cooling system for the repeater cards, it became clear immediately that a standard overpressure water cooling system as used in practically all commercially available cooling solutions (e.g. for desktop computers) is unsuitable. In case of a leak in the system, the repeater cards distributing HV to the silicon stations and the surrounding photomultipliers being on HV might be exposed to escaping water, causing a serious danger not only to the equipment but also to detector experts working on it. Hence, a solution had to be found which prevents any kind of spilling water while fulfilling all the requirements listed above. With other detector systems at COMPASS having similar cooling requirements for their front-end electronics, attention was turned to the water cooling system for the front-end electronics of the COMPASS RICH [48]. Based on the experiences with this system, a cooling solution was developed for the silicon detectors.

The system is designed as a PLC controlled underpressure circulation system, as shown in Fig. 5.6. The two basic elements of the system are water reservoirs placed on the platform underneath the RPD barrel (`Reservoir A`) and on top of the barrel (`Reservoir B`). The reservoirs are connected via tubes, and `Reservoir B` is connected to a continuously running vacuum pump with magnet valve `EV670` (which is controlled by the PLC) and a ball valve in between. While `Reservoir A` is filled with water and exposed to atmospheric pressure, the vacuum pump and the valves are used to create an underpressure in `Reservoir B` which causes the water to rise from `Reservoir A` to `Reservoir B`. The fill level of `Reservoir B` is monitored via two water sensors `LS670A` and `LS670B`, which are read out by the PLC. In order to avoid an overshot of water from `Reservoir B` through the tube into the vacuum pump, the ball valve is used to adjust the flow of air from `Reservoir B` to the vacuum pump when(ever) magnet valve `EV670` is open.

One can see in Fig. 5.6 that the circulation path is split right after `Reservoir B`, which is due to the arrangement of the repeater cards around the conical cryostat. In order to minimize impedance problems, both paths have the same length and are each equipped with an individual circulation pump. Moreover, the heat input for both paths is considered to be approximately the same since each path holds two repeater cards supplying ten APV25 and two cards supplying eight APV25 chips. Having in mind these assumptions, both paths are considered to behave similarly.

Considering Bernoulli's principle, it is possible to determine the necessary underpressure for filling `Reservoir B` with water from `Reservoir A`:

$$p + \rho g h + \frac{1}{2}\rho v^2 = const. \tag{5.1}$$

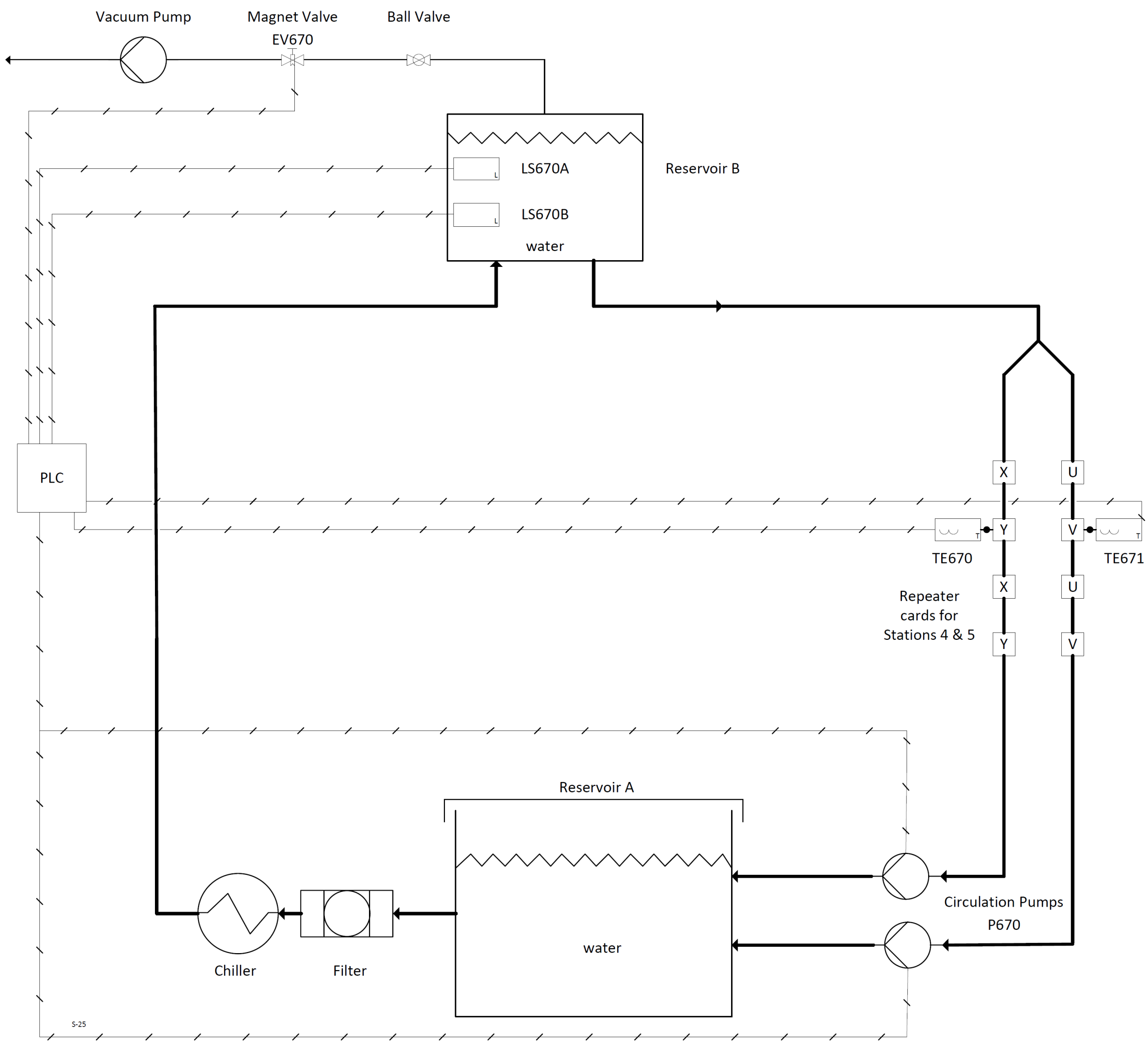

Figure 5.6.: Scheme of the water cooling system for the repeater cards of the COMPASS silicon microstrip detectors

In order to raise water from `Reservoir A` to `Reservoir B`, it is necessary to overcome the pressure difference caused by the difference in height h of the two reservoirs. For an altitude difference $h \approx 2\,\mathrm{m}$ between the two reservoirs, a density of water of $\rho_{water} = 0.998\,{}^{g}/_{\mathrm{cm}^{-3}}$ at $20\,°\mathrm{C}$ and the standard gravitational acceleration being $g = 9.81\,{}^{m}/_{\mathrm{s}^2}$, the necessary underpressure can be calculated:

$$\Delta p = -\rho_{water} g h \approx -200\,\mathrm{mbar} \tag{5.2}$$

Along one of the tube connections of the reservoirs, a `Filter` is placed in order to prevent clogging in the tubes by foreign particles which might enter the system via the openable `Reservoir A`. Directly after the `Filter`, a `Chiller` is placed and enables to adjust the temperature of the water flowing to `Reservoir B` and thus to the repeater cards. The second tube connection of the reservoirs is split into two paths, wherein each of the paths guides the water flow along four repeater cards. For each path, one of the four repeater cards is equipped with a temperature sensor (`TE670`, `TE671`). The cards are followed by two circulation pumps `P670`, one for each path, which suck water from `Reservoir A` along the tube connection and convey it back. When operated, all water-bearing parts of the system, apart from `Reservoir A`, are exposed to underpressure. As a consequence, in case of a leak, water cannot escape from the system, but air is sucked into it and consequently lowers the underpressure in the system causing the water to flow back into `Reservoir A`. During regular operation of the system, leakage is compensated by the vacuum pump.

5.2.2. PLC control system

As indicated in the foregoing section, the whole is system is controlled and monitored by a PLC. The system is integrated into the PLC environment of the liquid nitrogen cooling system for the detector modules. Consequently, it is also accessible via the ANIBUS client and thus can be comfortably controlled and monitored, also remotely. A very short and good introduction to PLC principles, the ANIBUS client and the MUSCADE® software suit, running all services, can be found in [32].

The control of the system is divided into two parts. On the one hand, there is one PLC cycle implemented which regulates the fill level of `Reservoir B` and a second cycle regulating the water circulation, which is dependent on the fill level regulation.

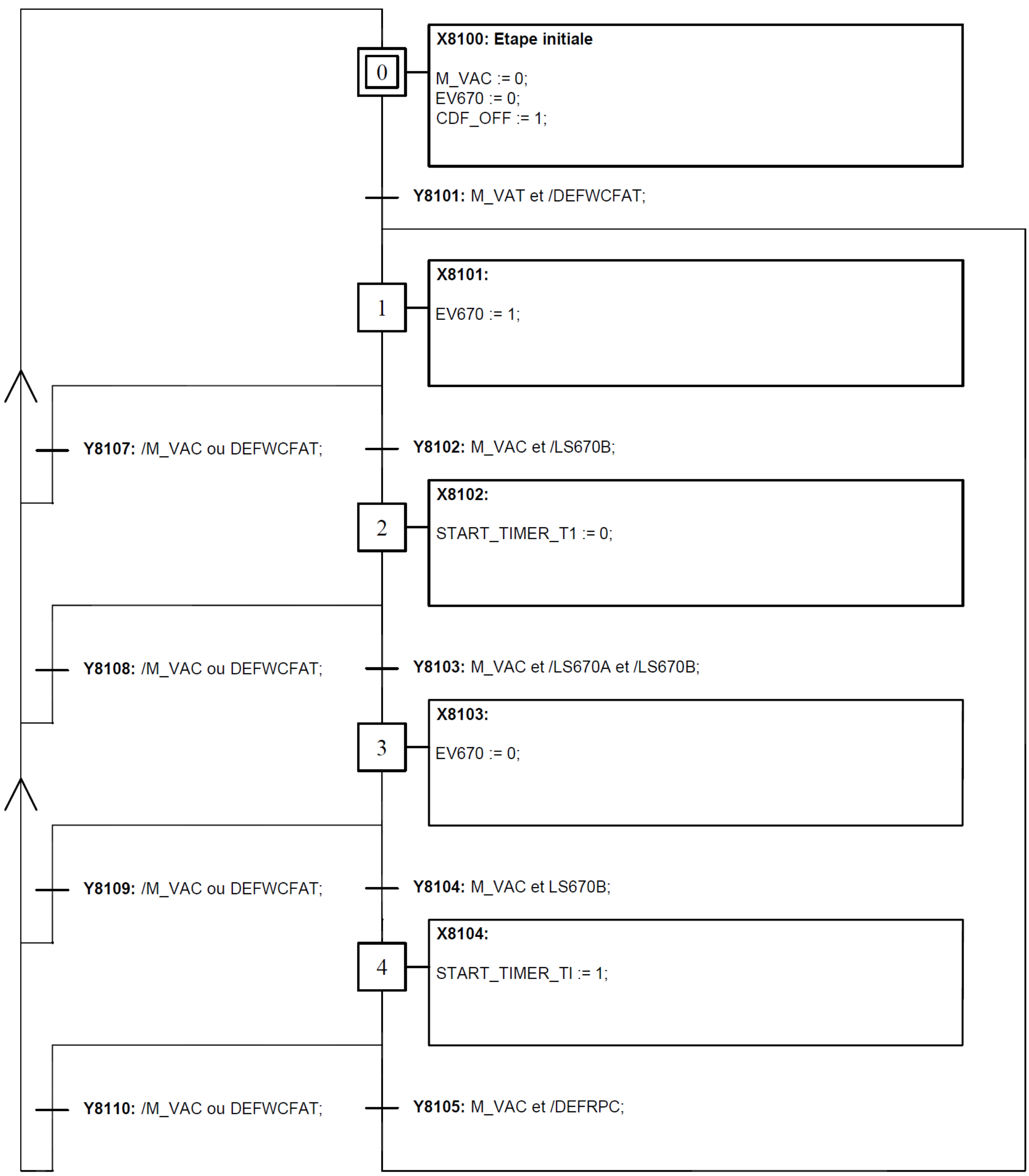

Figure 5.7.: GRAFCET of the fill level regulation

The working principle of the PLC cycle regulating the fill level of Reservoir B is shown as the employed GRAFCET[81] in Fig. 5.7. State X8100 is the initialisation of the fill level regulation, where the status bit M_VAC for regulating the fill level of Reservoir B is revoked and the magnet valve EV670 is closed for safety reasons. When the system is set from OFF to Standby or ON via ANIBUS (i.e. M_VAC is set) and if there are no critical errors[82], condition Y8101 is fullfilled and the system steps into state X8101 and magnet valve EV670 is set open. Opening valve EV670 means that an underpressure is created in Reservoir B, causing water stored in Reservoir A to rise.

Reservoir B is equipped with two water sensors LS670A and LS670B, which are opto-electronic devices with an integrated Schmitt-trigger. They are sensitive to the varying refractive index on their surface, thereby sensing the presence or the absence of water. With a response time of $50\,\mu$s [49], it is possible to precisely regulate the fill level. When both level sensors are registering water, condition Y8103[83] is fullfilled and the system steps into state X8103 and closes magnet valve EV670 again, Reservoir B is filled to capacity.

The system now stays in step X8103 until the fill level of Reservoir B has fallen under the niveau of the lower level sensor LS670B due to leakage in the system. With Reservoir B being almost out of water, condition Y8104 is fulfilled and the system steps back into step X8101[84], starting a new regulation cycle.

As one can see on the left side of the GRAFCET, the regulation can be interrupted at any time, by either revoking the status bit M_VAC via ANIBUS or in the event of a critical error DEFWCFAT. Furthermore, stepping into a new state is only possible if no critical error DEFECFAT is present.

Fig. 5.8 shows the PLC cycle for regulating the water circulation, wherein initial state X8200 of the circulation regulation is built similar to initial state X8100 of the fill level regulation. The status bit M_CIRC for the circulation is revoked and circulation pumps P670 are set to off. A big difference to the fill level regulation is that the circulation regulation cannot work independently from the fill level regulation. As can be seen in condition Y8101, the status bit M_CIRC of the circulation regulation and the status bit M_VAC of the fill level regulation have to be set for proceeding to the next state X8201. This safety measure was taken to protect the circulation pumps of running without water in the system which can potentially damage them. State X8201 is a standby state for

[81] **GRA**phe **F**onctionnel de **C**ommande **E**tapes/**T**ransitions; specification language to visualize procedure descriptions, which is favored in France

[82] combined in group error DEFWCFAT

[83] condition Y8102 and state X8102 are omitted since they are leftovers from a previous version of the regulation, which were not removed from the code used at COMPASS due to a lack of time at the beginning of the beam time. They do not affect the regulation.

[84] Again, state X8104 and condition Y8105 are omitted as they are leftovers of a previous version of the code and since they do not affect the behaviour of the system.

the circulation regulation, wherein the regulation is waiting until `Reservoir B` is filled with water, i.e. level sensors `LS670A` and `LS670B` indicate water in the reservoir. If these conditions (`Y8202`) are fulfilled, the system steps in state `X8202` and circulation pumps `P670` are switched on. The system stays in this state until `Reservoir B` is almost empty, which is indicated by level sensor `LS670B`, and then steps back into stand-by state `X8201`.

As in the fill level regulation, the circulation regulation can be interrupted at any point by revoking the respective status bit `M_CIRC` or by presence of a critical error `DEFWCFAT`.

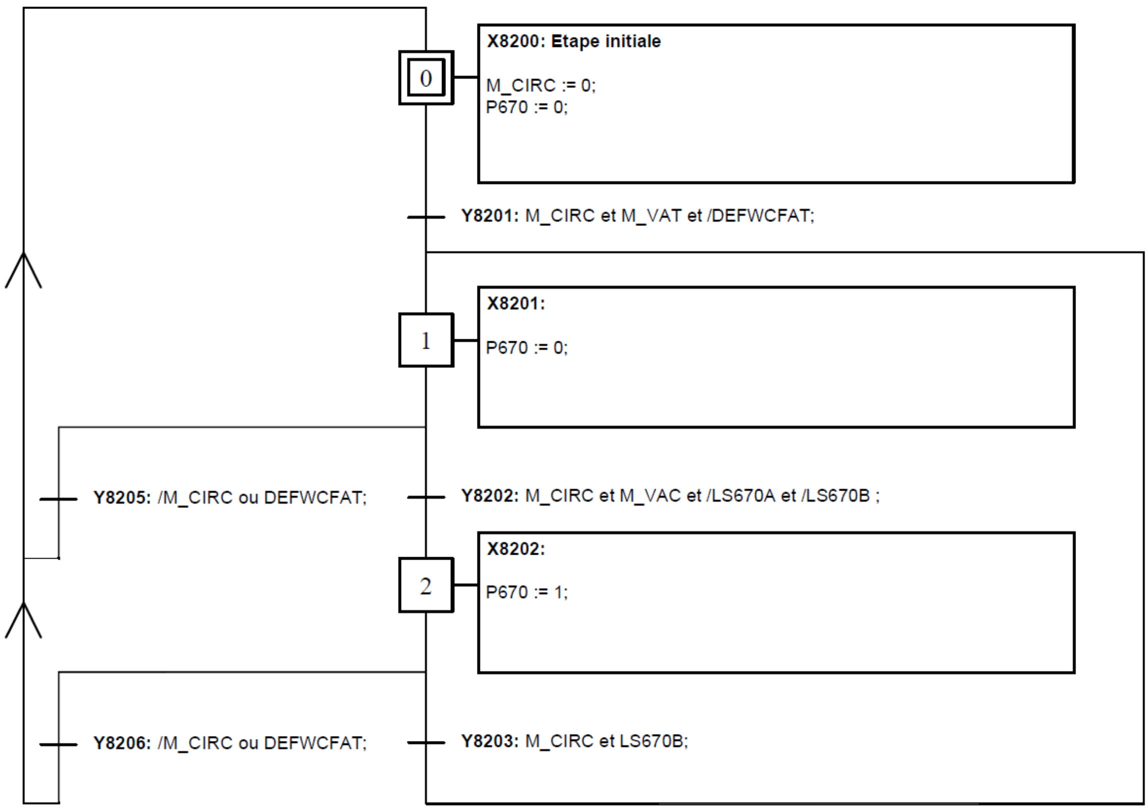

Figure 5.8.: GRAFCET of the circulation regulation

The PLC further reads two Pt100 temperature sensors (not shown in the GRAFCET) which are used for temperature monitoring. There are several temperature thresholds causing alarms and critical errors, e.g. reporting the failure of one of the water sensors `LS670A` or `LS670B`. Moreover, if the temperature on one of the monitored repeater cards exceeds a certain threshold, the APV-chips of all detectors planes in the conical cryostat are switched off.

5.2.3. Cooling plates

The design for the cooling plates (see Fig. 5.9) was adapted from the existing design of the cooling plates for the passively cooled repeater cards of the upstream stations. To protect the circuits on the boards, it was decided to cover both sides of the repeater cards with a plate, though with regards to cooling covering only the front side would be enough. Furthermore, the cylindrical heat-conductor thermally connecting both plates was kept to allow a cooling with air in case of problems or failure of the water cooling. Since the voltage regulators' ground is on HV, the voltage regulators need to be electrically insulated. This is done by two plastic pads spaced between voltage regulator and front plate, the pads are covered with white paste to improve heat conduction.

The front plate, covering the heat emitting part, is a 0.3 mm thick copper plate equipped with a U-shaped copper pipe having a diameter of $d_1 = 1/8''$. Two versions of the front plates exist: a short-pipe version, with a pipe length of $l_1 = 211\,\mathrm{mm}$, installed on the repeater cards mounted to the conical cryostat, and a version having longer pipes of $l_2 = 259\,\mathrm{mm}$, serving as spares. The pipe is arranged such, that it covers the plate areas on top of the voltage regulators. By extending the pipes by 48 mm more cooling power is provided to the heat emitting region sitting underneath the U-bend of the pipes. For the short pipe version, the pipes were glued to the plates using thermal adhesive, whereas the pipes were soft-soldered to the plate for the long pipe version. This was done because during the installation of the cards it turned out that the adhesion of the glue was rather limited, making the handling complicated.

5.2.4. Dimensioning

Dimensioning the system was based on several assumptions since only estimates for the thermal losses of the voltage regulators are available. It was already mentioned that the CAEN modules supply at maximum a current of $I = 1.7\,\mathrm{A}$ at $U = 3.45\,\mathrm{V}$ to a repeater card. Based on these values, it is possible to calculate the maximum power going through the voltage regulators of one card:

$$P = U \cdot I = 5.87\,\mathrm{W} \tag{5.3}$$

Since the CAEN module is the only power input of the voltage regulators, it was assumed that the maximum thermal power dissipation of the regulators is $P = 5.87\,\mathrm{W}$ since the heat output of the system cannot be higher than it's power input. A second assumption used for the dimensioning was, that all thermal power is transported through the copper plate, which seems reasonable due to the high heat transfer coefficient of copper $\alpha_{Cu} = 1.31\,{}^{W}/_{\mathrm{mm^2K}}$[85]. Having highly thermally conducting material, namely the

[85]for a 0.3 mm thick copper plate

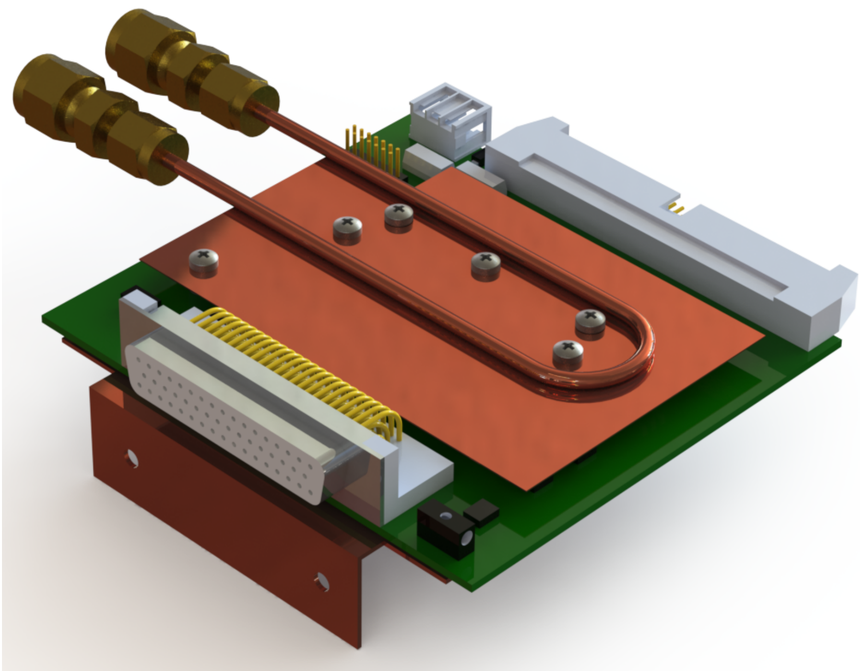

Figure 5.9.: Perspective CAD view of a water cooled repeater card (long pipe version, with Swagelok® connectors)

heat conducting glue or the brazing solder, as joints between copper plate and copper pipe, it was further assumed that no noteworthy thermal resistance between cooling pipe and heat source exists. Based on these assumptions, the necessary water flow for transporting away the incoming heat can be calculated:

$$\dot{Q} = \dot{m} \cdot c_{water} \cdot \Delta T \tag{5.4}$$

Having four repeater cards along each path, the total thermal power to transport is $\dot{Q} = 4 \cdot P = 23.5\,\mathrm{W}$ per path. Limiting the temperature difference ΔT of the cooling water from the first to the fourth card for each path to $\Delta T = 2\,\mathrm{K}$, one is able to calculate the necessary mass flow $\dot{m}$ from equation 5.4:

$$\dot{m} = \frac{\dot{Q}}{c_{water} \cdot \Delta T} = 2.81\,{}^{g}\!/\!_{\mathrm{s}} \tag{5.5}$$

Using the definition of the mass density ρ and generating its time derivative, it is possible to calculate the necessary volume flow:

$$\rho = \frac{m}{V} \Rightarrow V = \frac{m}{\rho} \tag{5.6}$$

$$\dot{V} = \frac{\dot{m}}{\rho_{water}} = 2.81\,{}^{cm^3}\!/\!_{\mathrm{s}} \text{ with } \rho_{water} = 0.998\,{}^{g}\!/\!_{\mathrm{cm}^3} \tag{5.7}$$

$$\Rightarrow \dot{V} = 10.12\,{}^{l}\!/\!_{\mathrm{h}} \tag{5.8}$$

The system installed at COMPASS provides a volume flow of 12 l/h for each path, being slightly above the necessary flow for safety reasons. The overall performance of the system is discussed in the next chapter.

5.3. Performance during the 2012 Primakoff run

For the discussion of the overall performance of the water cooling system, the temperature profile throughout the Primakoff beamtime is a valuable source of information. In Fig. 5.10 the temperature profile of the two monitored repeater cards (TE670, TE671) and the temperature profile of the experimental hall (TEDCS[86]) are plotted. One can see that the temperatures of the repeater cards mostly stay within 31 − 34 °C and roughly follow the trend of the hall temperature. Furthermore, one finds that the most significant changes in the repeater cards' temperatures are due to the night/day changes of the experimental hall's temperature. Hereby, it is worth mentioning that the night/day temperature oscillations are attenuated on the repeater cards compared to the oscillations of the environmental temperature. The average temperature of the repeater cards throughout the beamtime were around 32 °C with an RMS of approx. 1 °C.

Point	$\overline{T}$ [°C]	RMS [°C]
TE670	32.0	1.1
TE671	32.1	1.1

Table 5.1.: Temperature characteristics throughout the Primakoff run

Furthermore, it is important to note that the plotted hall temperature is not exactly the temperature inside the RPD. Comparing TEDCS with the measured values on the repeater cards during e.g. MDs[87], where the system was in `OFF` or `Standby` mode and the power supply to the repeater cards was interrupted (i.e. the measured temperature was basically the environmental temperature), it turned out that the temperature inside the RPD is actually 3 °C above TEDCS.

Taking into account that the temperature profiles of the two monitored repeater cards roughly follow the temperature profile of the experimental hall and that the average temperatures on the cards are close to the temperature inside the RPD, one may conclude that the position of the `Chiller` within the cooling circuit was not ideal. The cool water leaving the chiller (≈ 22 °C) had to pass along a tube to `Reservoir B` and from there to the repeater cards. This corresponded to a significant heat input from the surrounding environment since the flow in the system was rather low (i.e the water needs

[86]Measured on the gallery of the experimental hall. Values taken from COMPASS DCS.
[87]**M**achine **D**evelopment; regular intermissions of the beam distribution to COMPASS due to work on the SPS accelerator.

quite some time to reach the repeater cards). Swapping the circulation pumps `P670` with the `Chiller` and inverting the flow direction in the system might have improved the cooling of the repeater cards since the cool water leaving the `Chiller` would have been guided directly to the repeater cards, lowering the heat input from the environment.

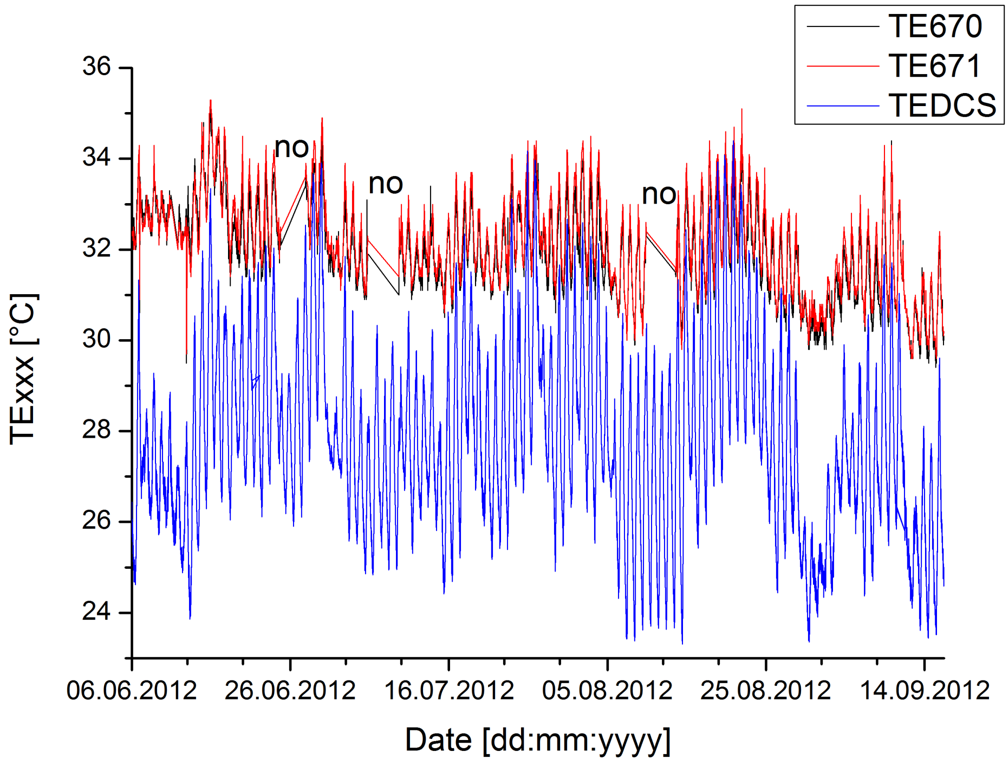

Figure 5.10.: Temperature profile for the monitored repeater cards and the experimental hall throughout the Primakoff run. "no" designates periods where either the water cooling system or the repeater cards were not operated.

After discussing the overall performance during the Primakoff run, focus shall be layed on the system's dynamic range. Fig. 5.11 shows the temperature profile for a cool down performance test conducted on May, 11th. At the beginning of the test (∼19:45), the APV chips were off and the water cooling system was in `Standby` mode, causing a temperature of $T \approx 30\,^{\circ}\mathrm{C}$ on both monitored repeater cards. In a second part of the performance test, the APV chips were switched on and loaded and the system was kept in this situation for approx. 35 minutes (19:45 - 20:22). Fig. 5.11 nicely shows how the temperature on both repeater cards increases by approx. $20\,^{\circ}\mathrm{C}$. After the temperatures exceeded $47 - 49\,^{\circ}\mathrm{C}$, it was decided to switch on the cooling again, to prevent damage to the repeater cards. As can be seen nicely, the system reacts immediately and the temperatures on both repeater cards decrease promptly and smoothly on both cards[88]. The system could cool down the cards to the nominal operating temperature within 4 minutes (20:22 - 20:26), a performance considered satisfactory.

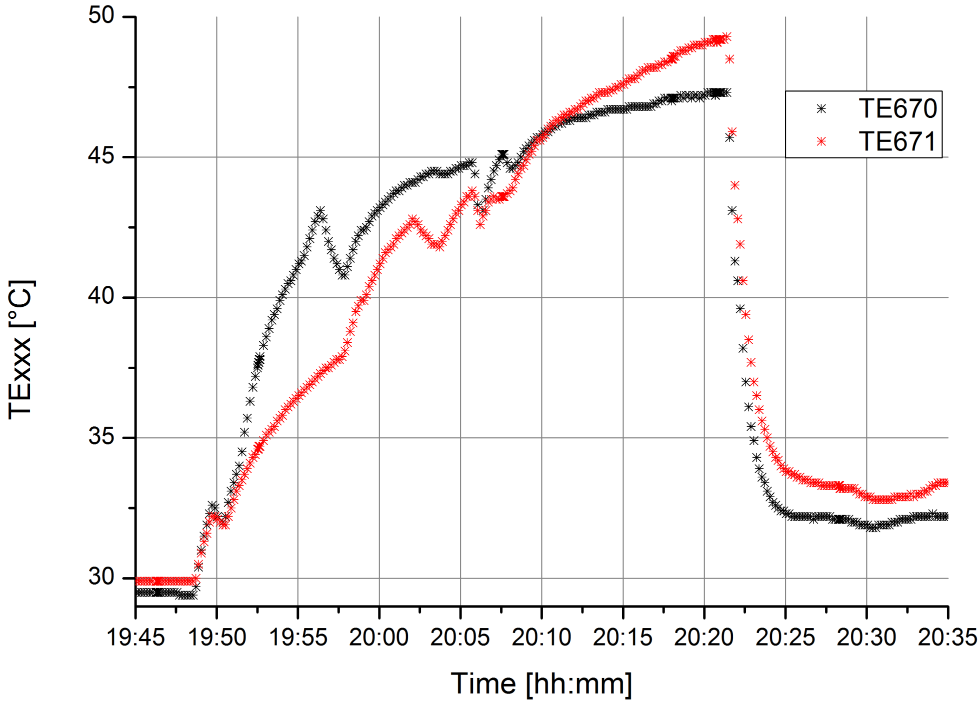

Figure 5.11.: Temperature profile for cool down performance test

Another point to consider when assessing the performance of the system is the leak rate Q of the system. It can be determined from the time between two openings of the magnetic valve `EV670`. The two level sensors determining the valve operation are spaced $\Delta h_{level} = 60\,\mathrm{mm}$ apart in height and together with the upper reservoir's base area of $A = 100 \times 100\,\mathrm{mm}^2$, this defines a volume $V_{leak} = 0.6\,\mathrm{l}$. During the whole run, the magnetic valve opened periodically every $t_{leak} = 40\,\mathrm{min}$. With these values, the leak rate for the water leaving `Reservoir B` can be determined:

$$Q_{fluid} = \frac{V_{leak}}{t_{leak}} = 0.9\,{}^{l}/_{\mathrm{h}} \tag{5.9}$$

[88]The offset between `TE670` and `TE671` is considered to have its roots in differing thermal contacts between the Pt100 temperature sensors on the copper plates due to their fixation to the plates with Kapton® tape.

This value corresponds to the leak rate for air entering `Reservoir B`, taking into account a pressure of $p = 800\,\mathrm{mbar}$[89] inside the reservoir:

$$Q_{air} = \frac{p \cdot V_{leak}}{t_{leak}} = \frac{800\,\mathrm{mbar} \cdot 0.6\,\mathrm{l}}{2400\,\mathrm{s}} = 0.2\,{}^{mbar\,l}/_{\mathrm{s}} \tag{5.10}$$

Looking at theses values, one has to point out that the leak rate is not satisfactory. During lab tests, the system was able to keep the water level between the level sensors for more than two weeks before it had to be dismounted and shipped to CERN. When equipping the conical cryostat with repeater cards at CERN and moving it to it's final position, it was discovered that the feedthroughs at the concial cryostat were not centered between the scintillator pair defining the gap for the repeater cards, as indicated in the technical drawings. Hence, it was not possible to install the repeater cards outside the RPD since they would have clashed with the housings of the scintillator's photomultipliers. Consequently, one was forced to install the cards after the conical cryostat was screwed to the marguerite. In this position, it is rather challenging to do the installation as there is only little workspace and special attention has to be paid to not inflict damage to the fragile beam window of the conical cryostat. Considering the laborious installation, it is assumed that one or more of the Swagelok® connections, which connect the copper pipes on the cards with the rubber tubes, are not tightened correctly. Due to a number of other problems at the beginning of the run, there was no resources to investigate and fix this problem and it was decided to go on with the system as it was.

5.4. Conclusions

Based on the experience at COMPASS concerning water cooling systems for front-end electronics, a water cooling system for the repeater cards of the silicon microstrip detectors was planned, designed, constructed and commissioned at COMPASS. The system described herein was able to meet all requirements and provided a stable operation of the front-end electronics throughout the whole 2012 Primakoff run. Even with an abnormally high leak rate, the problems with the HV insulation during the commissioning and despite the laborious installation at the conical cryostat, the operation in 2012 can be considered successful.

For future operation, the system may be expanded to the repeater cards of the upstream stations as well as to the ADCs, where a stabilized temperature could be beneficial as well. In case of cooling the ADCs, the cooling plate needs to be adopted to the ADC layout. For the upstream stations, the design presented within this thesis can be adopted unchanged since it has proven successful in 2012. Furthermore, expanding the system to other parts of the front-end electronics requires almost no work on the PLC

[89] For simplicity, the pressure inside `Reservoir B` is considered to remain constant.In reality, the underpressure in the reservoir decreases by roughly 3 %; which is considered negligible.

code, since the regulations themselves do not depend on the amount of equipment to be cooled. However, it will be necessary to add additional temperature sensors to monitor an expanded system and to remove legacy code from the PLC program.

6. Alignment studies for the 2012 Primakoff run

The silicon microstrip detectors are crucial for a precise vertex definition as they provide a spatial resolution better than $10\,\mu$m and as they are the first detectors downstream of the target. It was shown in [40] that a precise and run by run based alignment is necessary to make full use of the silicon microstrip detectors.

In the course of this chapter, the COMPASS alignment procedure will be described and results of the alignment studies for the 2012 Primakoff beam time will be presented.

6.1. The alignment procedure

6.1.1. Coordinate systems and formalism

Main reference system

The COMPASS main reference system ($Oxyz$) is spanned by a z axis oriented along the nominal beam axis, the y axis which is oriented vertically to the beam and upward and the x axis horizontal and perpendicular to the z axis, such that the system is orthogonal. The origin O was initially located at the COMPASS target center. But due to changes in the spectrometer setup, the origin is now located at an arbitrary position along the beam axis. The position of the Primakoff Ni target in 2012 is at $z = -67.2\,$cm.

Wire reference system

In addition to the main reference system, a local reference system, the so called wire reference system ($O'uvz$) is defined for each detector plane. The local z axis is equal to the z axis as defined in the main reference system. The u axis is oriented perpendicular to the detector strips and wires, respectively, and coincides with the coordinate measured by the detector, whereas the v axis goes parallel to the detector strips/wires. The local origin O' is defined by the intersection of the detector plane with the z axis.

Formalism

The COMPASS spectrometer alignment[90] consists of two separate alignment runs, one run recorded with spectrometer "magnets off" and one with "magnets on". In case of absence of the magnetic field, particle tracks can be approximated by straight lines, wherein effects like multiple scattering or any other interaction within the spectrometer are ignored. With the magnetic field present, one has to consider that the supports for some detectors (e.g. FI03 and F04; not used for Primakoff measurements) are slightly magnetic, causing them to move. Moreover, the magnetic field deflects the drift electrons in gaseous detectors (e.g. GM01, GM02 and GM03) which can be treated as an effective misalignment in u. In the presence of a magnetic field, particle tracks can no longer be treated as straight tracks but have to be approximated by bent curves. In order to be able to correct for these effects, an alignment with "magnets on" is necessary.

For an alignment performed with "magnets off", the mathematical description can be reduced to four parameters per track:

- (x_0, y_0) the position in a reference plane located at z_0
- $(t_{x,0}, t_{y,0})$ the tangent of the track angles with respect to the beam axis

With magnets on, small deviations δx_0, $\delta t_{x,0}$, δy_0, $\delta t_{y,0}$ need to be applied to the parameters as used for the magnets off case.

6.1.2. The alignment principle

The alignment is based on the values obtained from the position measurements of the surveying teams. These measurements have a precisions of 0.5 mm [51]. For an optimum performance of the spectrometer, an accuracy of roughly 10 % of the detector's spatial resolution is needed. For most detectors this transfers to position accuracy in the order of $50 - 100\,\mu$m and for the silicons to an accuracy $<1\,\mu$m. Hence, it is obvious that a good alignment is mandatory.

In order to achieve the desired precision, the alignment procedure uses the values of surveyors measurements as a basis and derives corrections to these values, resulting in an optimized spectrometer geometry description for track reconstruction. The mathematical principle forming the base of this optimization procedure is the minimization of the summed χ^2 of all χ_i^2 for all individual tracks[91] in a given sample of N tracks:

$$\chi^2 = \sum_{i=1}^{N} \chi_i^2 \tag{6.1}$$

[90] for further details see [50]

[91] χ_i^2 is the square of the ratio between the difference between the hit position measured by a detector plane i and the calculated position given by the track model, and the resolution of detector plane.

Each of the contributions χ_i^2 in Eq. 6.1 depends on the one hand on a different set of track parameters and on the other hand on a single set of alignment parameters. These alignment parameters represent the corrections to the values of the surveyors measurements. For COMPASS, the set of alignment parameters usually contains four corrections per plane:

- δu, the transverse offset of a detector plane along the local u axis;
- $\delta\theta$, the rotational offset of a detector plane in the wire reference system $O'uv$;
- δz, the longitudinal offset a detector plane along the beam axis z;
- δp, to correct for the nominal pitch.

When determining the quality of a calculated set of alignment parameters for each of the approximately 200 detector planes within the COMPASS spectrometer, relative and absolute criteria can be applied. Examples for relative criteria may be:

- the number of reconstructed tracks per event in the spectrometer,
- the χ^2 distribution for these tracks,
- the number of reconstructed vertices per event,
- the number of tracks per vertex,
- physics mass widths of reconstructed particles.

However, these criteria cannot be used for the minimization of the overall χ^2 since the expected values for a perfectly aligned spectrometer are not known. However, they may be used for a comparison of different sets of alignment parameters.

In contrast to that, absolute criteria are based on the distribution of the detector plane's residual in correlation with geometrical variables. The residual for a track is defined as:

$$\Delta u = u_{det} - u_{cal} \tag{6.2}$$

Here, u_{det} is the hit position in the detector measured in the direction perpendicular to its strips and u_{cal} is the hit position along the same axis for the reconstructed track. The quality of each of the used corrections can be evaluated considering an expression in Δu:

- δu by the distribution of its average value $\langle \Delta u \rangle$, which is sensitive to the transverse offset δu;
- $\delta\theta$ by $\partial \langle \Delta u \rangle / \partial v$, since the slope of the distribution of the average of u versus the hit position in the direction parallel to the detector strips v is sensitive to the rotational offset of the detector plane;

- δz and δp by $\partial\langle\Delta u\rangle/\partial u$, due to the fact that the slope of the distribution of the average of u versus the hit position perpendicular to the detector strips, as determined by the tracking, is sensitive to longitudinal misalignment and to uncertainties in the pitch.

The actual alignment procedure determines corrections for all detector planes simultaneously under the boundary condition of minimized distributions for $\langle\Delta u\rangle$, $\partial\langle\Delta u\rangle/\partial v$ and $\partial\langle\Delta u\rangle/\partial u$. For example, a track sample of $N = 1000$, four alignment parameters per track and the approximately 200 detector planes with four alignment parameters each makes it necessary to invert a matrix of the size 4800×4800 to minimise Eq. 6.1. However, taking advantage of the matrix structure with many zeros and using matrix manipulations [52], it is possible to reduce the matrix size to the number of alignment parameters. The number of alignment parameters is still a rather large number, but using these tricks, the matrix to invert is no longer dependent on the size of the track sample.

6.1.3. Run by run alignment

The run by run alignment consists of three consecutive steps. First, a physics alignment is done in order to roughly align the silicon detectors with the rest of the spectrometer. In a second step, the silicon alignment, only the silicon planes are aligned, with the rest of the spectrometer fixed. Furthermore, the pitch of the individual silicon planes is a free parameter for the silicon alignment, correcting for minimal misalignment of the silicon planes in z direction. In a last step, scintillating fiber detector FI01 is aligned, which was excluded from the track reconstruction for the silicon alignment[92].

6.2. Results

Fig. 6.1 shows the shifts of all silicon X-planes during week 35 of the 2012 beam time. As seen for 2008 [53] and 2009 [40] data, the movement of the silicon detectors seems to be correlated to the temperature inside the experimental hall. For runs using hadron beam ($t = 45 - 115\,\mathrm{h}$ in the plot), the shifts of the silicon plans are in agreement with the results obtained for previous years. Already for the run by run alignment of the 2009 Primakoff data, it was observed that the offsets are systematically higher for runs using muon beam. This may be explained by the different phase space for muon and hadron beams, which results in a different weighting of the tracking detectors and consequently in a slightly different positioning of the silicon detectors with respect to the rest of the spectrometer. However, in 2012 data the shifts of the silicon planes for runs using muon beam ($t = 0 - 45\,\mathrm{h}$ in the plot) are significantly higher: offsets up to $300\,\mu\mathrm{m}$ have been observed for X and U planes. Movements of this size due to thermal expansion are not

[92] see Section C.2 for the individual CORAL option files

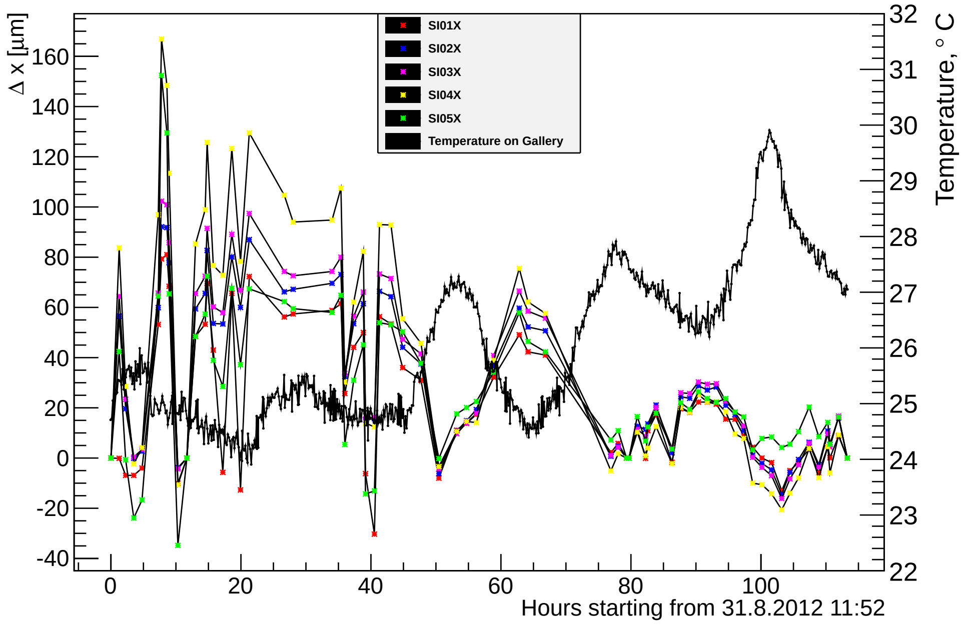

Figure 6.1.: Plane shifts W35 for X planes

realistic but hint to other reasons. Moreover, the shifts of the silicon planes don't seem to be correlated to the temperature inside the experimental hall.

The residuals of the silicon planes for alignment runs with artificially increased route widths and position uncertainties[93] for the silicon detectors do not show any suspicious characteristics (see Fig. C.1). But with route widths and position uncertainty set to zero, i.e. using the full resolution of the silicon detectors, the residuals have an abnormal distribution for silicon stations SI04 and SI05 (see Fig. C.2). While the residuals for station SI04 may be explained with reconstruction artefacts which are already known from previous years, the structure of the SI05 residuals is a yet unknown effect. For SI05, the residuals show a main peak and spaced apart a side peak with lower intensity.

Further investigations into these side peaks showed that the momentum distribution is the same as for the main peak (see Fig. 6.2(a) and Fig. 6.2(b)), whereas the distribution of the beam gradient Δy, which represents an angular distribution of the beam particles in y direction, is slightly different (see Fig. 6.4(b) and Fig. 6.4(d)). Moreover, the distribution of Δy does not have the expected shape. As shown in Fig. 6.4(f), the gradient has two components, whereas one would expect only one. The gradient distribution for the main peak shows both components, while the distribution for the side peak shows a suppressed contribution of the second component peaking at $\Delta y \approx -0.0008$ in Fig. 6.4(f).

[93] The default settings for CORAL.

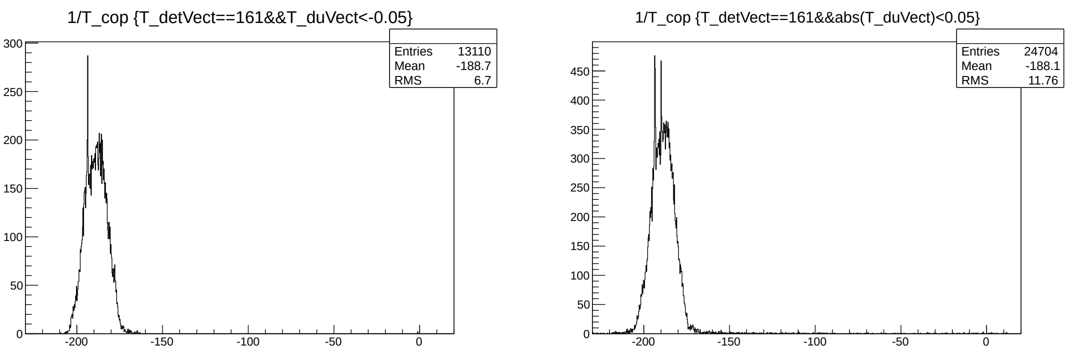

(a) Side peak

(b) Main peak

Figure 6.2.: Exemplary momentum distributions for muon beam as seen by SI05 X plane.

As shown in Fig. 6.3(a) and Fig. 6.3(b), the number of detector planes contributing to the reconstructed track differs for the main and the side peak. While the main peak is constituted by tracks with at least ten detector planes, the side peak has only tracks with more than approx. 30 detector planes hit. Both distributions show a peak at approx. 34 detector planes hit, while the distribution for the side peak shows a second peak at approx. 38 detector planes hit.

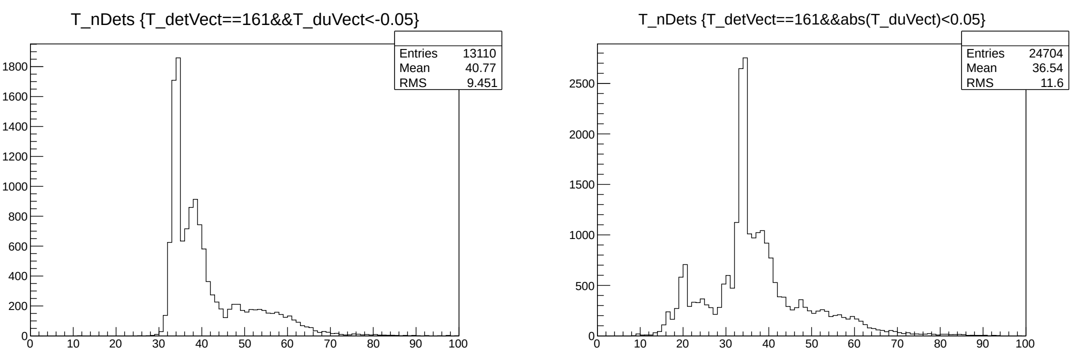

(a) Distribution of the number of tracks for the side peak

(b) Distribution of the number of tracks for the main peak

Figure 6.3.: Exemplary distribution of the number of detector planes contributing to a reconstructed track as seen by SI05 X plane.

For hadron beams, a small number of entries next to the main peak in the residuals for station SI05 can be observed, too. It is assumed that the number of entries for the hadron beam is much smaller due to the difference in phase space for muon and hadron beam. However, the entries in the hadron beam case do not form a second peak like for the muon beam, but form a more or less flat distribution. Furthermore, since the number of entries is comparably small, the effect on the shift of the planes seems negligible. Moreover, the gradients for the hadron beam do not show contributions from multiple components as it is the case for the muon beam.

Tests with a more "hadron beam like" muon beam, this means by restricting the tracks used for alignment to tracks with a gradient Δy between -0.0003 and 0.0009 and consequently cutting away the second component of the gradient in y direction, showed equivalent residuals, while the absolute values for the plane shifts slightly decreased. However, offsets up to $250\,\mu$m for X and U planes were observed.

Since these effects were not observed in the 2009 alignment [53] and moreover, taking into account the preliminary results of the efficiency studies for the 2012 Primakoff beam time [54], the effects might be related to reconstruction problems for the silicon detectors in CORAL since two planes of stations SI04 and SI05 were de facto destroyed during an HV incident during the commissioning phase. Further investigations on the impact of these more or less blind detector planes on the reconstruction are necessary. However, the preliminary alignment for the hadron data may be used for later mass production since the residuals, the shifts of the planes, the positions and the pitch corrections for the silicon detectors look reasonable.

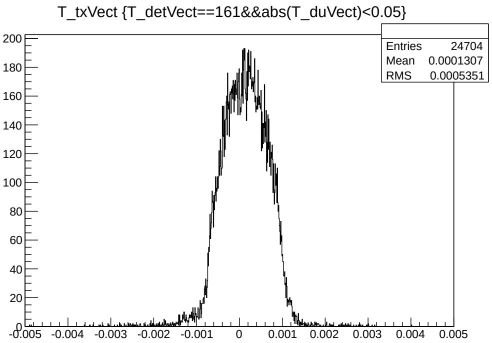

(a) Δx for the main peak

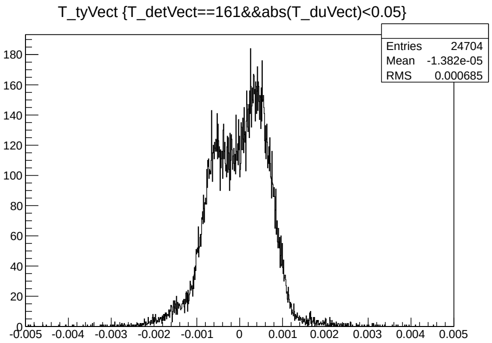

(b) Δy for the main peak

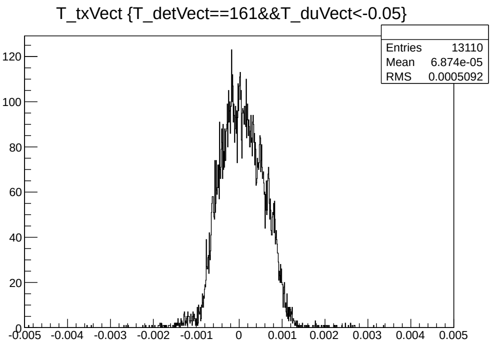

(c) Δx for the side peak

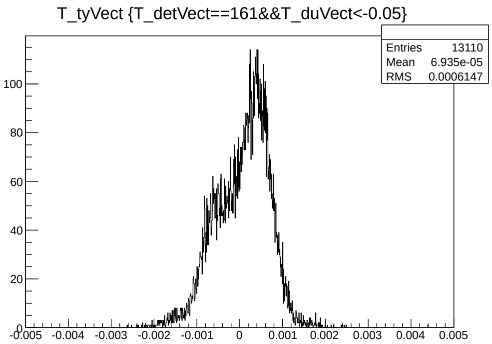

(d) Δy for the side peak

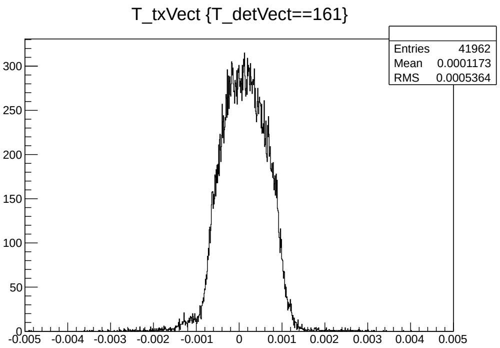

(e) Combined Δx

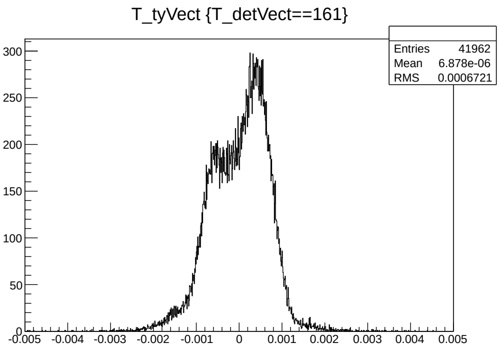

(f) Combined Δy

Figure 6.4.: Exemplary beam gradient distributions for muon beam as seen by SI05 X plane.

7. Conclusion and outlook

Over the course of this thesis, a new phase separator for the COMPASS silicon microstrip detectors was designed and constructed. Evaluation showed that the design with a detachable feedthrough for the electric connections concludes with the requirements. With it, a valuable alternative to the phase separators employed at COMPASS is given. Moreover, further improvements on the present design are proposed and may be tested in 2013 and 2014 when the silicon detectors will not be operated at COMPASS.

Additionally, a water cooling system for the repeater cards of the silicon microstrip detectors was designed and commissioned at COMPASS. Despite several challenges during the commissioning, the operation during the 2012 Primakoff beam time was successful. Looking ahead, the system may be used for the repeater cards of the upstream stations and moreover, the system may be expanded to ADC cards where a stabilized temperature is desirable as well.

Alignment studies for the 2012 Primakoff data have shown yet unknown residual distributions for the planes of silicon stations SI04 and SI05. Furthermore, unrealistic high shifts of the silicon planes for muon data have been observed in the run by run alignment. Together with preliminary results of the efficiency studies on the silicon detectors, the findings hint to problems with the reconstruction of the silicon detectors in CORAL, where the reconstruction may be affected by the two detector planes of silicon stations SI04 and SI05, which were seriously damaged by a HV incident during the commissioning phase. Further investigations on the impact of these planes on the reconstruction are necessary. However, the run by run alignment for hadron data may be used for later mass production as it looks comparable to run by run alignments of previous years.

A. Documentation of the modular phase separator

A.1. Components

Component	Supplier	Order number
Ease Release 205 release agent[94]	KauPo	09711-001-0010
fibre glass rod	TUM[95]	—
Pins	TUM[95]	—
Pt100 temperature sensors	TUM[95]	—
Stainless steel-/copper-body	TUM workshop	—
UHU PLUS ENDFEST 300	TUM workshop	—

Table A.1.: Components of the modular phase separator

[94]used for molding the epoxy feedthrough
[95]component recovered from other TUM project

A.2. Mapping

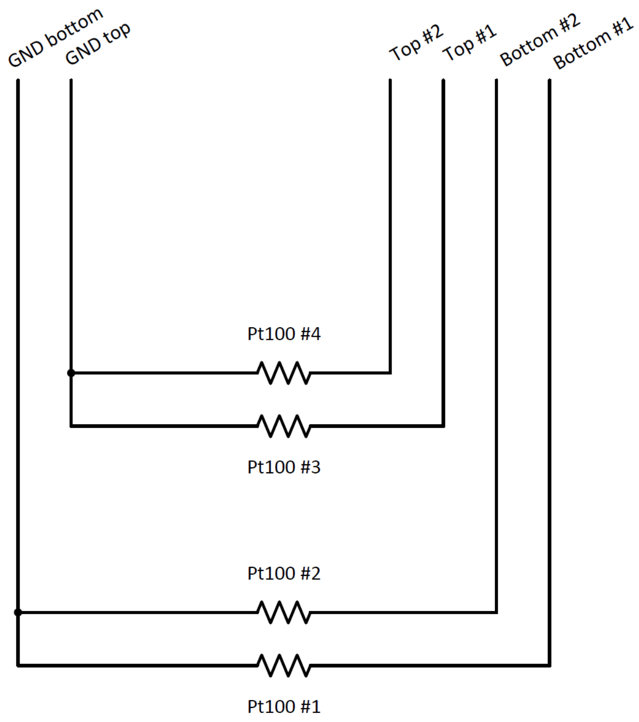

Figure A.1.: Wiring diagram of the modular phase separator. Labels on top correspond to the labels in Fig. A.2.

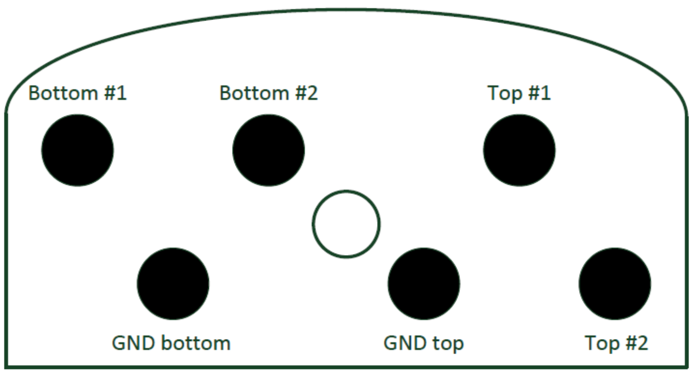

Figure A.2.: Pin-mapping of the feedthrough (seen from above)

A.3. Technical drawings

A.3.1. Modular phase separator


BENENNUNG:
Phasenseparator
Bernd Holzgartner, E18
A4
MASSSTAB:1:1
BLATT 1 VON 9

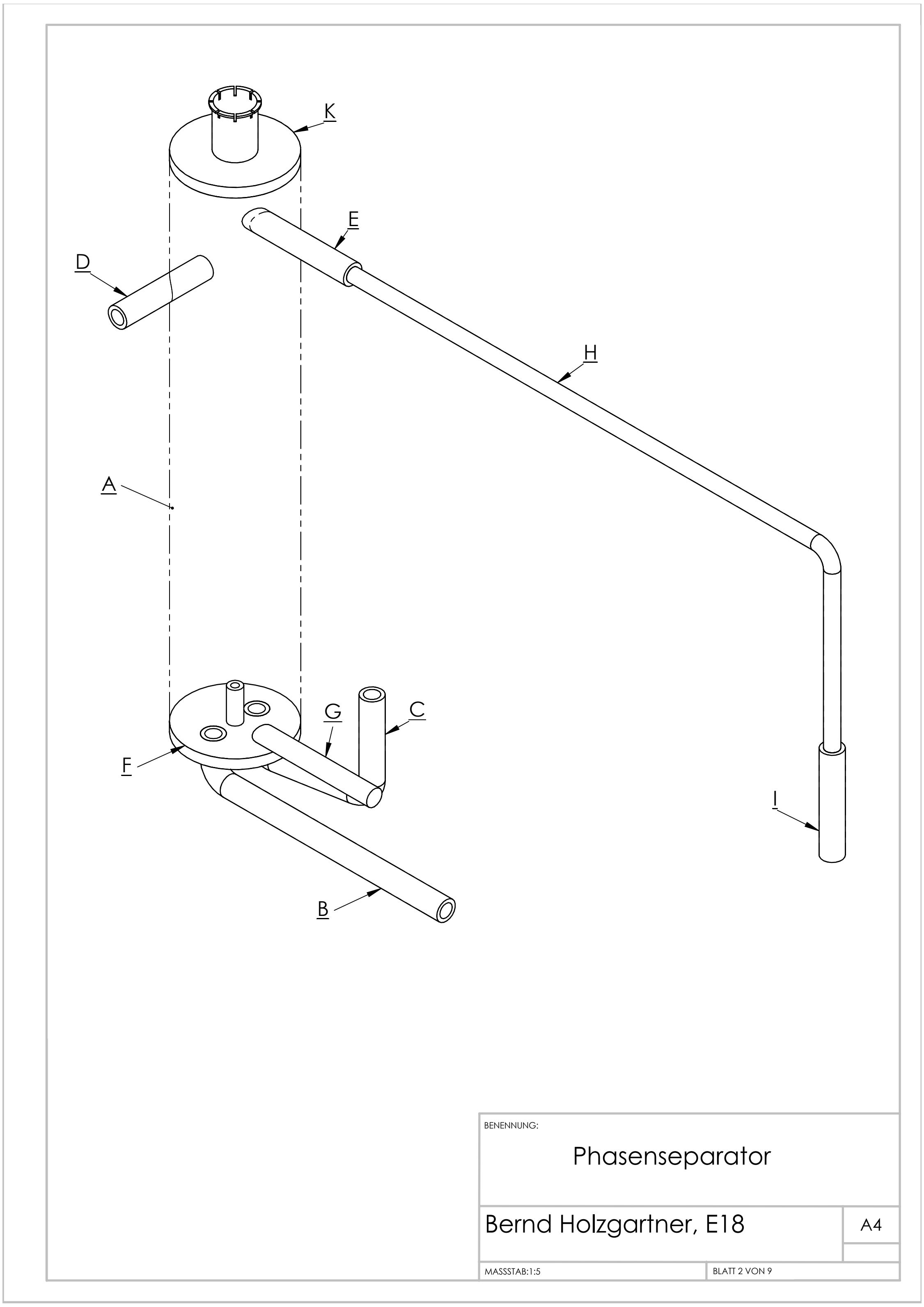
K
E
D
H
A
G
C
F
I
B
BENENNUNG:
Phasenseparator
Bernd Holzgartner, E18
A4
MASSSTAB:1:5
BLATT 2 VON 9

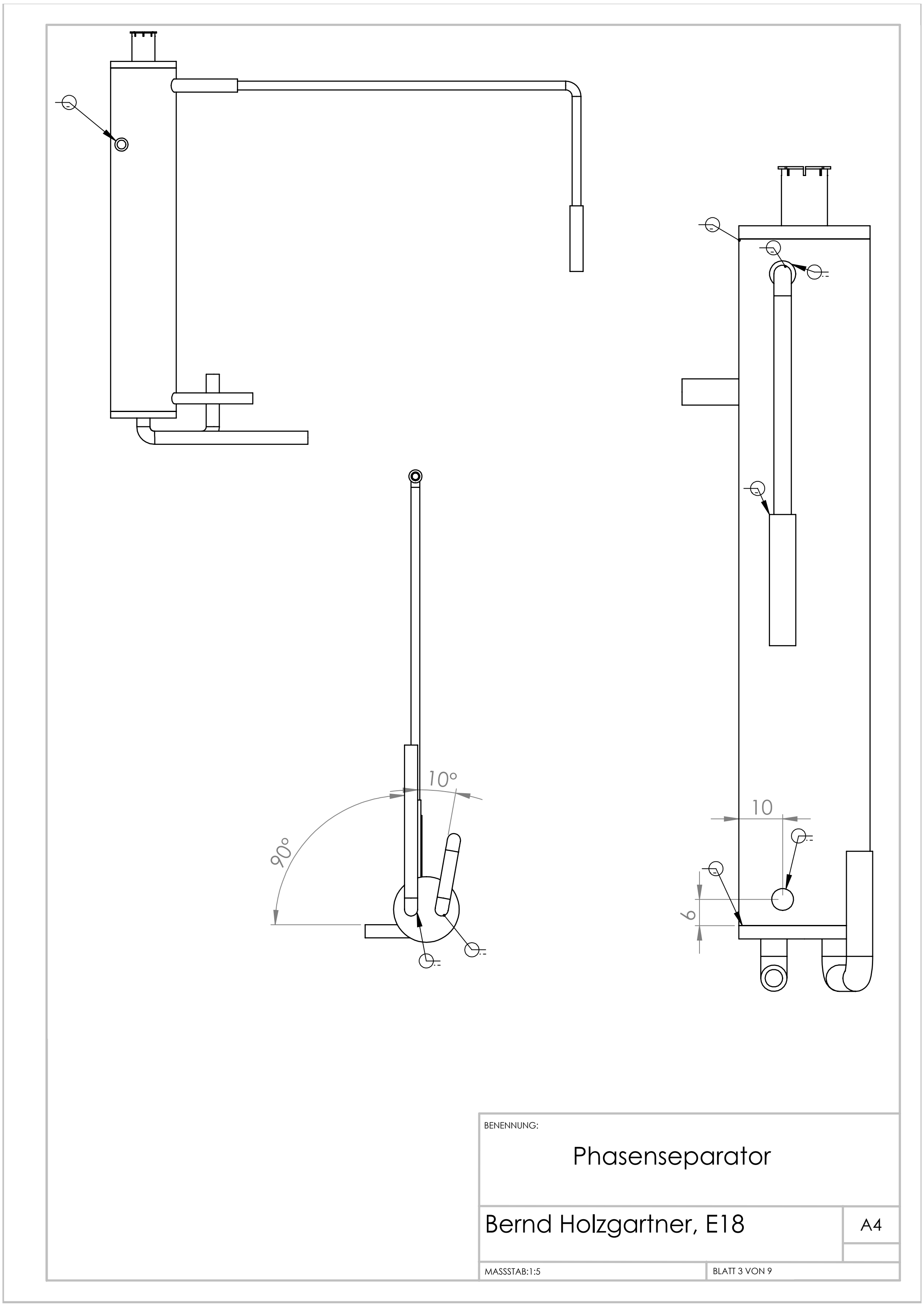
10°
90°
10
6
BENENNUNG:
Phasenseparator
Bernd Holzgartner, E18
A4
MASSSTAB:1:5
BLATT 3 VON 9

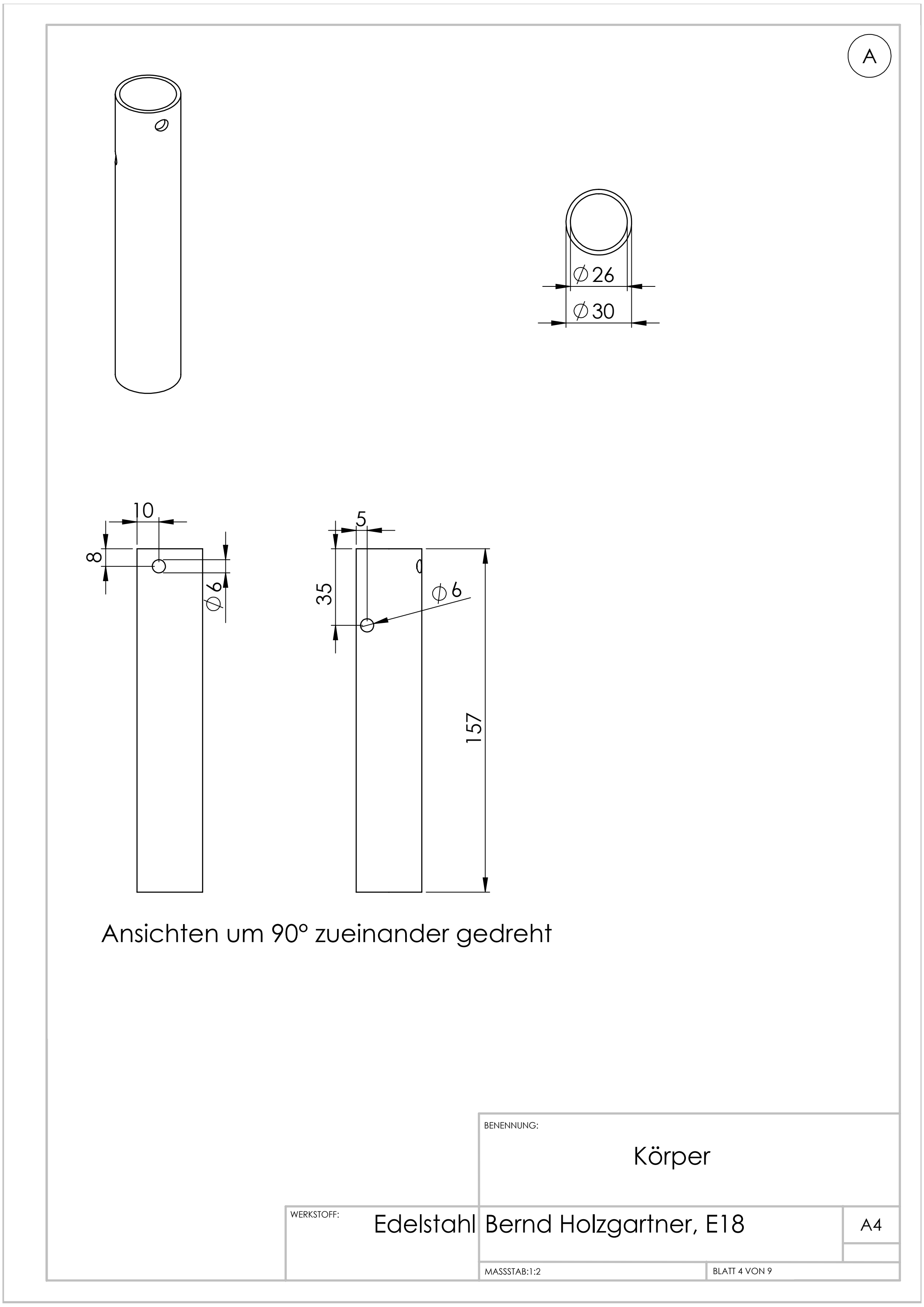
A
⌀26
⌀30
10
8
⌀6
5
35
⌀6
157
Ansichten um 90° zueinander gedreht
BENENNUNG:
Körper
WERKSTOFF:
Edelstahl
Bernd Holzgartner, E18
A4
MASSSTAB:1:2
BLATT 4 VON 9

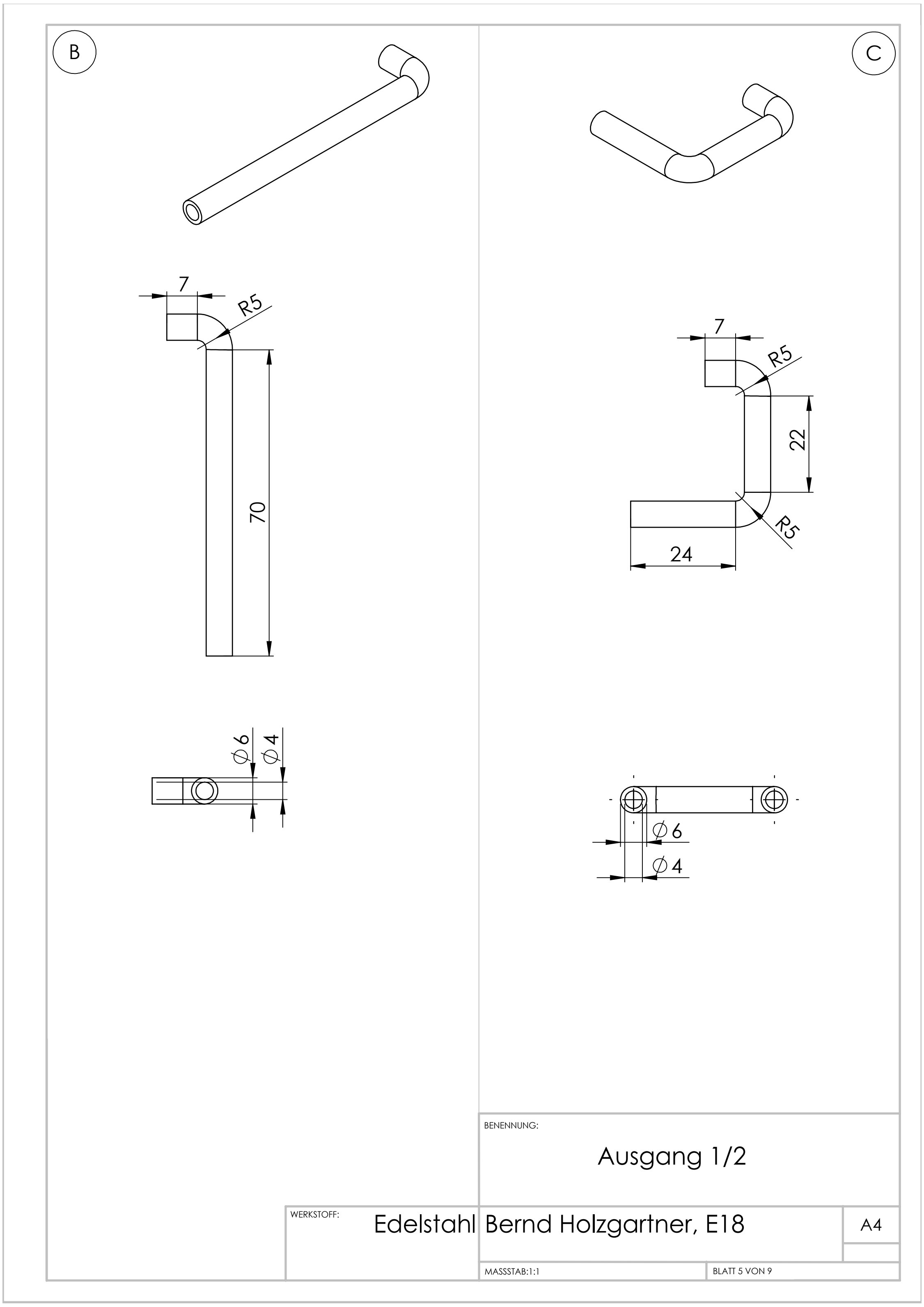
B
C
7
R5
70
⌀6
⌀4
7
R5
22
R5
24
⌀6
⌀4
BENENNUNG:
Ausgang 1/2
WERKSTOFF:
Edelstahl
Bernd Holzgartner, E18
A4
MASSSTAB:1:1
BLATT 5 VON 9

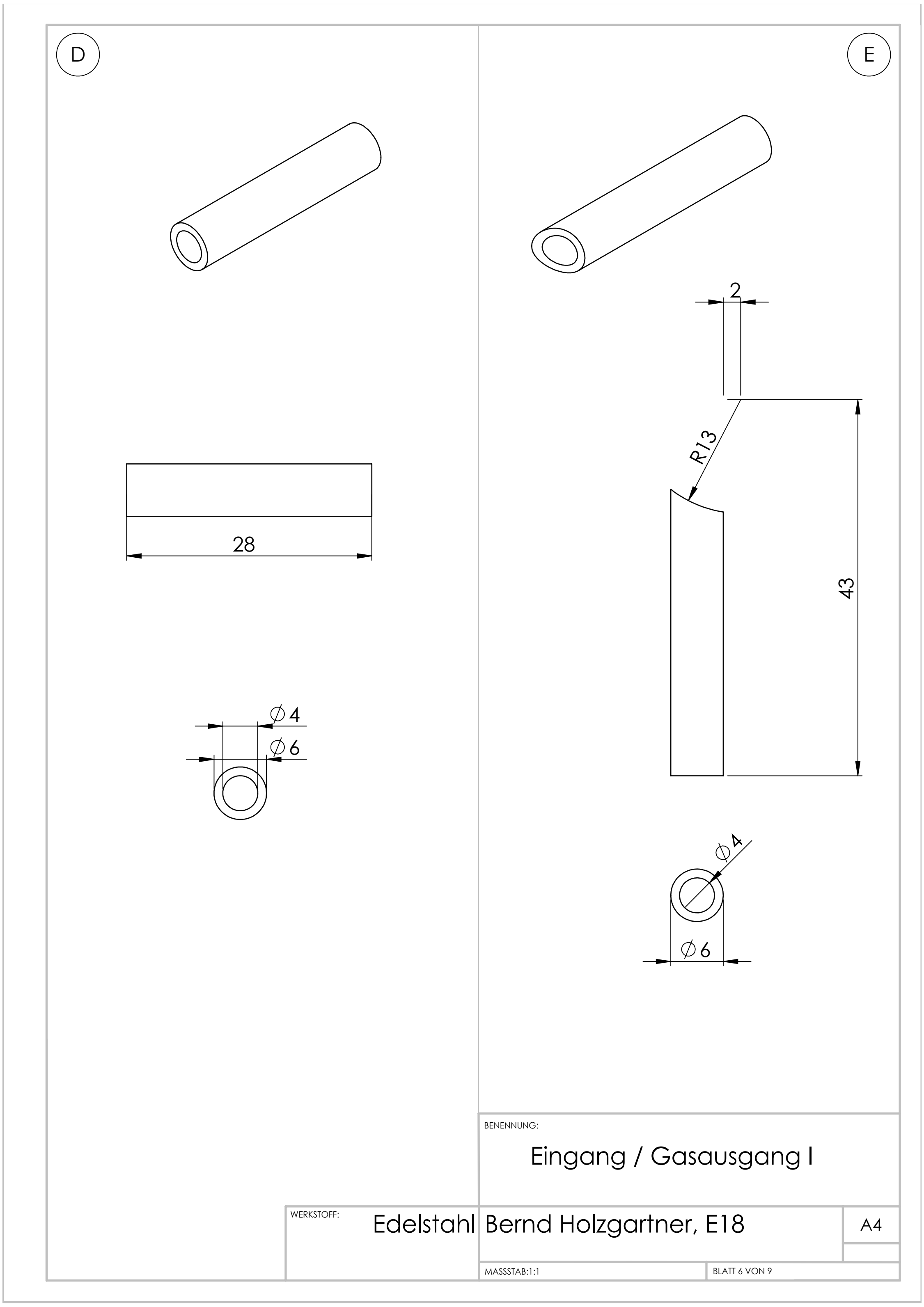
D
E
28
∅4
∅6
2
R13
43
∅4
∅6
BENENNUNG:
Eingang / Gasausgang I
WERKSTOFF:
Edelstahl
Bernd Holzgartner, E18
A4
MASSSTAB:1:1
BLATT 6 VON 9

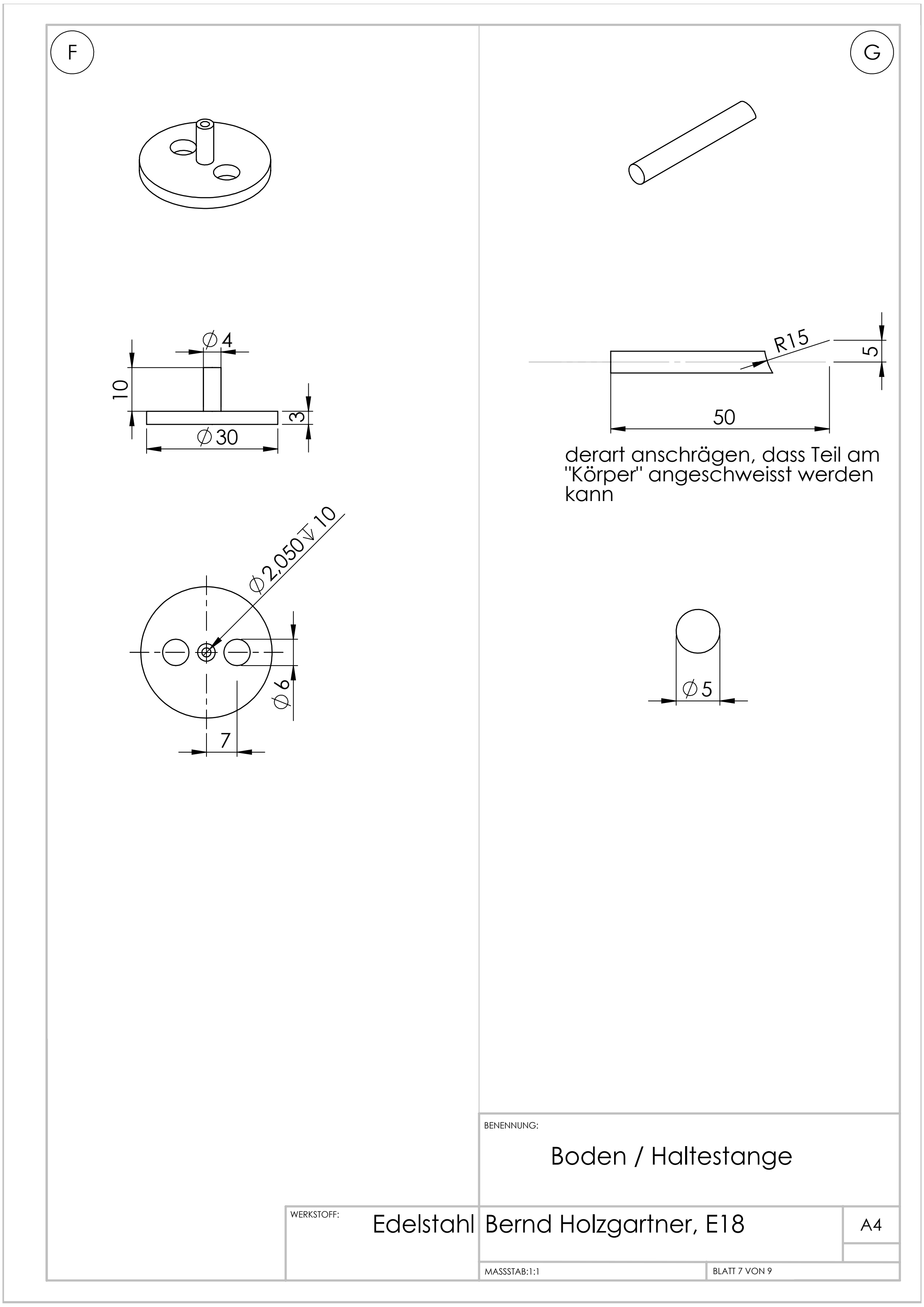
F
G
∅4
10
3
∅30
∅2,050 ↧ 10
∅6
7
R15
5
50
derart anschrägen, dass Teil am "Körper" angeschweisst werden kann
∅5
BENENNUNG:
Boden / Haltestange
WERKSTOFF:
Edelstahl
Bernd Holzgartner, E18
A4
MASSSTAB:1:1
BLATT 7 VON 9

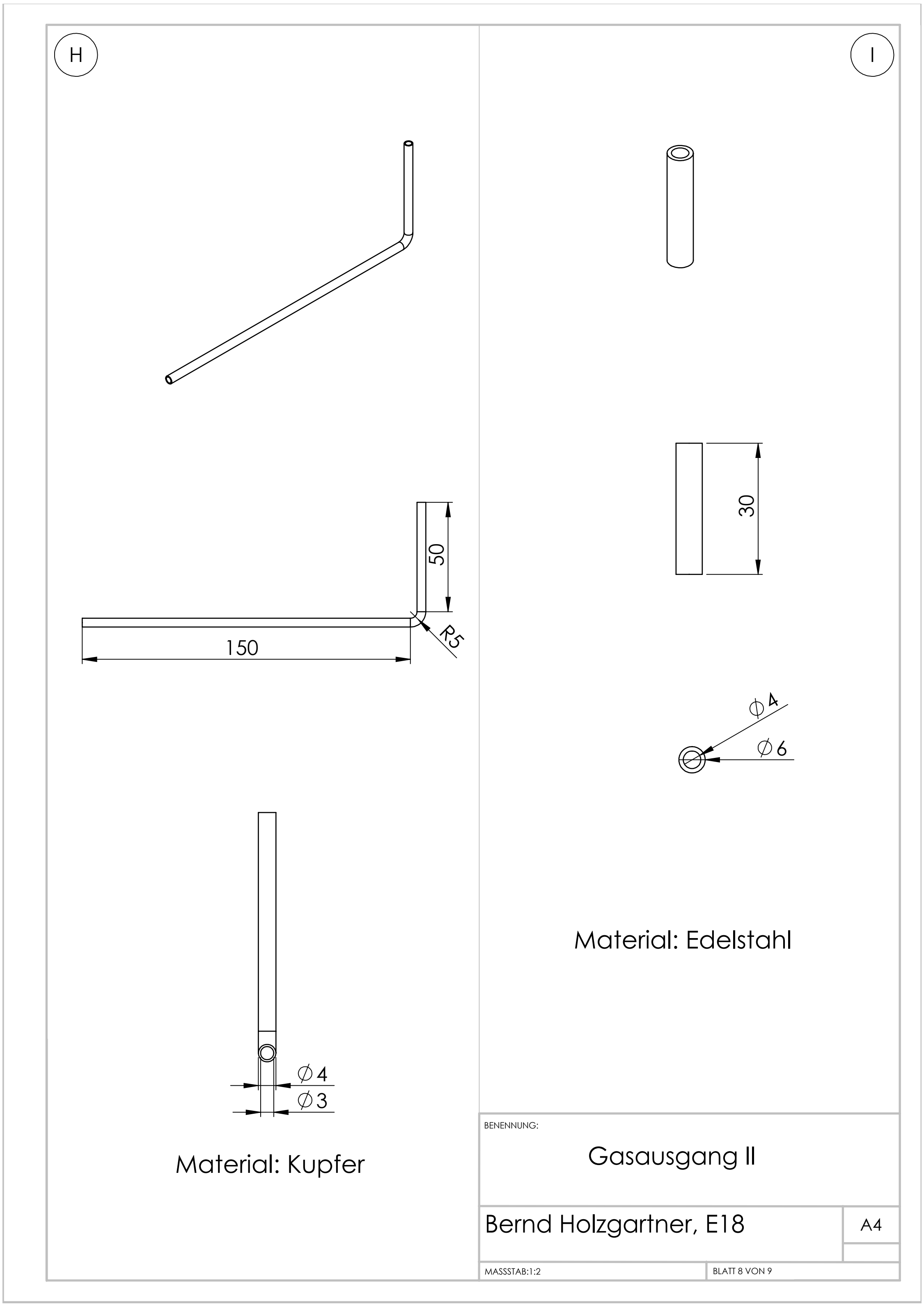
H
I
50
R5
150
30
∅4
∅6
∅4
∅3
Material: Edelstahl
Material: Kupfer
BENENNUNG:
Gasausgang II
Bernd Holzgartner, E18
A4
MASSSTAB:1:2
BLATT 8 VON 9

A.3.2. Molding assembly

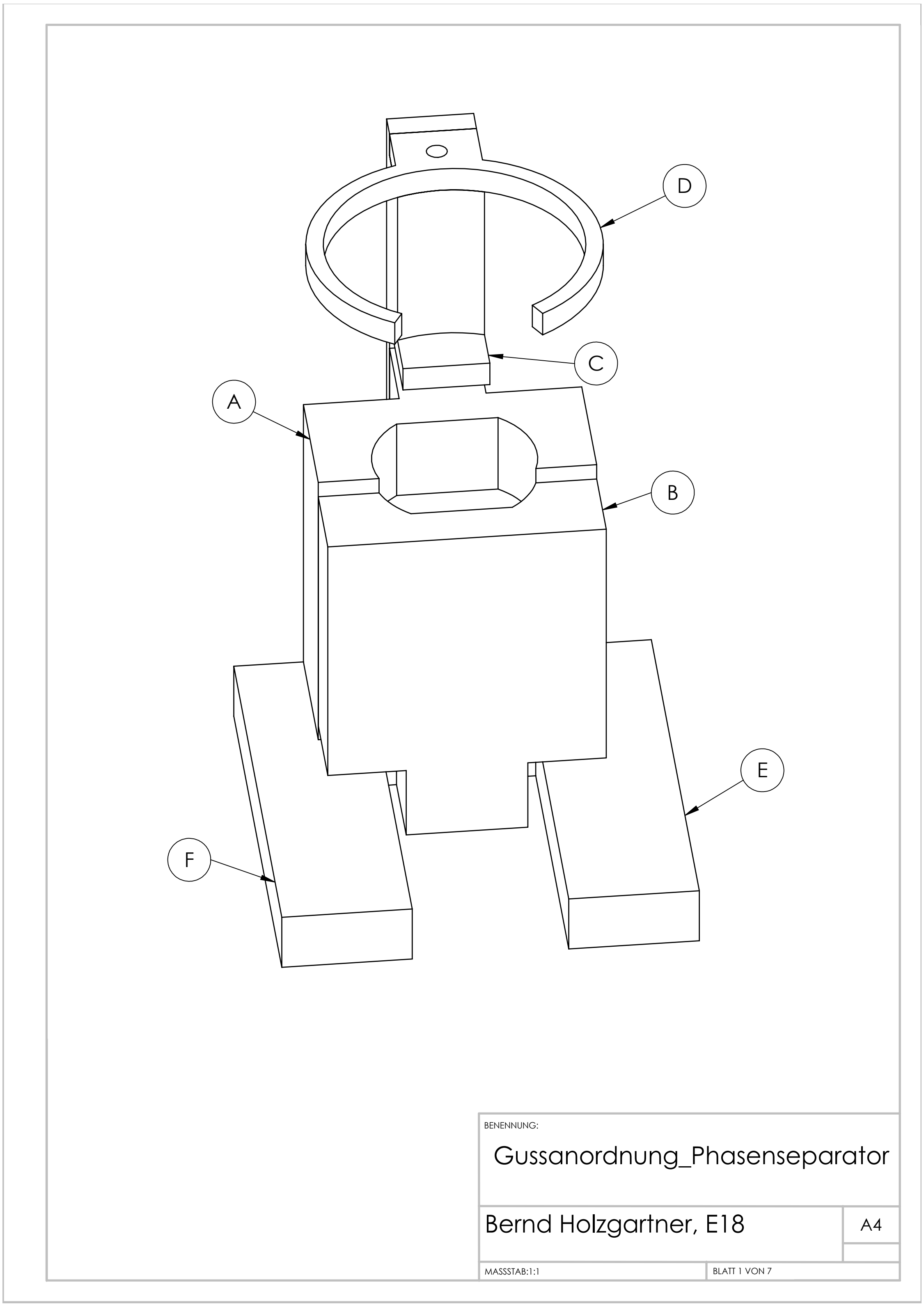
D
C
A
B
E
F
BENENNUNG:
Gussanordnung_Phasenseparator
Bernd Holzgartner, E18
A4
MASSSTAB:1:1
BLATT 1 VON 7

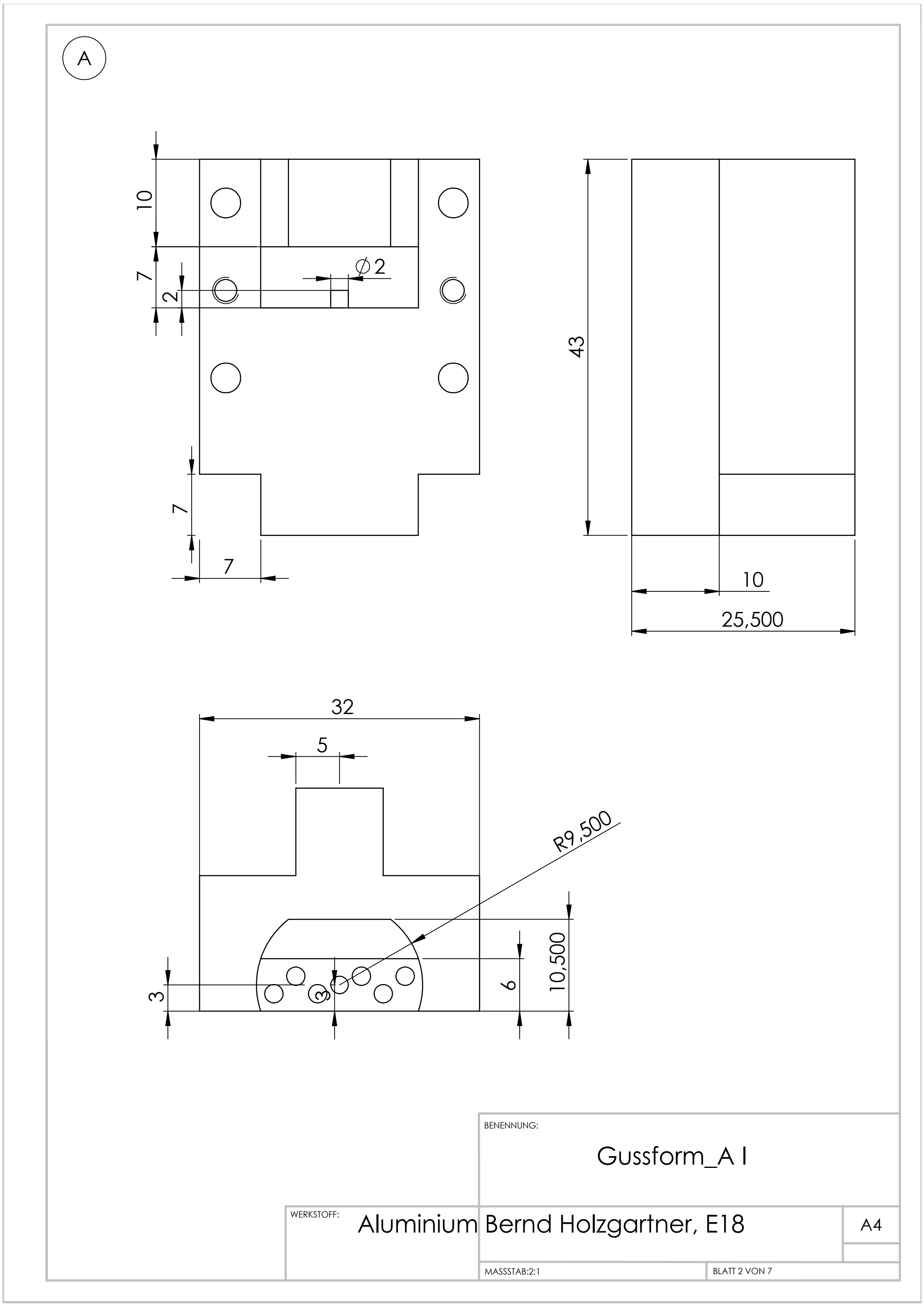
A
10
7
2
⌀2
43
7
7
10
25,500
32
5
R9,500
3
3
6
10,500
BENENNUNG:
Gussform_A I
WERKSTOFF:
Aluminium
Bernd Holzgartner, E18
A4
MASSSTAB:2:1
BLATT 2 VON 7

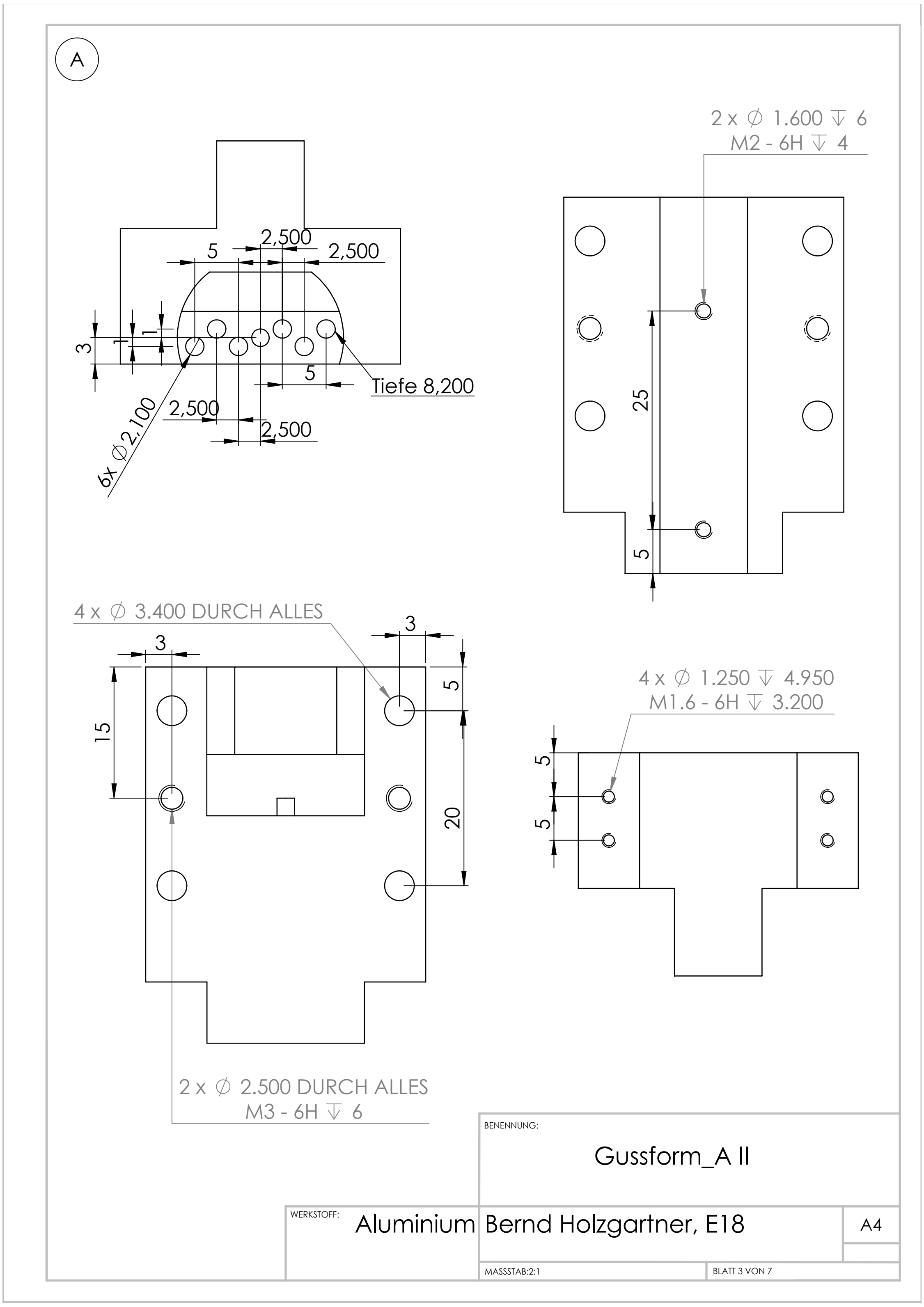
A
2,500
5
2,500
3
1
1
5
Tiefe 8,200
2,500
2,500
6x ∅2,100
2 x ∅ 1.600 ↧ 6
M2 - 6H ↧ 4
25
5
4 x ∅ 3.400 DURCH ALLES
3
3
15
5
20
4 x ∅ 1.250 ↧ 4.950
M1.6 - 6H ↧ 3.200
5
5
2 x ∅ 2.500 DURCH ALLES
M3 - 6H ↧ 6
BENENNUNG:
Gussform_A II
WERKSTOFF:
Aluminium
Bernd Holzgartner, E18
A4
MASSSTAB:2:1
BLATT 3 VON 7

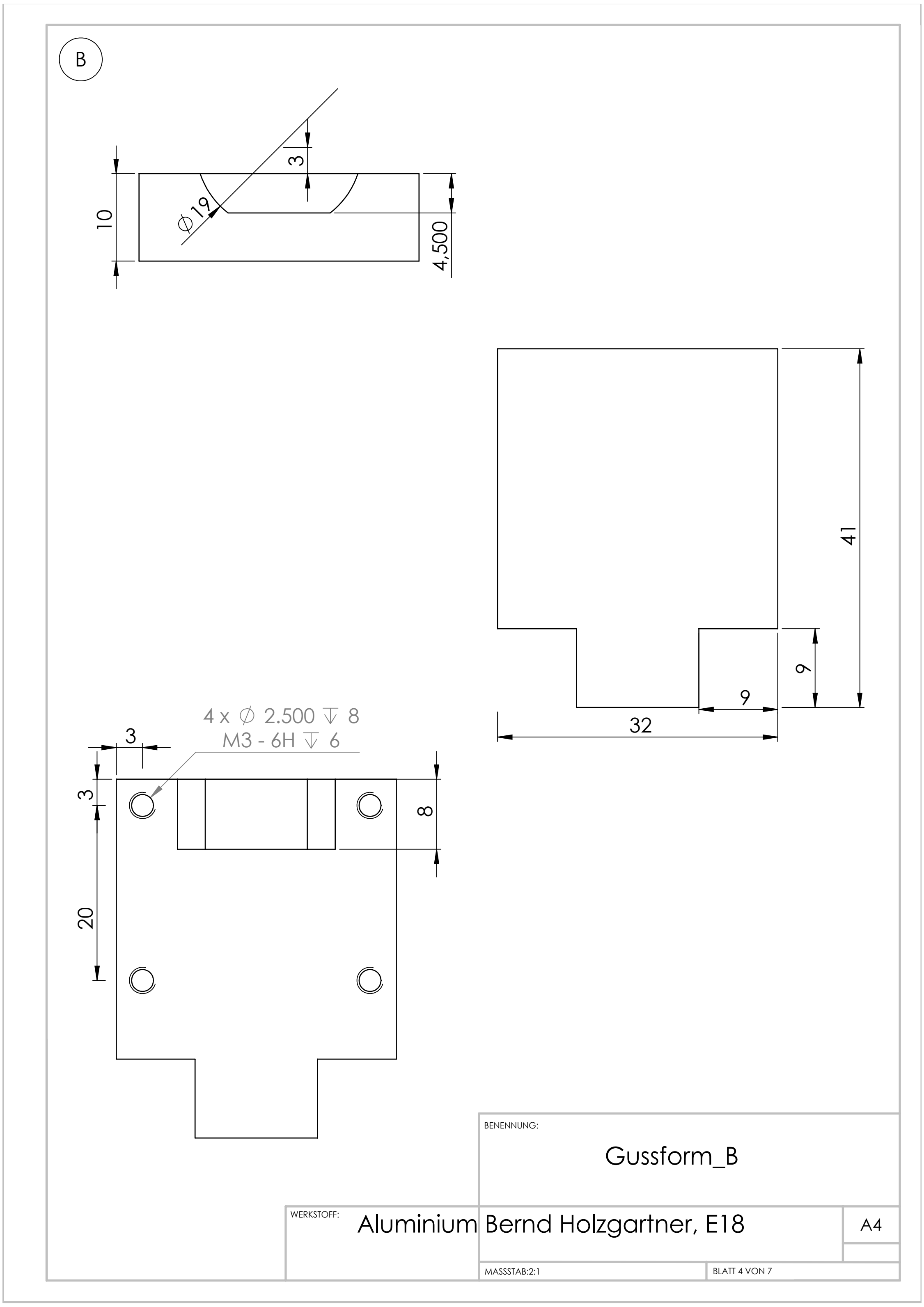
B
3
10
Ø19
4,500
41
9
9
32
4 x Ø 2.500 ↧ 8
M3 - 6H ↧ 6
3
3
8
20
BENENNUNG:
Gussform_B
WERKSTOFF:
Aluminium
Bernd Holzgartner, E18
A4
MASSSTAB:2:1
BLATT 4 VON 7

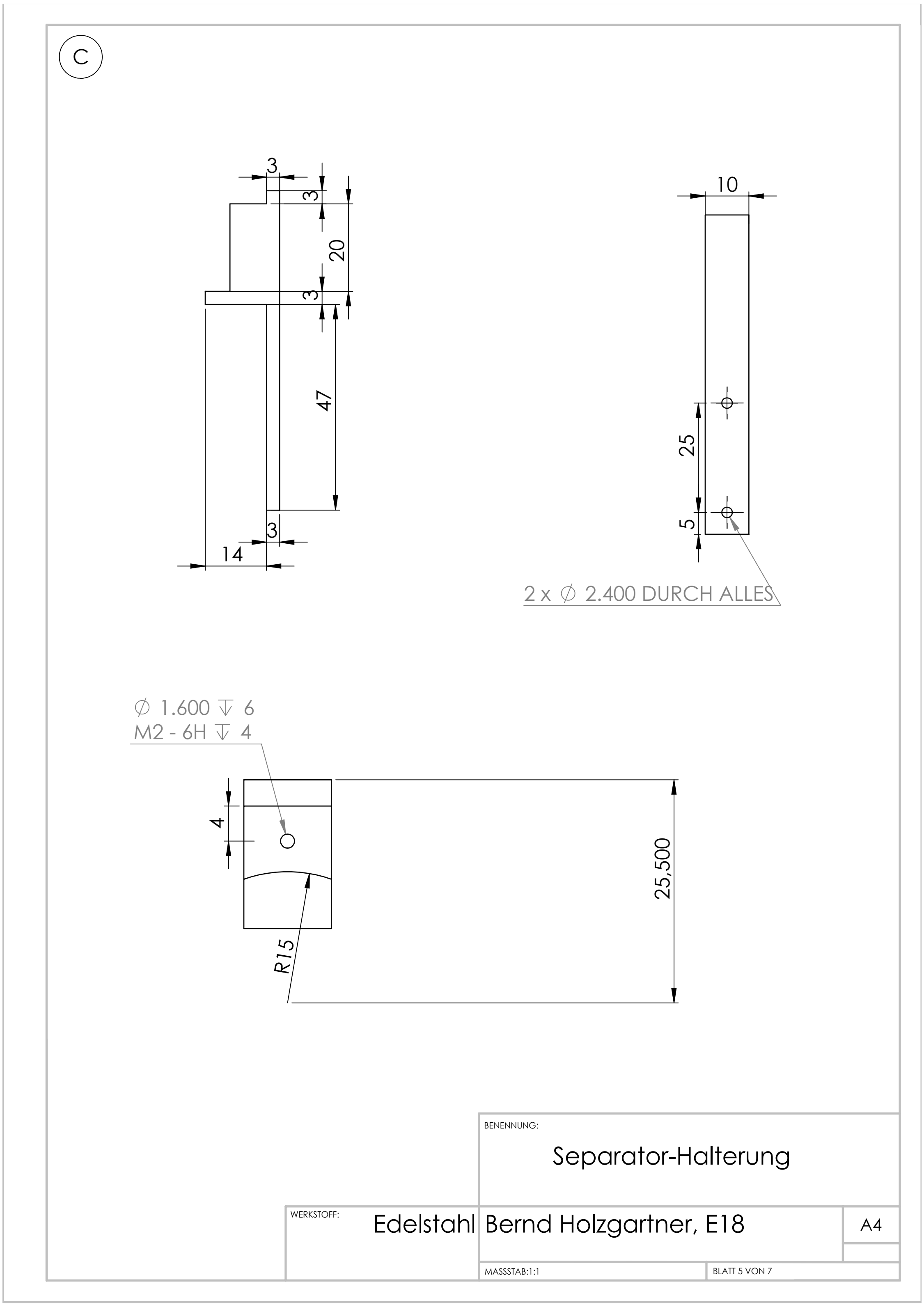
C
3
3
20
3
47
3
14
10
25
5
2 x ∅ 2.400 DURCH ALLES
∅ 1.600 ↧ 6
M2 - 6H ↧ 4
4
25,500
R15
BENENNUNG:
Separator-Halterung
WERKSTOFF:
Edelstahl
Bernd Holzgartner, E18
A4
MASSSTAB:1:1
BLATT 5 VON 7

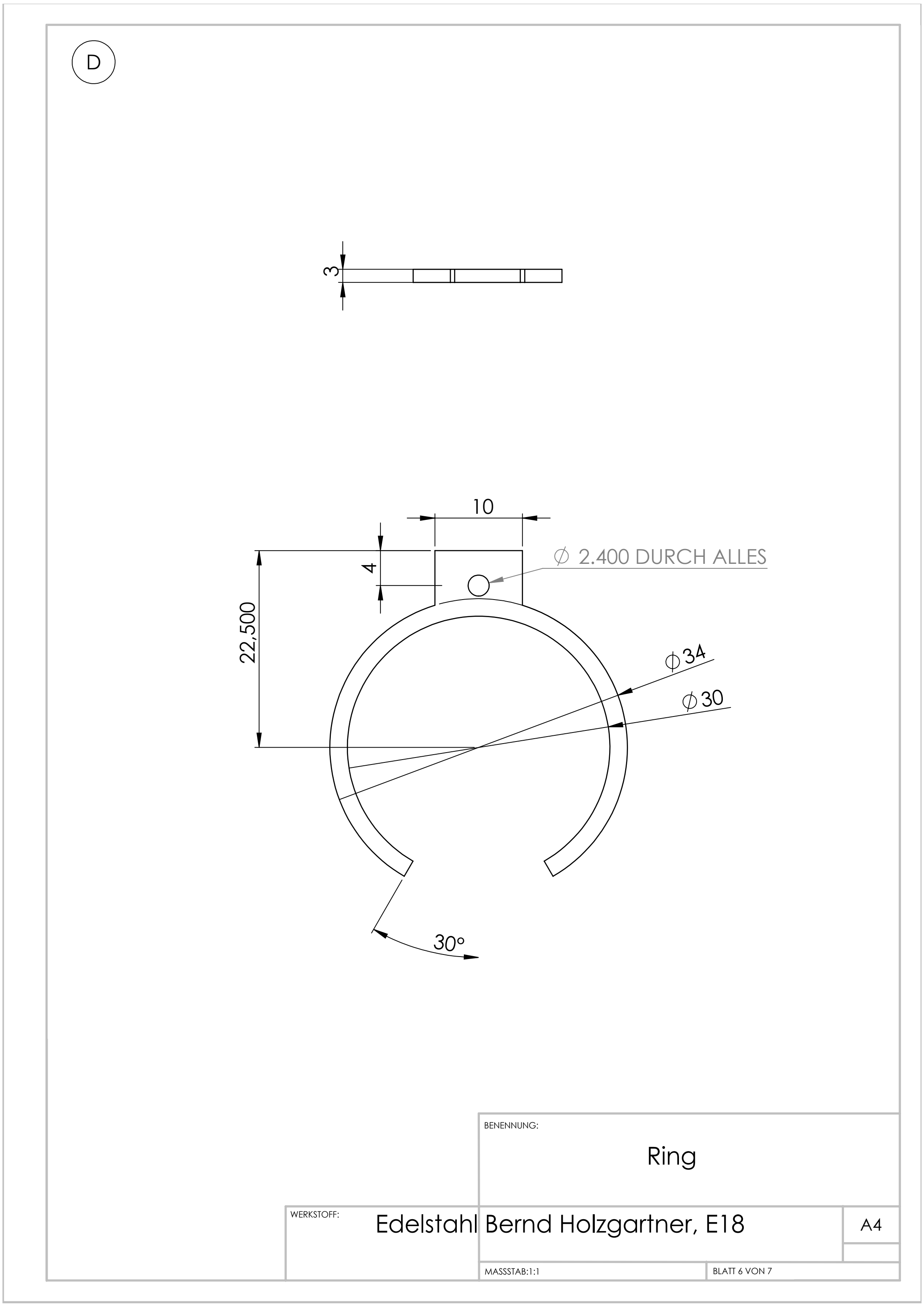
D
3
10
4
22,500
∅ 2.400 DURCH ALLES
∅34
∅30
30°
BENENNUNG:
Ring
WERKSTOFF:
Edelstahl
Bernd Holzgartner, E18
A4
MASSSTAB:1:1
BLATT 6 VON 7

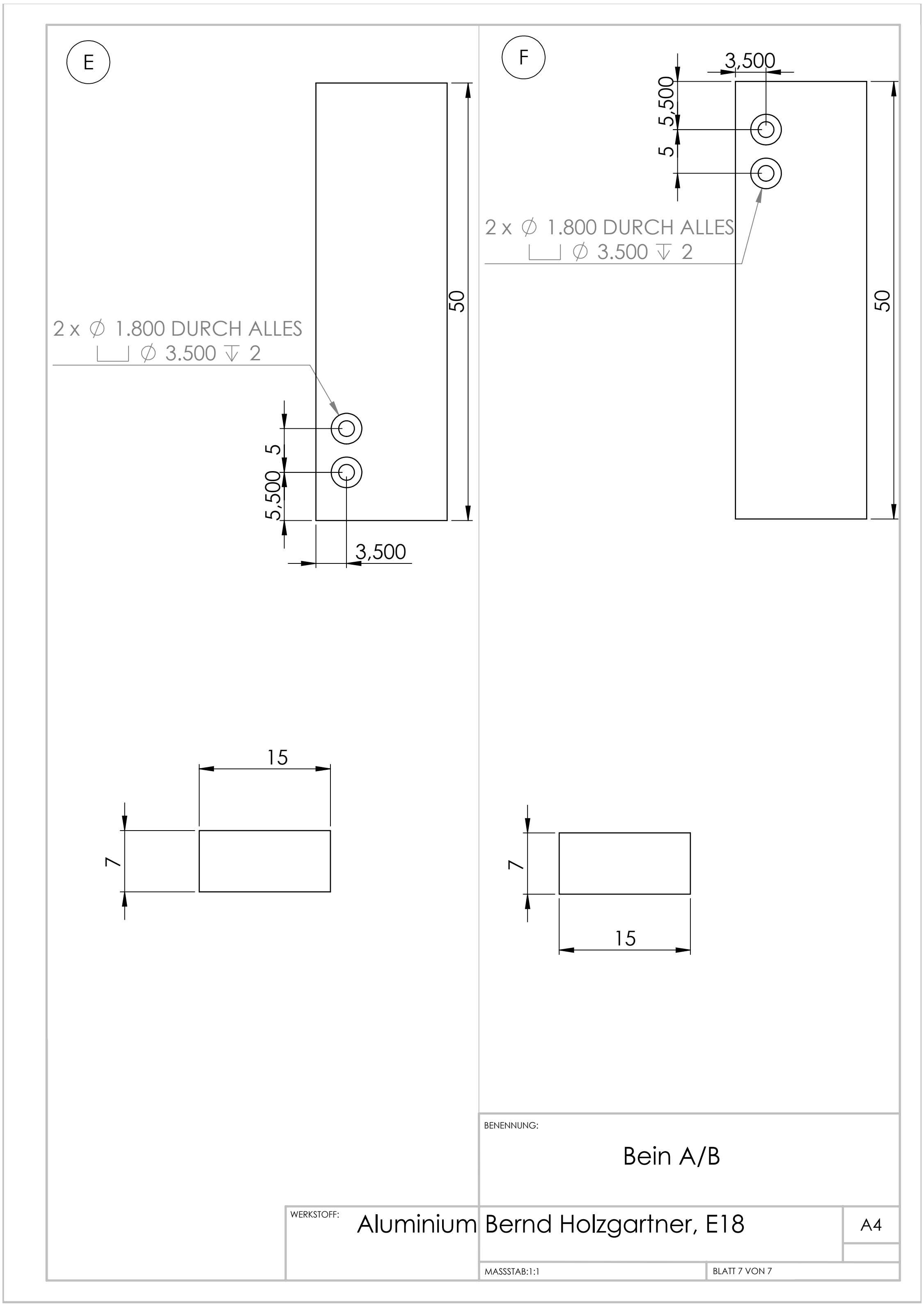
E
F
3,500
5,500
5
2 x ∅ 1.800 DURCH ALLES
⌴ ∅ 3.500 ↧ 2
50
50
2 x ∅ 1.800 DURCH ALLES
⌴ ∅ 3.500 ↧ 2
5
5,500
3,500
15
7
7
15
BENENNUNG:
Bein A/B
WERKSTOFF:
Aluminium
Bernd Holzgartner, E18
A4
MASSSTAB:1:1
BLATT 7 VON 7

B. Documentation of the water cooling system for the repeater cards

B.1. Mapping

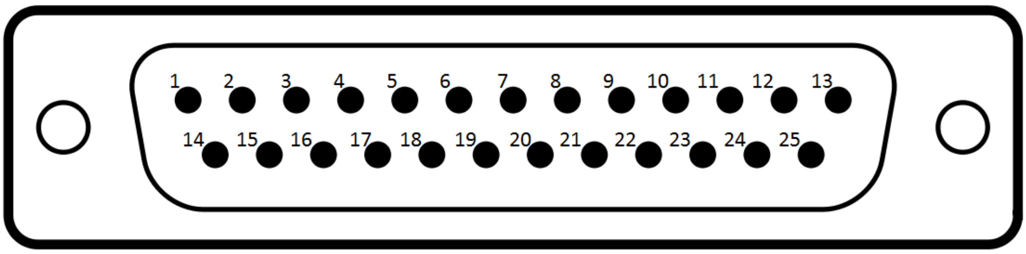

Figure B.1.: Pin numbering of the D-SUB DB-25M used throughout the whole water cooling system

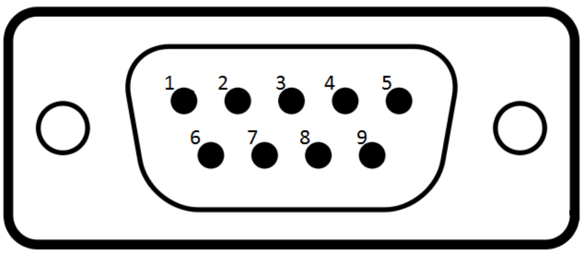

Figure B.2.: Pin numbering of the D-SUB DE-9M used throughout the whole water cooling system

Connector	Pin	Assignment
PLC	1-4	Temperature input (TE670) of the PLC for Saleve side
	5-8	Temperature input (TE671) of the PLC for Jura side
	9-12	NIL
	13-14	Digital input of the PLC for level sensor LS670A
	15-16	Digital input of the PLC for level sensor LS670B
	17-19	NIL
	20-21	Control voltage for relais controlling the magnet valve EV5670
	22-23	NIL
	24-25	Control voltage for relais controlling circulation pumps P670
UR	1	NIL
	2	+5V DC
	3	0V DC
	4	Digital output of level sensor LS670A
	5	NIL
	6	NIL
	7	+5V DC
	8	0V DC
	9	Digital output of level sensor LS670B
MV	1	+24V DC
	2-8	NIL
	9	0V DC
TE	1	GND
	2-5	Temperature input (TE670) of the PLC for Saleve side
	6-9	Temperature input (TE671) of the PLC for Jura Side

Table B.1.: Pin assignment of the D-SUB connectors used in the electronic box

Pin	Assignment
1	NIL
2	V_{CC} input of level sensor LS670A
3	0V input of level sensor LS670A
4	Digital output of level sensor LS670A
5	NIL
6	NIL
7	V_{CC} input of level sensor LS670B
8	0V input of level sensor LS670B
9	Digital output of level sensor LS670B

Table B.2.: Pin assignment of the D-SUB DE-9M used in the upper Reservoir

Pin	**Assignment**
1	+24V DC input of the magnet valve
2-8	NIL
9	0V DC input of the magnet valve

Table B.3.: Pin assignment of the D-SUB DE-9M used for the magnet valve

B.2. Components

B.2.1. Upper reservoir

Component	Supplier	Order number
Honeywell LLE 101000 level sensor	RS-Online	181-1328
Connector 1/2" to 10/8mm	Caseking	WASC-039
O-Ring NORMATEC NBR 70 Shore A	Angst & Pfister	11.2003.5918
D-SUB Connector, 9 pins	CONRAD	742066 - 05
Tamiya Color Lexanspray PS5	CONRAD	243841 - 05
Plexiglas[96]-components	TUM workshop	—

Table B.4.: Components of the upper reservoir

B.2.2. Electronic box

Component	Supplier	Order number
Rubber connector (female)	CONRAD	612600 - 62
TDK-Lambda DSP10-5 power supply	CONRAD	511513 - 05
TDK-Lambda DSP30-24 power supply	CONRAD	510901 - 62
Auto-Off-On Relay Finder Serie 19	CONRAD	503138 - 62
Rittal mounting rail	CONRAD	521016 - 62
Circuit board	CONRAD	527453 - 62
D-SUB Connector, 9 pins	CONRAD	742066 - 05
D-SUB Connector, 25 pins	CONRAD	741671 - 05
Solid state relais	Radiospares	3650620
4-conductor-bushing-clamp	Reichelt	WAGO 2002-1404
Baffle plate for bushing clamp	Reichelt	WAGO 2002-1492
Connection bridge 3x for bushing clamp	Reichelt	WAGO 2002-403
Connection bridge 2x for bushing clamp	Reichelt	WAGO 2002-402
Schuko socket	Reichelt	EL SKSD H
Plexiglas-components	TUM workshop	—

Table B.5.: Components of the electronic box

[96]Plexiglas is a registered trademark of Evonik Industries AG

B.2.3. Cooling plates

Component	Supplier	Order number
Copper pipe 1/8"	CS-Chromatographie	198004-01
Thermal conducting glue WLK 10[97]	CONRAD	181175 - 05
Copper plates	TUM workshop	—
Copper pad	TUM workshop	—

Table B.6.: Components of the cooling plates

B.2.4. Miscellaneous

Component	Supplier	Order number
Eheim 1262 pump	aquaristikshop.com	—
Connector 1/4" to 10/8mm	Caseking	WASC-002
10/8 mm PVC tube	Caseking	WAZU-036
Connector 1/2" to 10/8mm	Caseking	WASC-039
innovatek Protect IP anticorrosive	Caseking	WAZU-034
Ball valve	Caseking	WAAN-022
2/2 magnet valve	RS-Online	701-3249
D-SUB Connector, 9 pins	CONRAD	742066 - 05
Vacuum pump	Mercateo	768-9852902
Reducing socket 3/4" to 1/2"	schlauch-profi.de	45035019013
Connector 10/8mm to 1/4"	Swagelok	B-10M0-6-4
Connector 1/4" to 1/8"	Swagelok	B-400-6-2
Tubular stiffener 10/8mm	Swagelok	B-10M5-8M
Tubular stiffener 1/4"	Swagelok	B-405-2
Connector 10/8mm to 6mm	Swagelok	SS-10M0-6-6M
Tubular stiffener 10/8mm	Swagelok	SS-10M5-8M
1/4" PVC tube	Swagelok	LT-2-4
Hailea HC 500 A chiller	TUM[95]	—
Connector to 1/4" for Hailea HC 500 A	TUM[95]	—

Table B.7.: Residual components of the water cooling system

[97] only used for short pipe version

B.3. Technical drawings

B.3.1. Upper reservoir

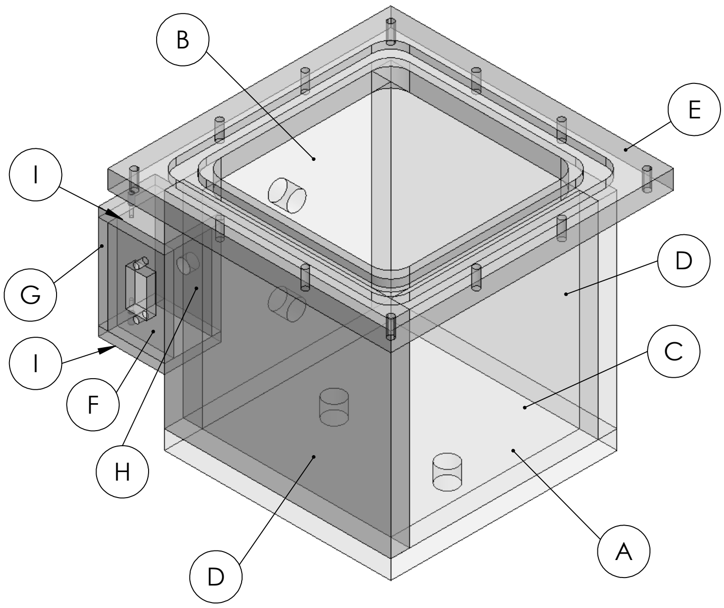

BENENNUNG: Reservoir, oben	
Bernd Holzgartner, E18	A4
MASSSTAB:1:2	BLATT 1 VON 12

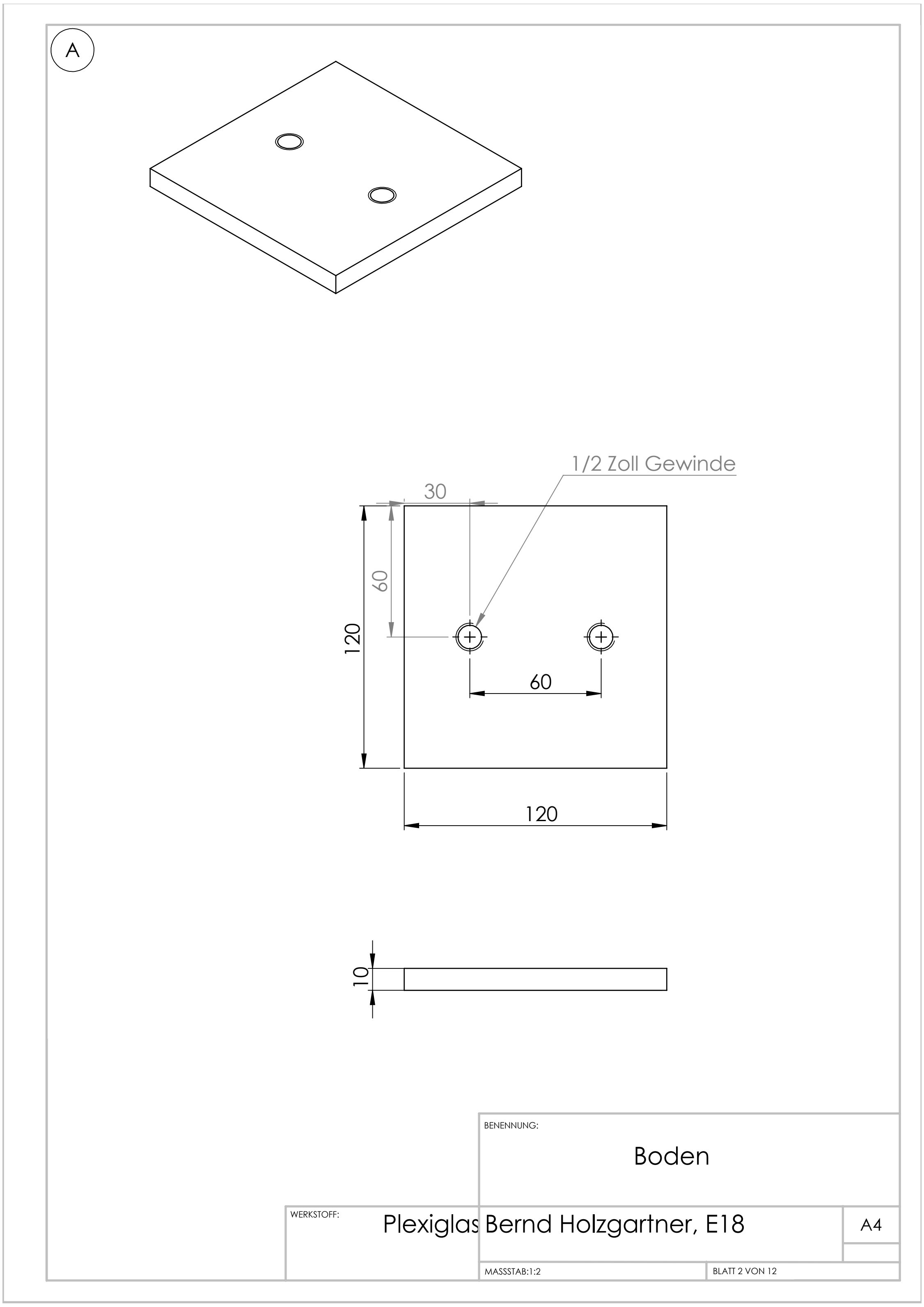
A
1/2 Zoll Gewinde
30
60
120
60
120
10
BENENNUNG:
Boden
WERKSTOFF:
Plexiglas
Bernd Holzgartner, E18
A4
MASSSTAB:1:2
BLATT 2 VON 12

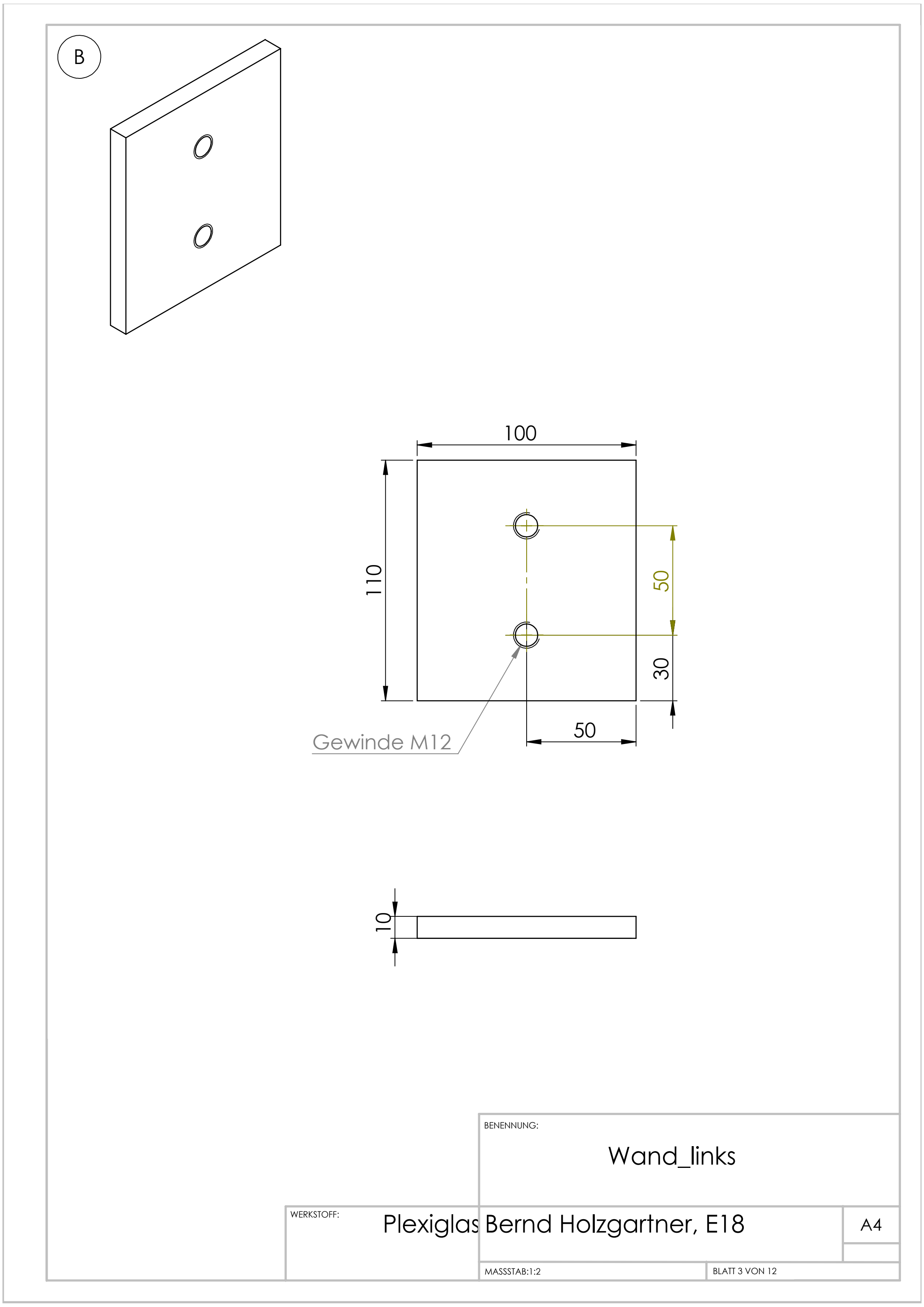
B
100
110
50
30
50
Gewinde M12
10
BENENNUNG:
Wand_links
WERKSTOFF:
Plexiglas
Bernd Holzgartner, E18
A4
MASSSTAB:1:2
BLATT 3 VON 12

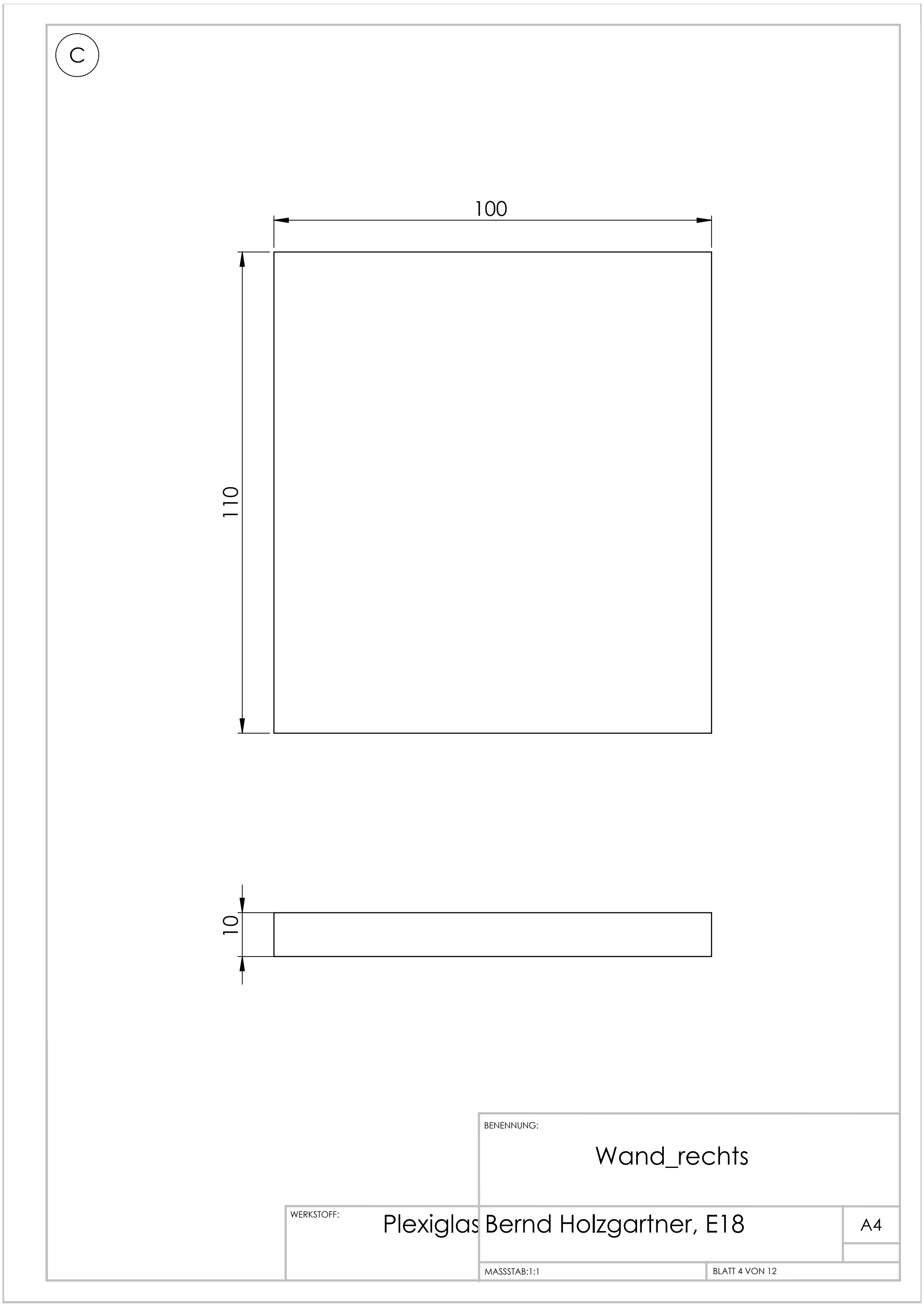
C
100
110
10
BENENNUNG:
Wand_rechts
WERKSTOFF:
Plexiglas
Bernd Holzgartner, E18
A4
MASSSTAB:1:1
BLATT 4 VON 12

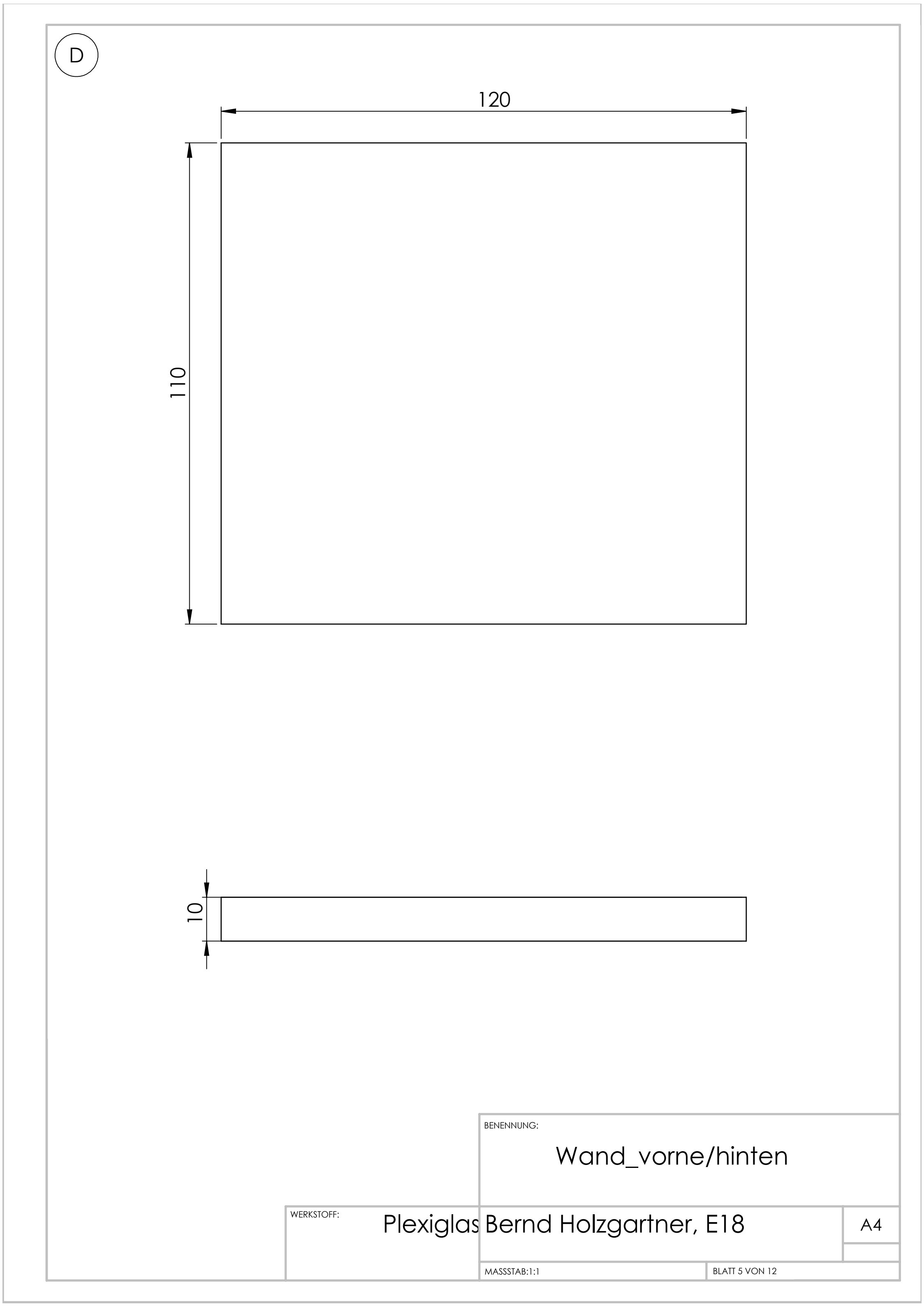
D
120
110
10
BENENNUNG:
Wand_vorne/hinten
WERKSTOFF:
Plexiglas
Bernd Holzgartner, E18
A4
MASSSTAB:1:1
BLATT 5 VON 12

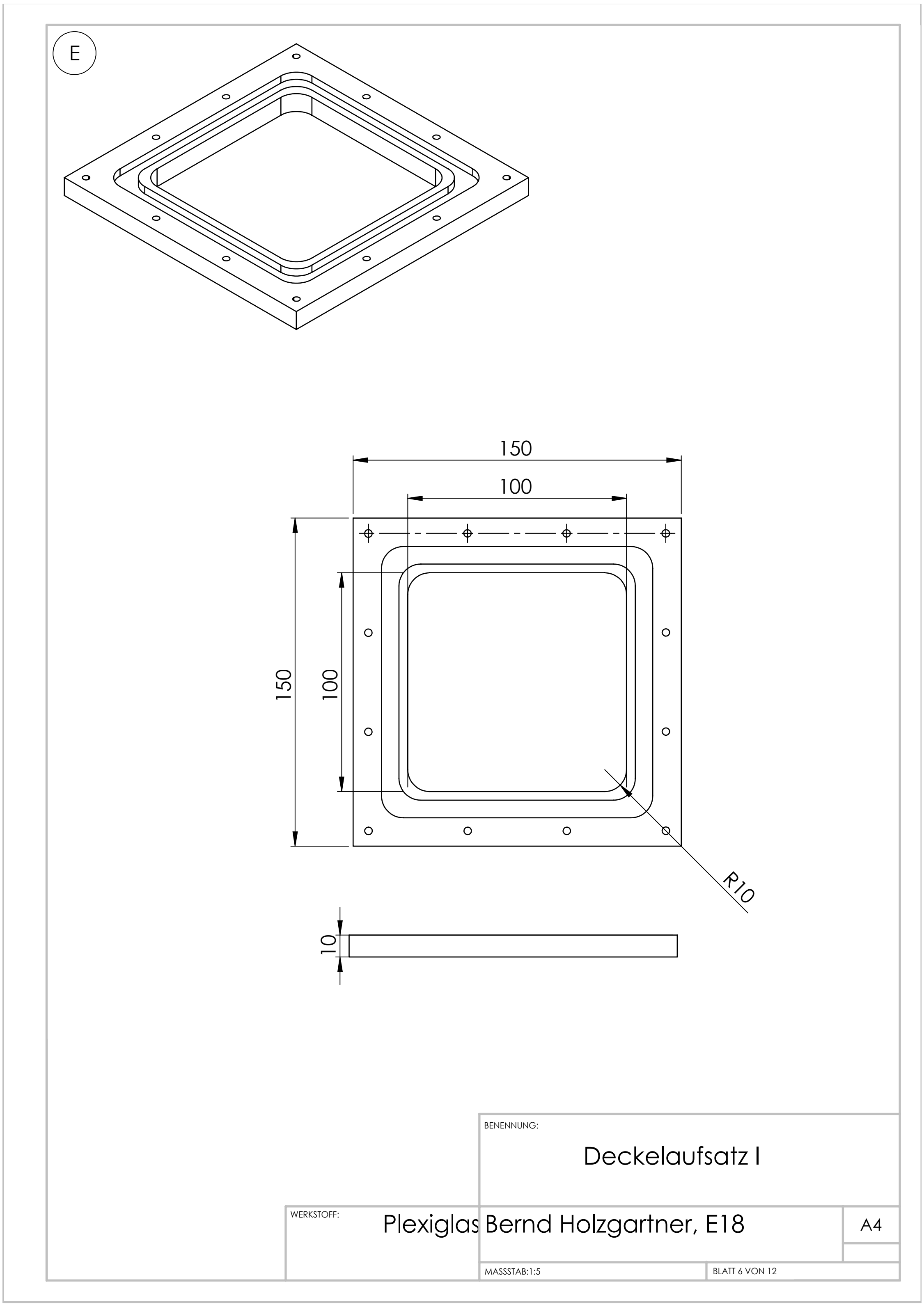
E
150
100
150
100
R10
10
BENENNUNG:
Deckelaufsatz I
WERKSTOFF:
Plexiglas
Bernd Holzgartner, E18
A4
MASSSTAB:1:5
BLATT 6 VON 12

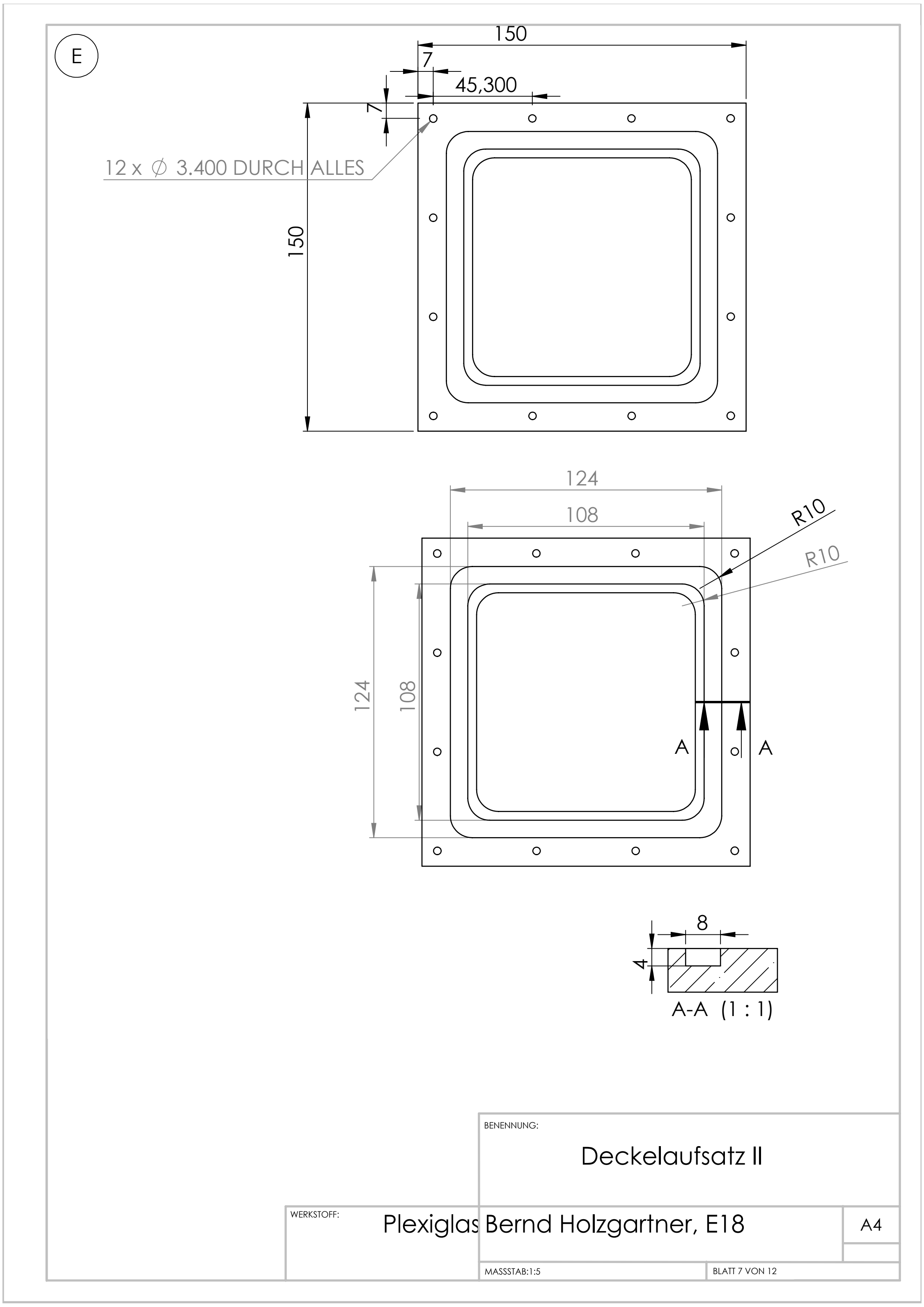
E
150
7
45,300
7
12 x ∅ 3.400 DURCH ALLES
150
124
108
R10
R10
124
108
A
A
8
4
A-A (1 : 1)
BENENNUNG:
Deckelaufsatz II
WERKSTOFF:
Plexiglas
Bernd Holzgartner, E18
A4
MASSSTAB:1:5
BLATT 7 VON 12

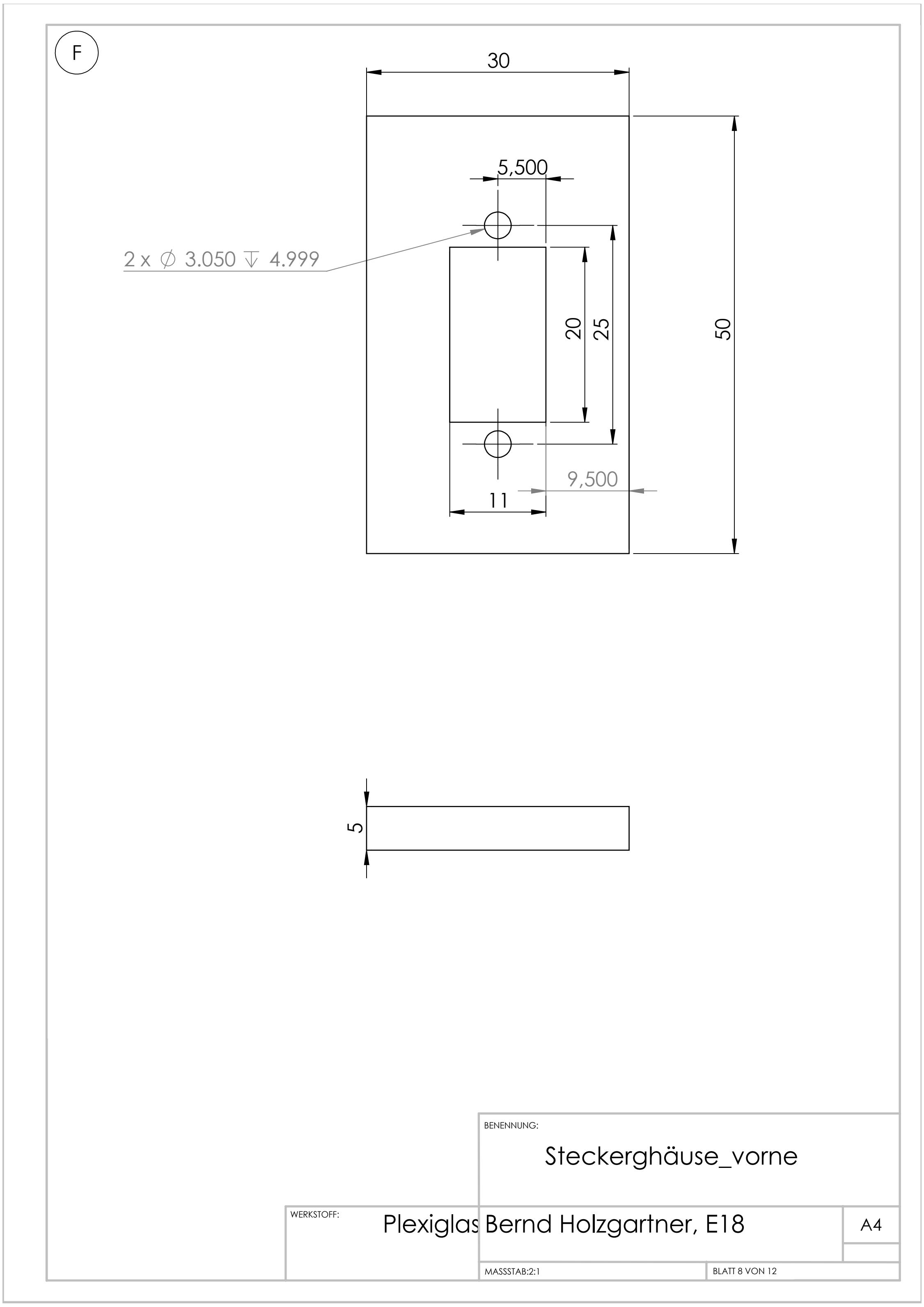
F
30
5,500
2 x ∅ 3.050 ↧ 4.999
20
25
50
9,500
11
5
BENENNUNG:
Steckerghäuse_vorne
WERKSTOFF:
Plexiglas
Bernd Holzgartner, E18
A4
MASSSTAB:2:1
BLATT 8 VON 12

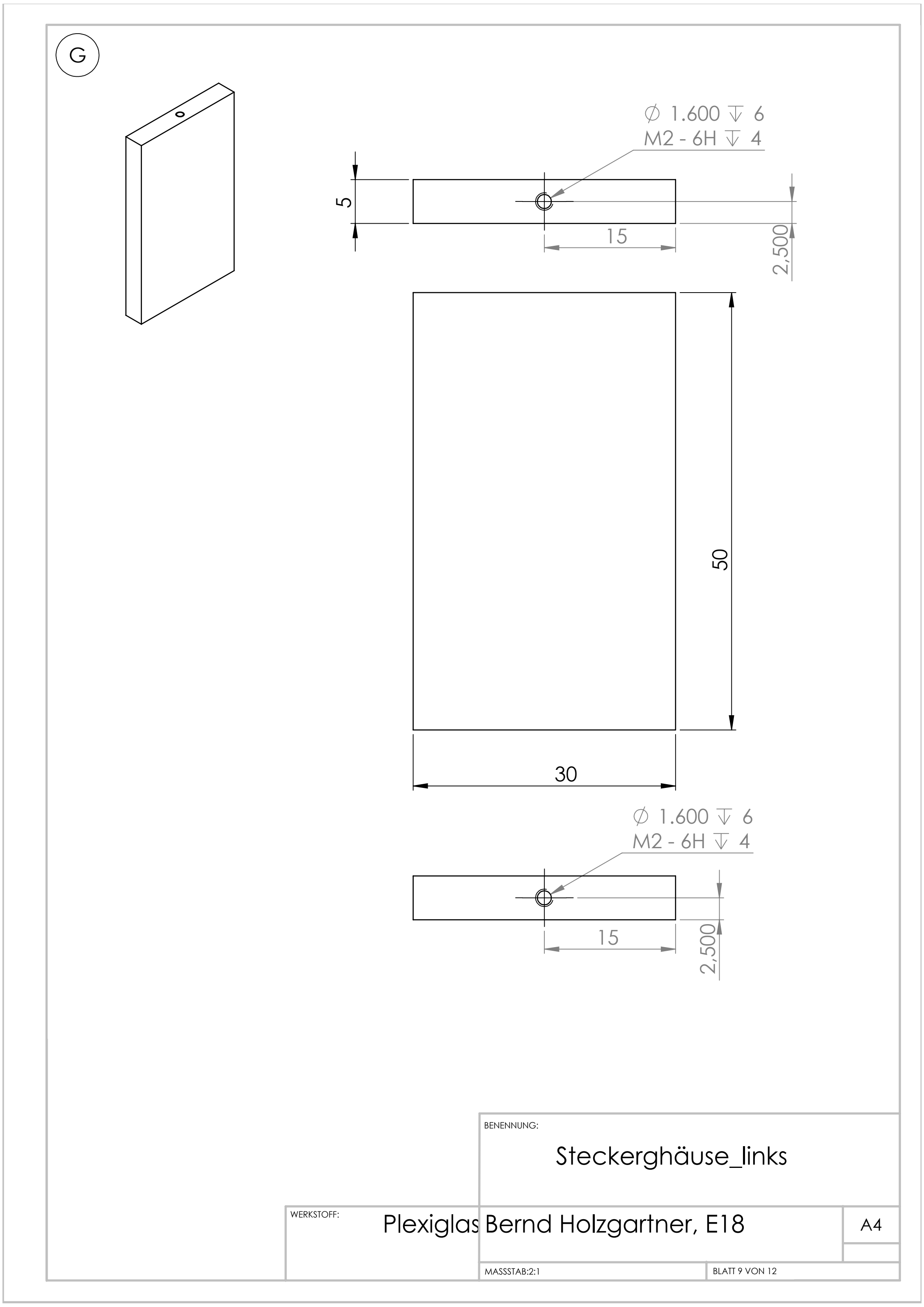
G
∅ 1.600 ↧ 6
M2 - 6H ↧ 4
5
15
2,500
50
30
∅ 1.600 ↧ 6
M2 - 6H ↧ 4
15
2,500
BENENNUNG:
Steckerghäuse_links
WERKSTOFF:
Plexiglas
Bernd Holzgartner, E18
A4
MASSSTAB:2:1
BLATT 9 VON 12

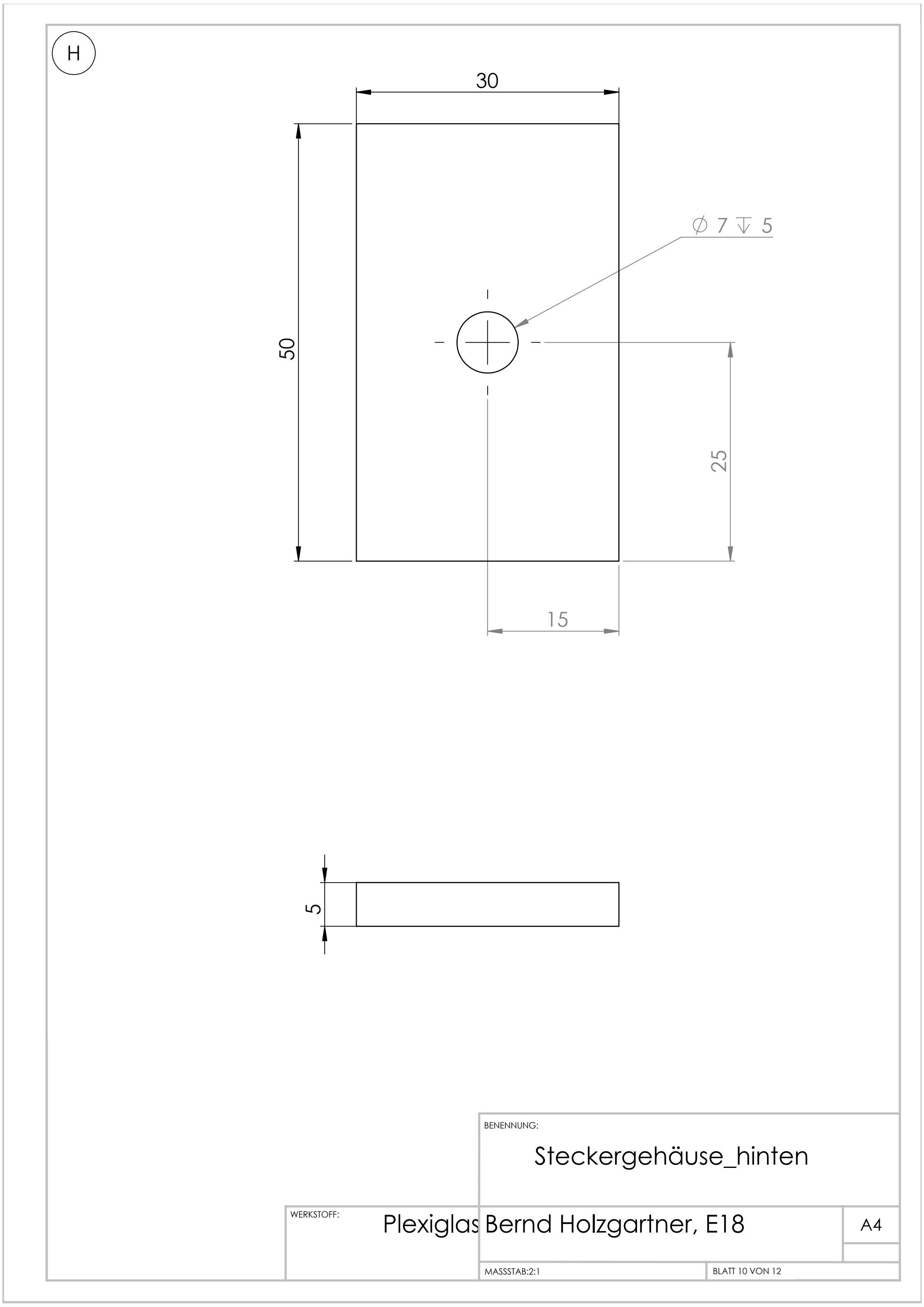
H
30
50
⌀ 7 ↧ 5
25
15
5
BENENNUNG:
Steckergehäuse_hinten
WERKSTOFF:
Plexiglas
Bernd Holzgartner, E18
A4
MASSSTAB:2:1
BLATT 10 VON 12

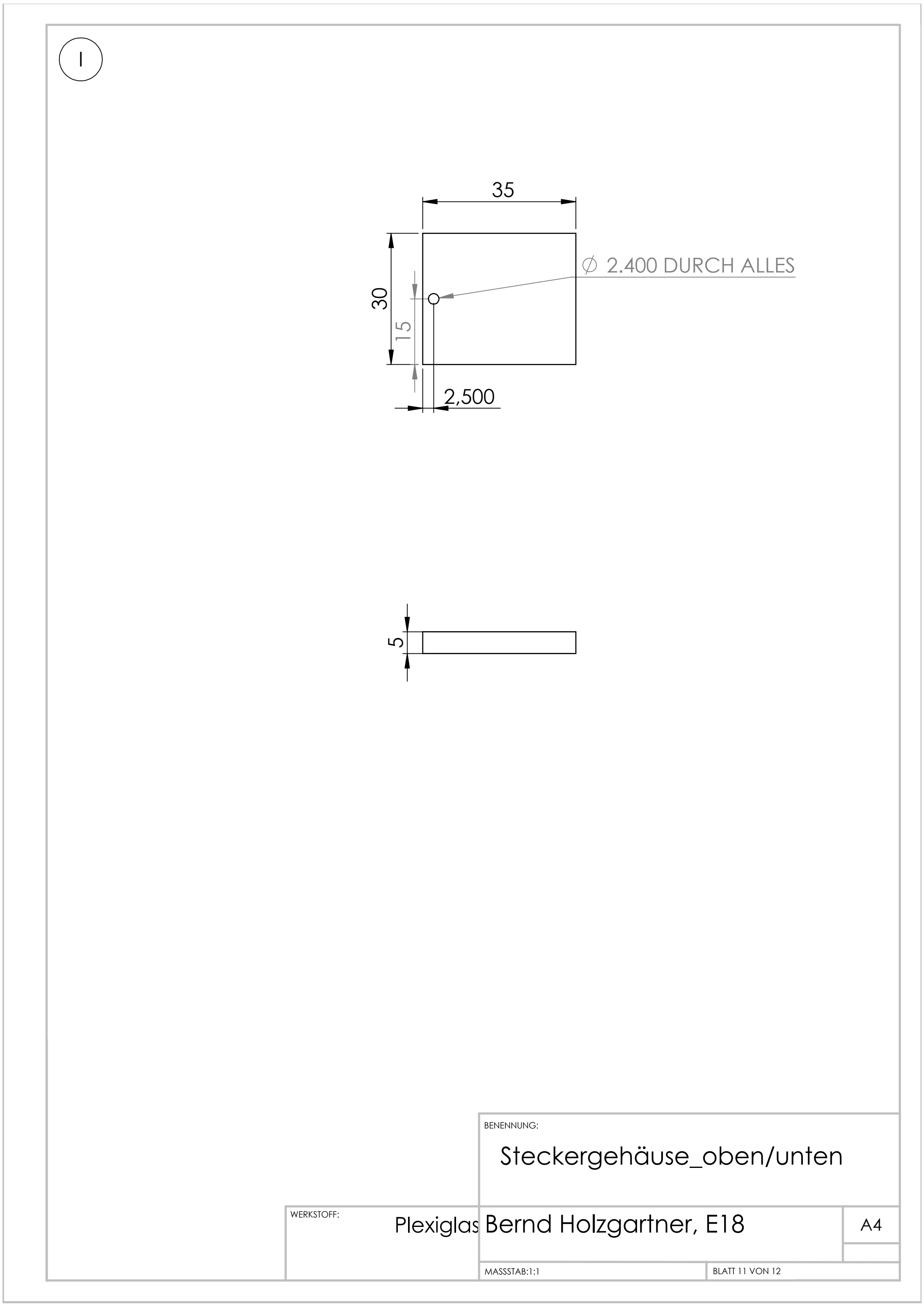
I
35
⌀ 2.400 DURCH ALLES
30
15
2,500
5
BENENNUNG:
Steckergehäuse_oben/unten
WERKSTOFF:
Plexiglas
Bernd Holzgartner, E18
A4
MASSSTAB:1:1
BLATT 11 VON 12

B.3.2. Cooling plates

Short pipe version

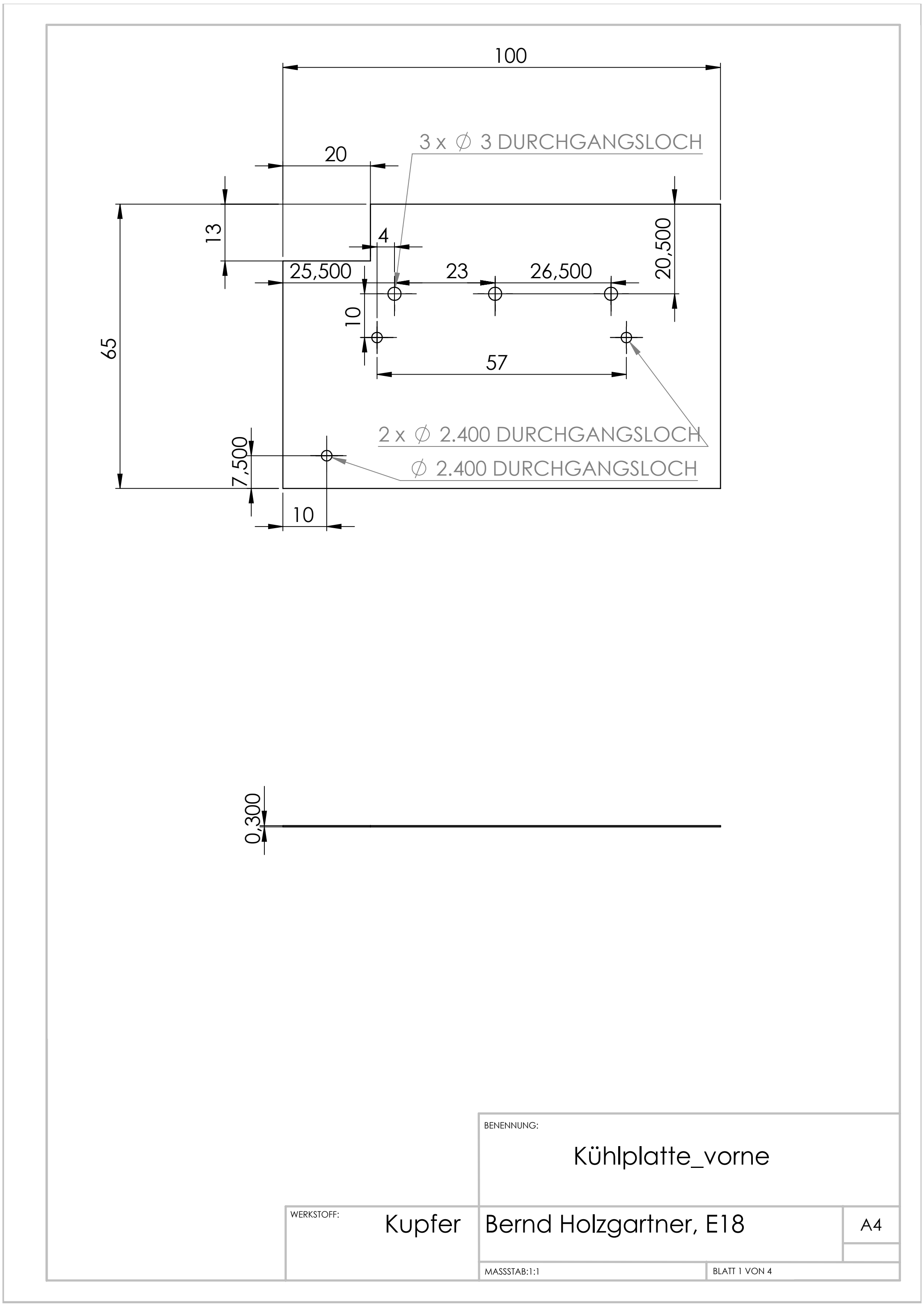
100
3 x ∅ 3 DURCHGANGSLOCH
20
13
4
20,500
25,500
23
26,500
10
65
57
2 x ∅ 2.400 DURCHGANGSLOCH
∅ 2.400 DURCHGANGSLOCH
7,500
10
0,300
BENENNUNG:
Kühlplatte_vorne
WERKSTOFF:
Kupfer
Bernd Holzgartner, E18
A4
MASSSTAB:1:1
BLATT 1 VON 4

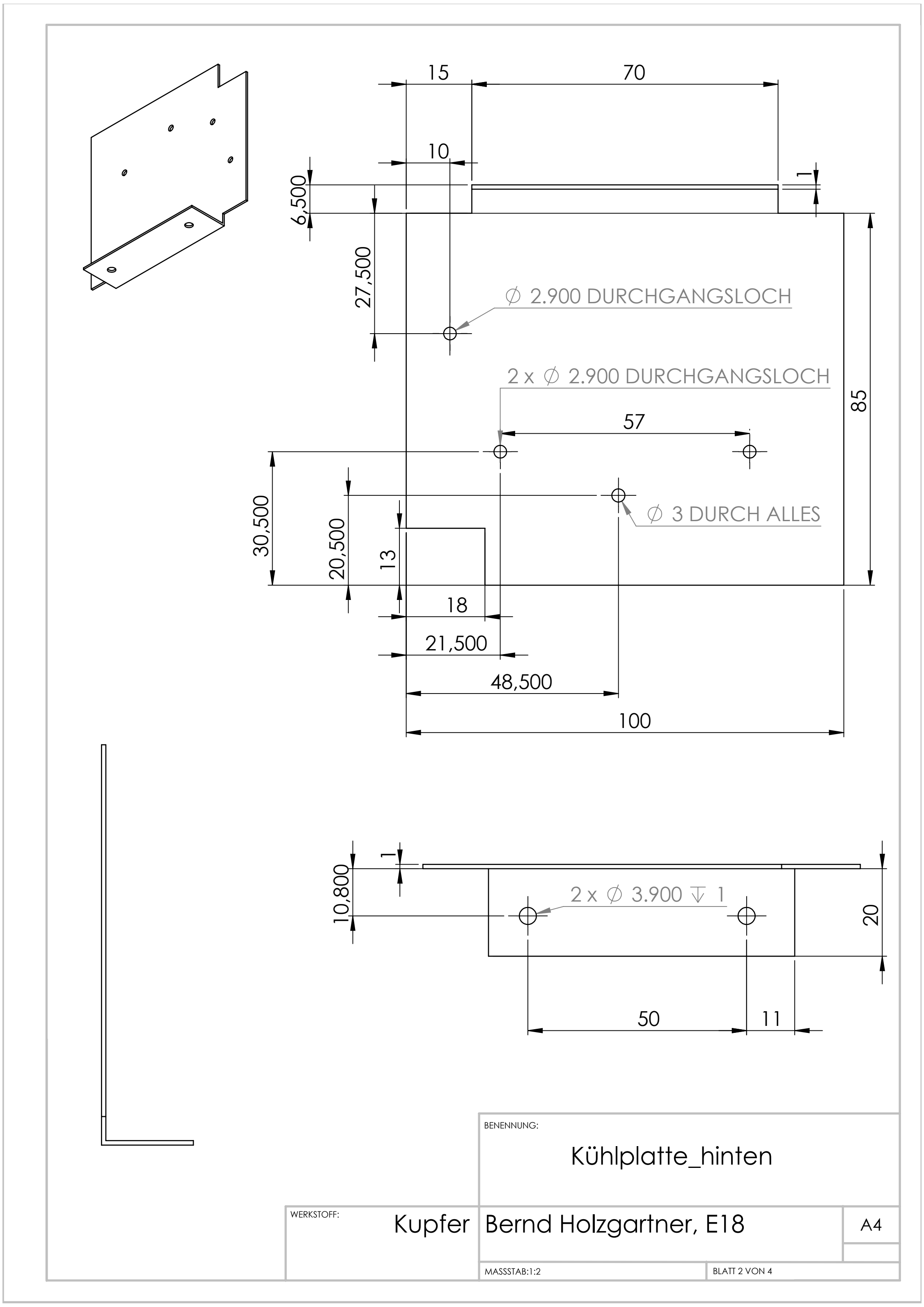
15
70
10
1
6,500
27,500
∅ 2.900 DURCHGANGSLOCH
2 x ∅ 2.900 DURCHGANGSLOCH
57
85
30,500
20,500
13
∅ 3 DURCH ALLES
18
21,500
48,500
100
1
10,800
2 x ∅ 3.900 ↧ 1
20
50
11
BENENNUNG:
Kühlplatte_hinten
WERKSTOFF:
Kupfer
Bernd Holzgartner, E18
A4
MASSSTAB:1:2
BLATT 2 VON 4

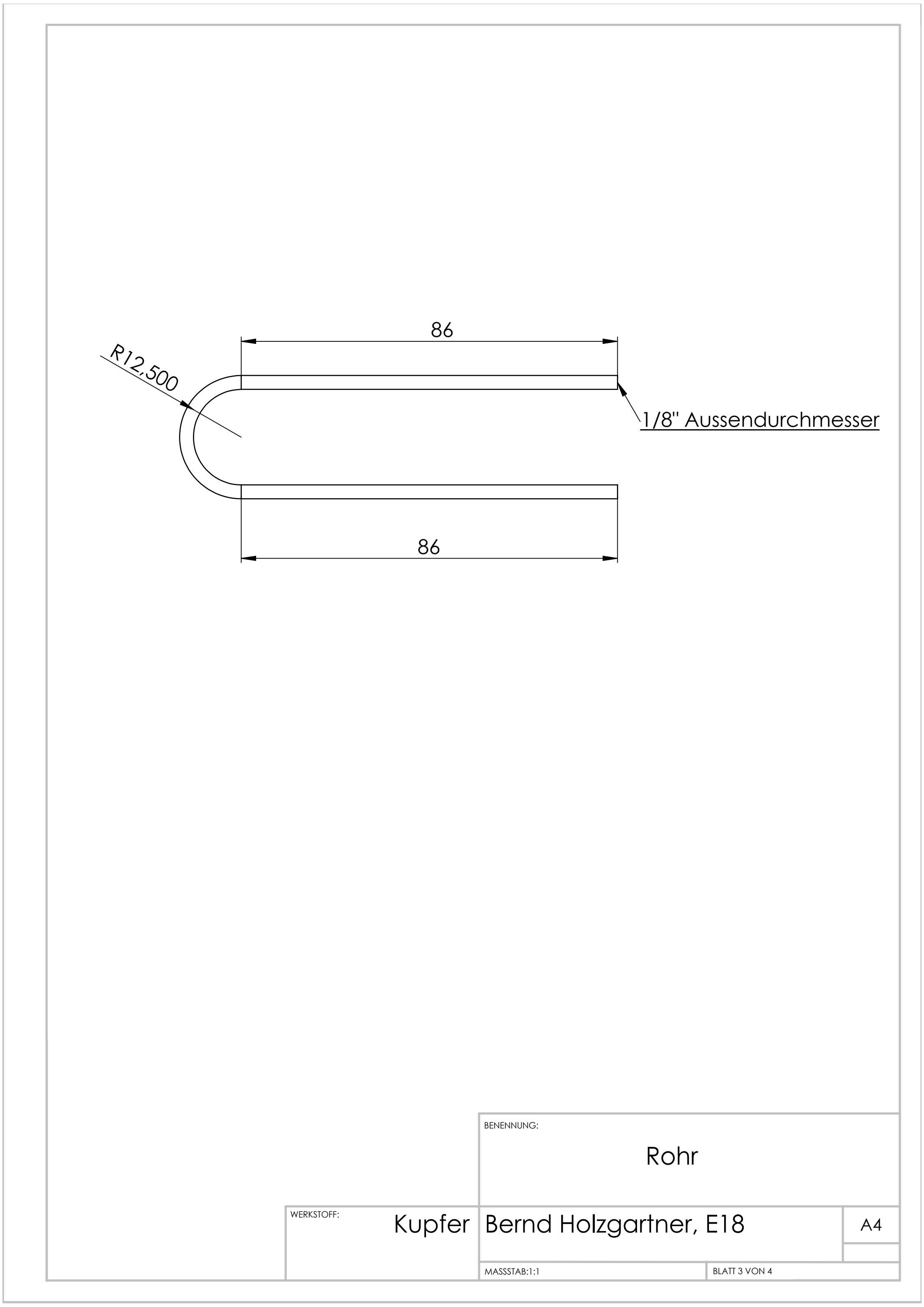
86
R12,500
1/8" Aussendurchmesser
86
BENENNUNG:
Rohr
WERKSTOFF:
Kupfer
Bernd Holzgartner, E18
A4
MASSSTAB:1:1
BLATT 3 VON 4

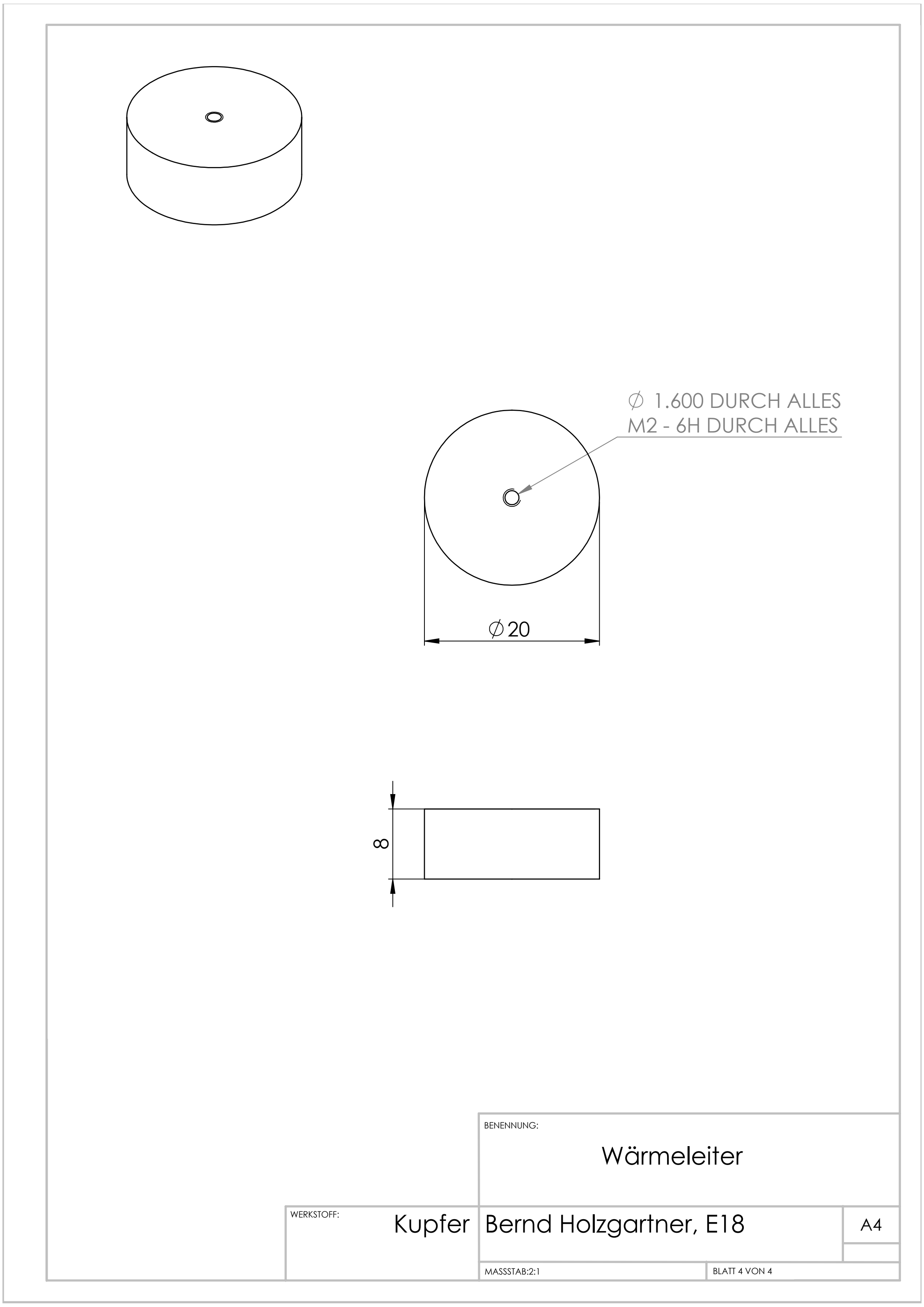
∅ 1.600 DURCH ALLES
M2 - 6H DURCH ALLES
∅20
8
BENENNUNG:
Wärmeleiter
WERKSTOFF:
Kupfer
Bernd Holzgartner, E18
A4
MASSSTAB:2:1
BLATT 4 VON 4

Long pipe version

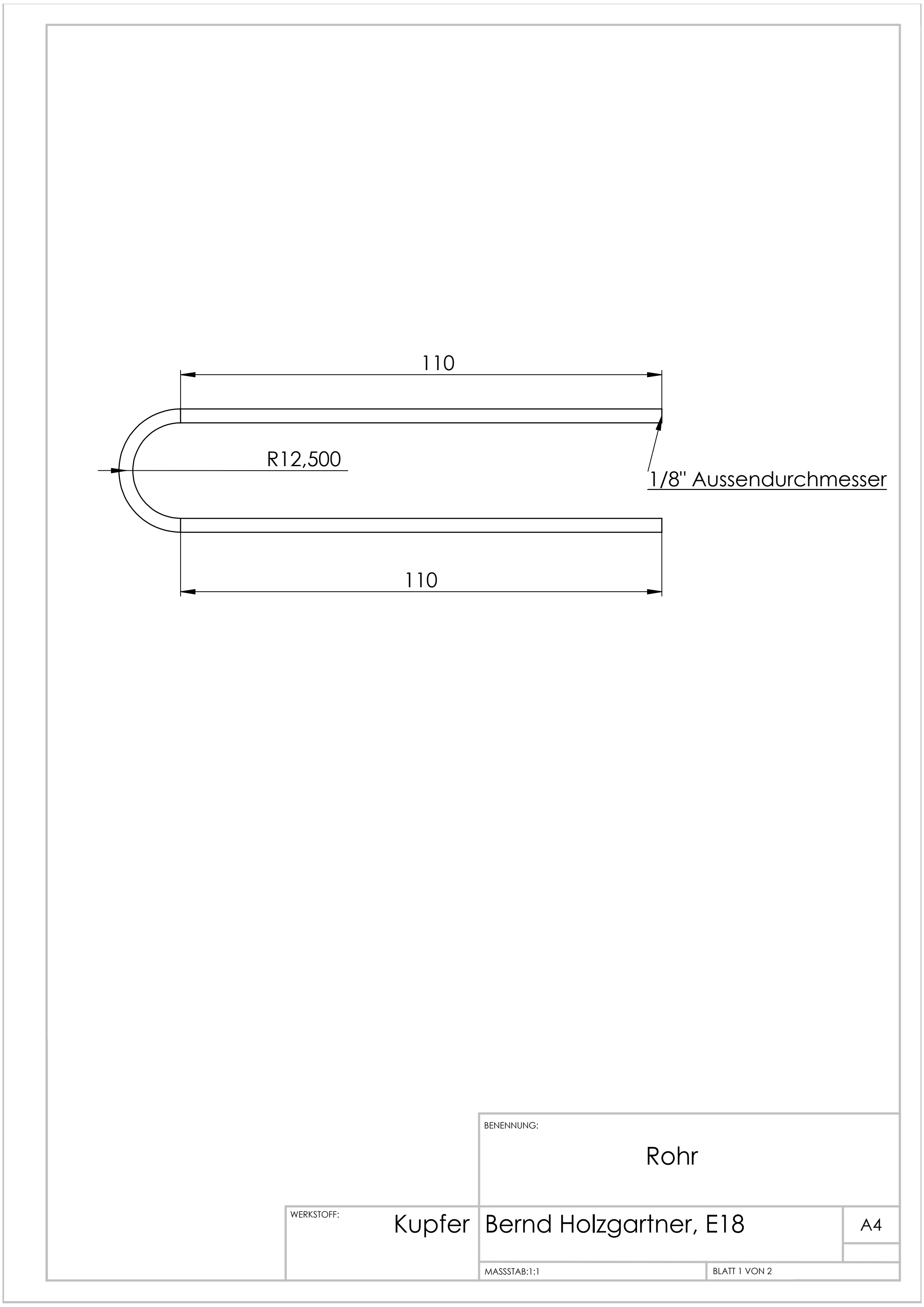
110
R12,500
1/8" Aussendurchmesser
110
BENENNUNG:
Rohr
WERKSTOFF:
Kupfer
Bernd Holzgartner, E18
A4
MASSSTAB:1:1
BLATT 1 VON 2

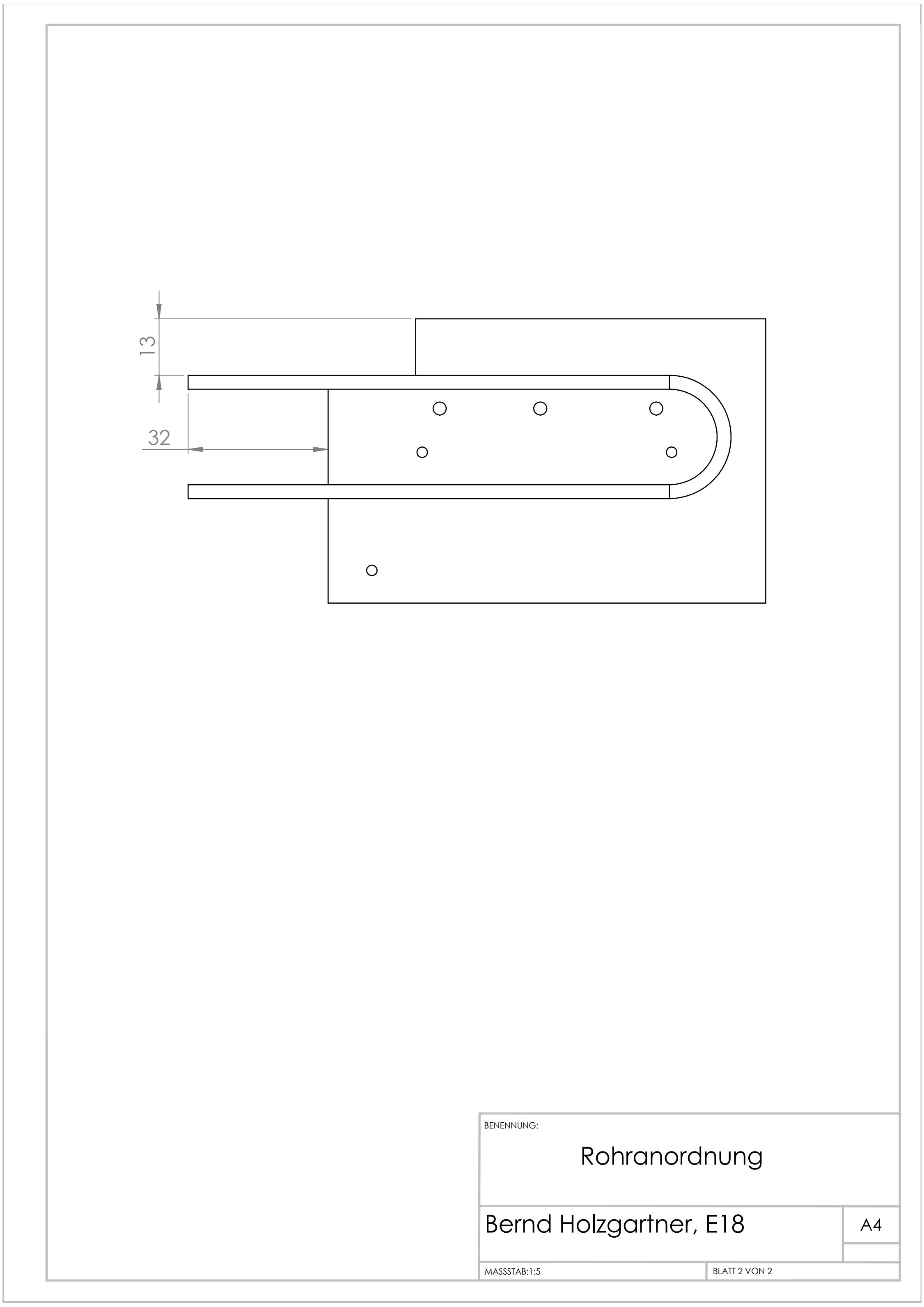
13
32
BENENNUNG:
Rohranordnung
Bernd Holzgartner, E18
A4
MASSSTAB:1:5
BLATT 2 VON 2

B.3.3. Electronic box

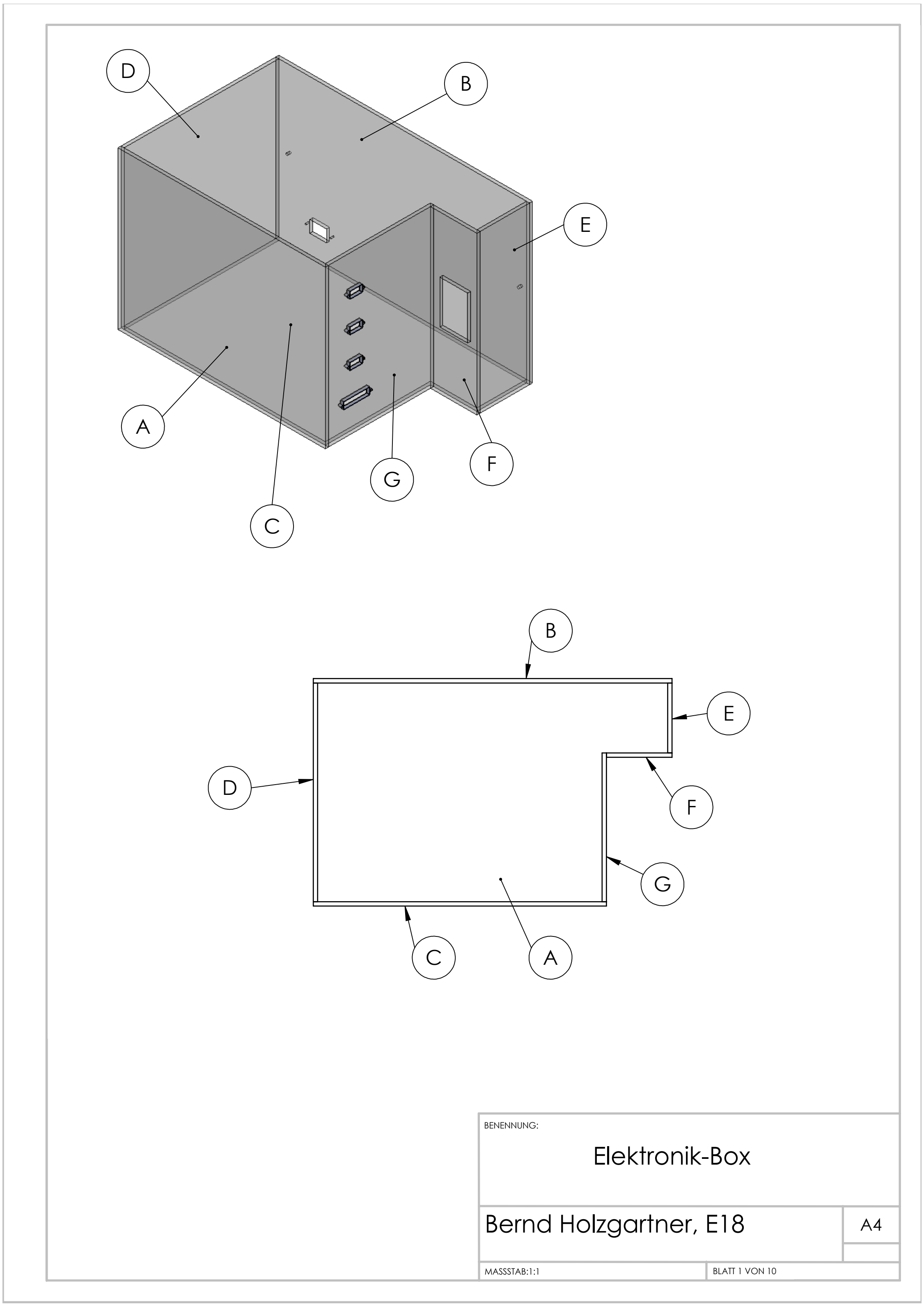
D
B
E
A
G
F
C
B
E
D
F
G
C
A
BENENNUNG:
Elektronik-Box
Bernd Holzgartner, E18
A4
MASSSTAB:1:1
BLATT 1 VON 10

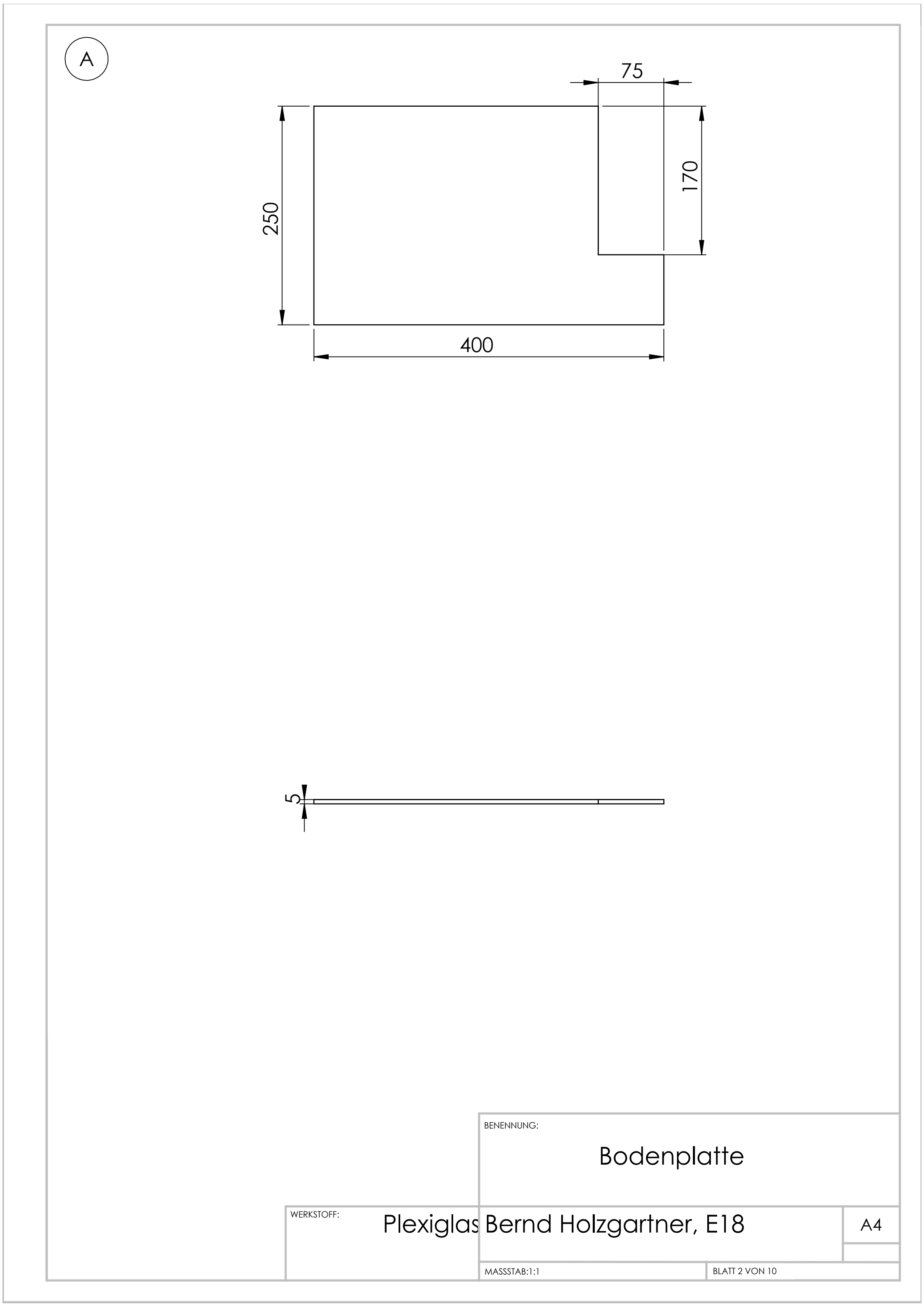
A
75
170
250
400
5
BENENNUNG:
Bodenplatte
WERKSTOFF:
Plexiglas
Bernd Holzgartner, E18
A4
MASSSTAB:1:1
BLATT 2 VON 10

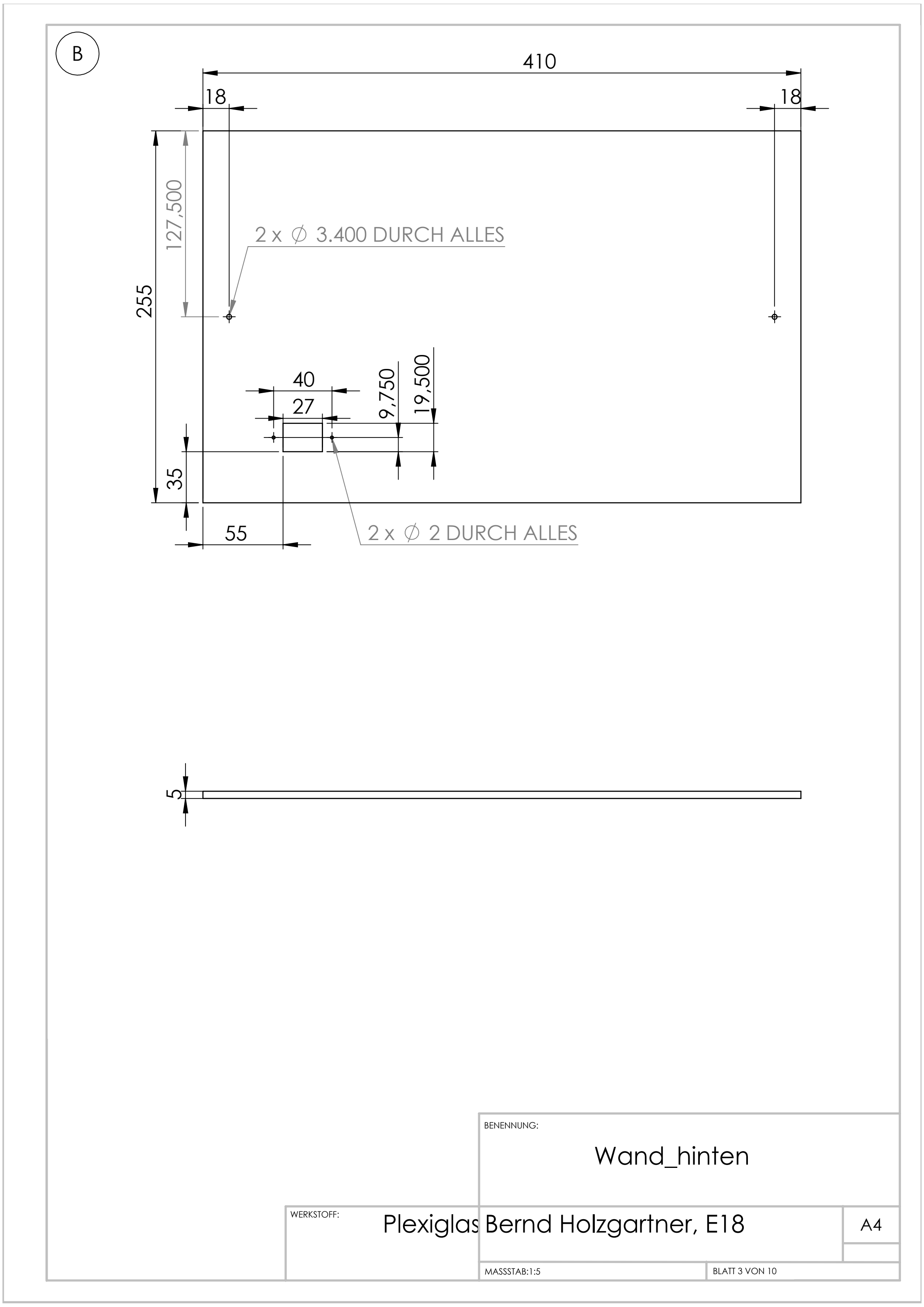
B
410
18
18
127,500
2 x ∅ 3.400 DURCH ALLES
255
40
27
9,750
19,500
35
55
2 x ∅ 2 DURCH ALLES
5
BENENNUNG:
Wand_hinten
WERKSTOFF:
Plexiglas
Bernd Holzgartner, E18
A4
MASSSTAB:1:5
BLATT 3 VON 10

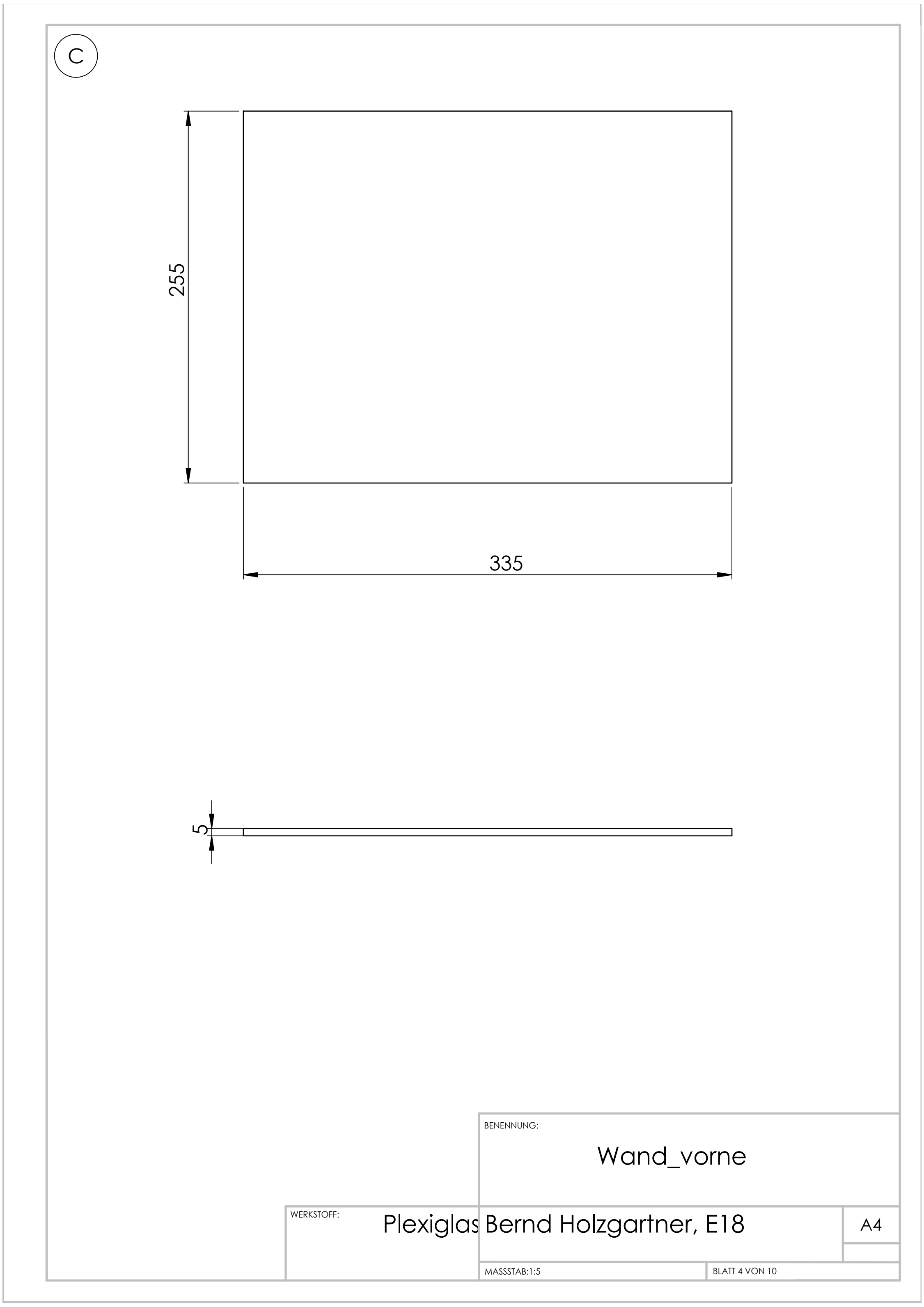
C
255
335
5
BENENNUNG:
Wand_vorne
WERKSTOFF:
Plexiglas
Bernd Holzgartner, E18
A4
MASSSTAB:1:5
BLATT 4 VON 10

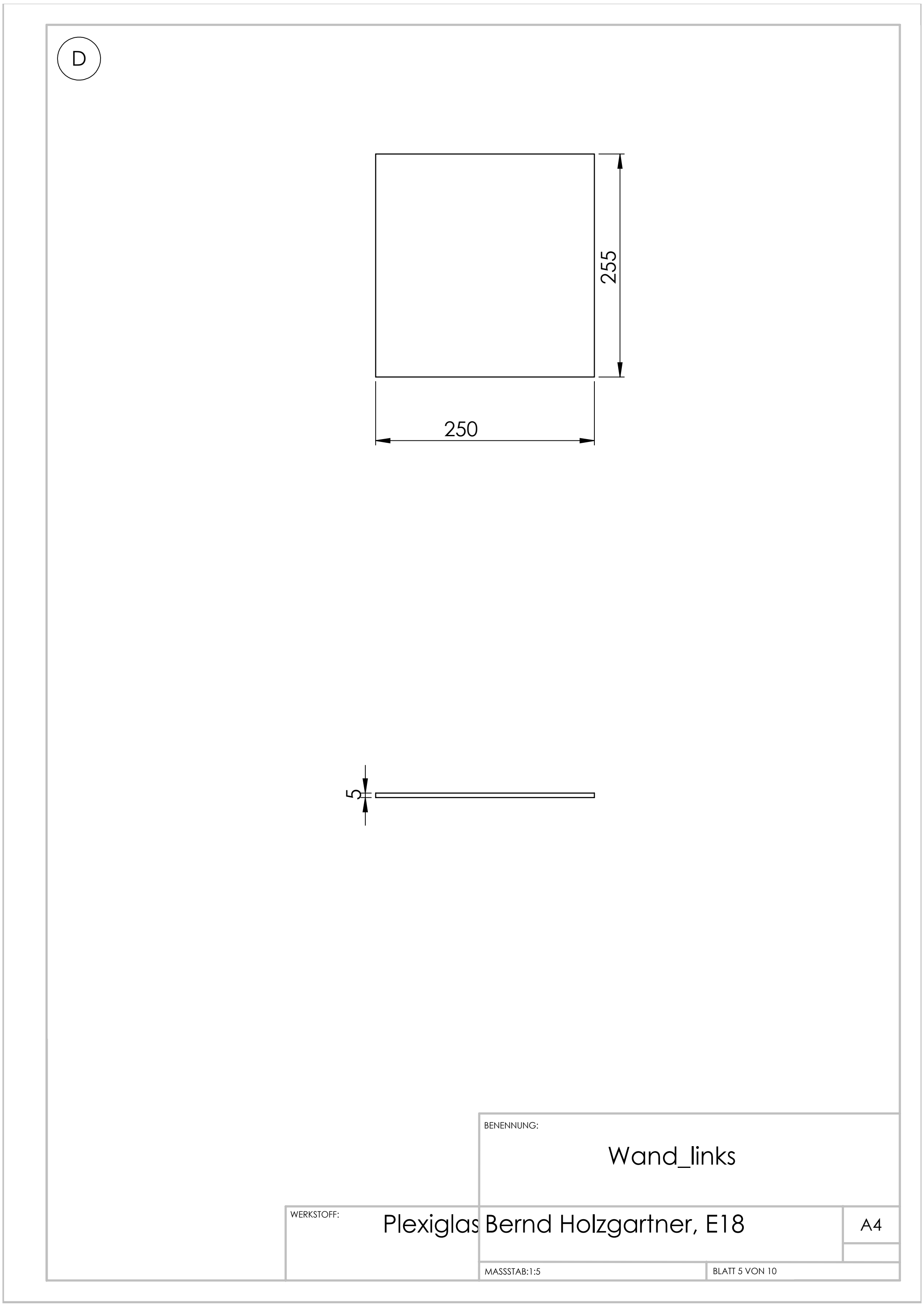
D
255
250
5
BENENNUNG:
Wand_links
WERKSTOFF:
Plexiglas
Bernd Holzgartner, E18
A4
MASSSTAB:1:5
BLATT 5 VON 10

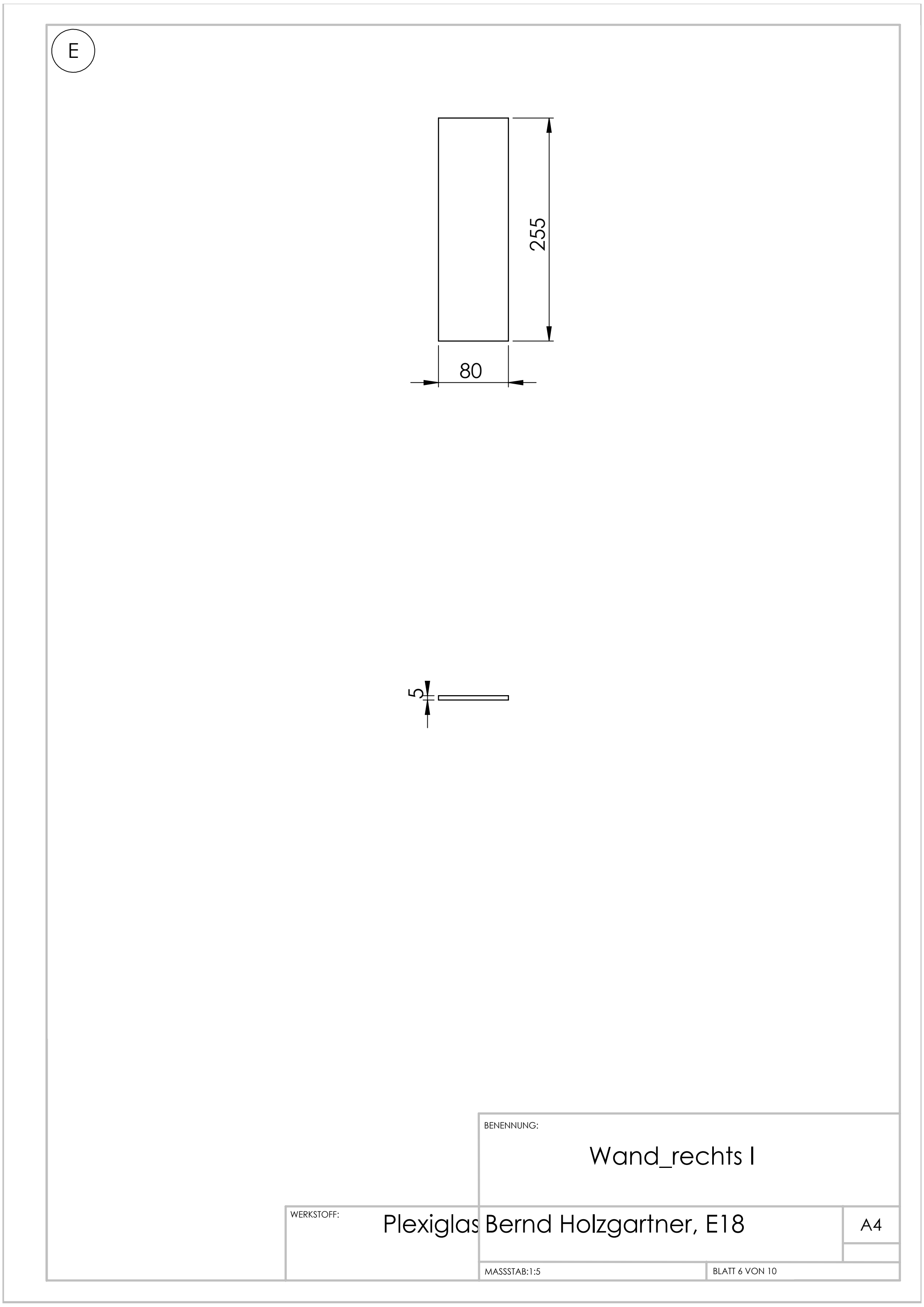
E
255
80
5
BENENNUNG:
Wand_rechts I
WERKSTOFF:
Plexiglas
Bernd Holzgartner, E18
A4
MASSSTAB:1:5
BLATT 6 VON 10

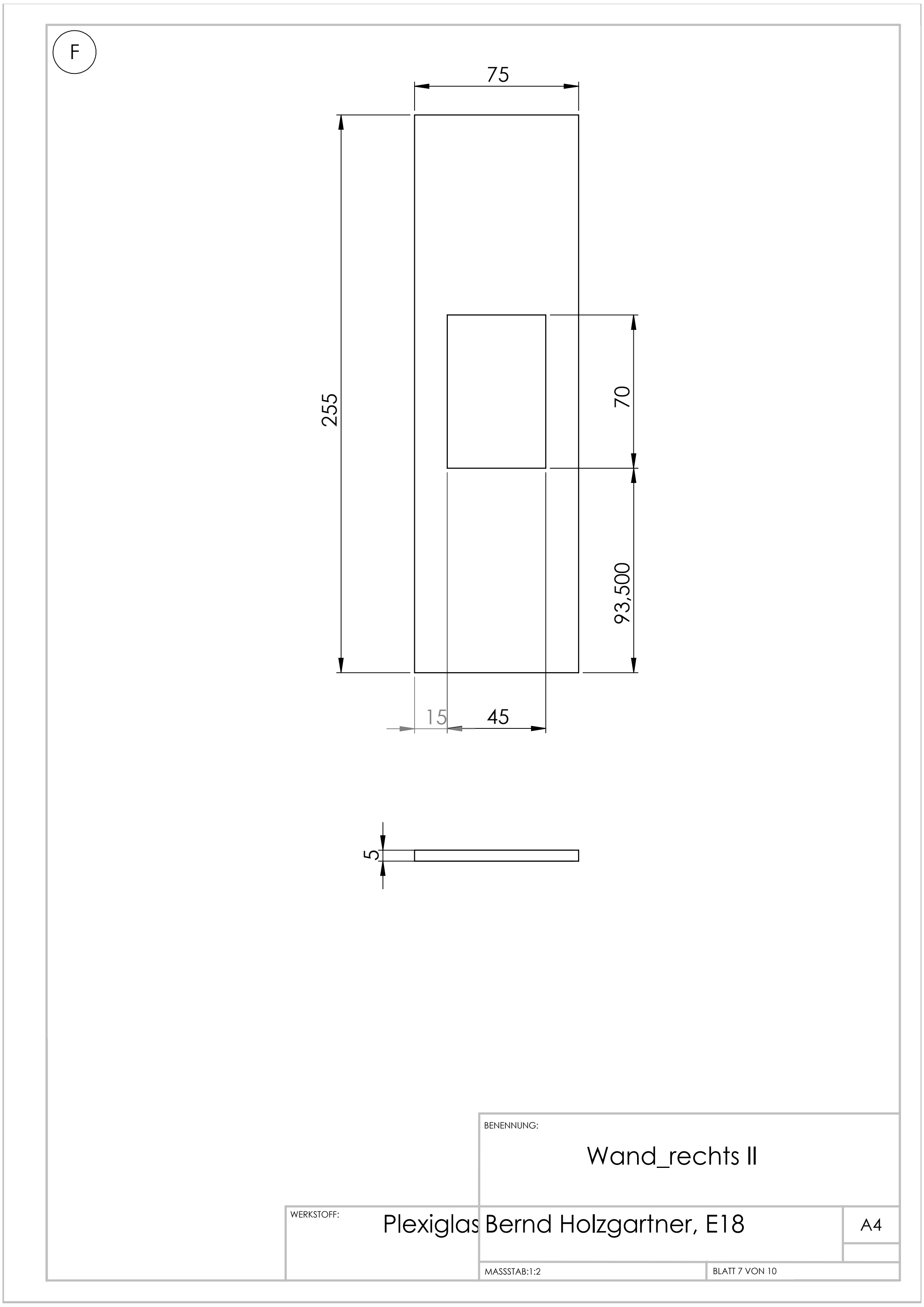
F
75
255
70
93,500
15
45
5
BENENNUNG:
Wand_rechts II
WERKSTOFF:
Plexiglas
Bernd Holzgartner, E18
A4
MASSSTAB:1:2
BLATT 7 VON 10

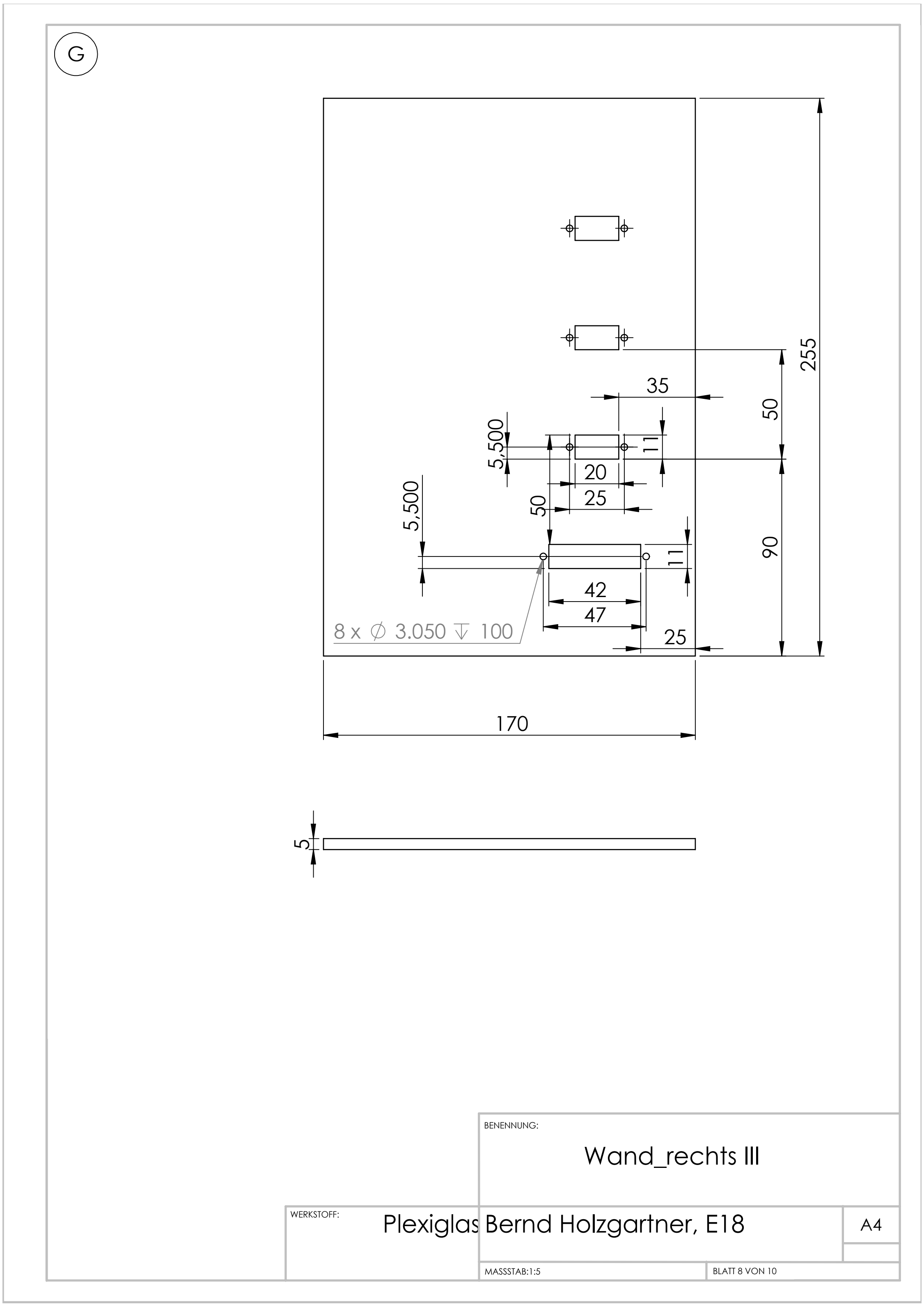
G
255
35
50
5,500
11
20
25
5,500
50
90
11
42
47
8 x ∅ 3.050 ↧ 100
25
170
5
BENENNUNG:
Wand_rechts III
WERKSTOFF:
Plexiglas
Bernd Holzgartner, E18
A4
MASSSTAB:1:5
BLATT 8 VON 10

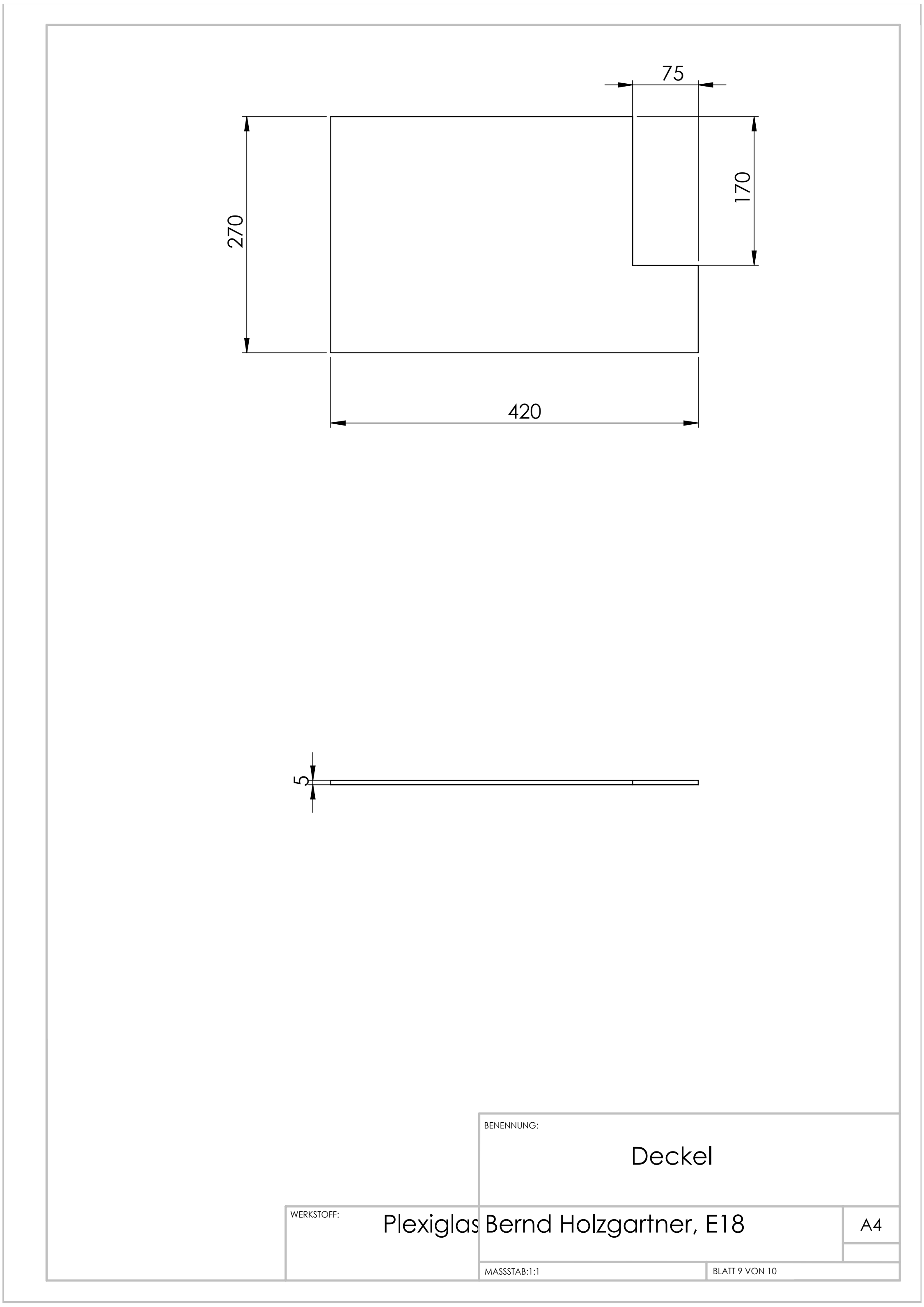
75
170
270
420
5
BENENNUNG:
Deckel
WERKSTOFF:
Plexiglas
Bernd Holzgartner, E18
A4
MASSSTAB:1:1
BLATT 9 VON 10

C. Run by run alignment

C.1. Plots

C.1.1. Silicon residuals

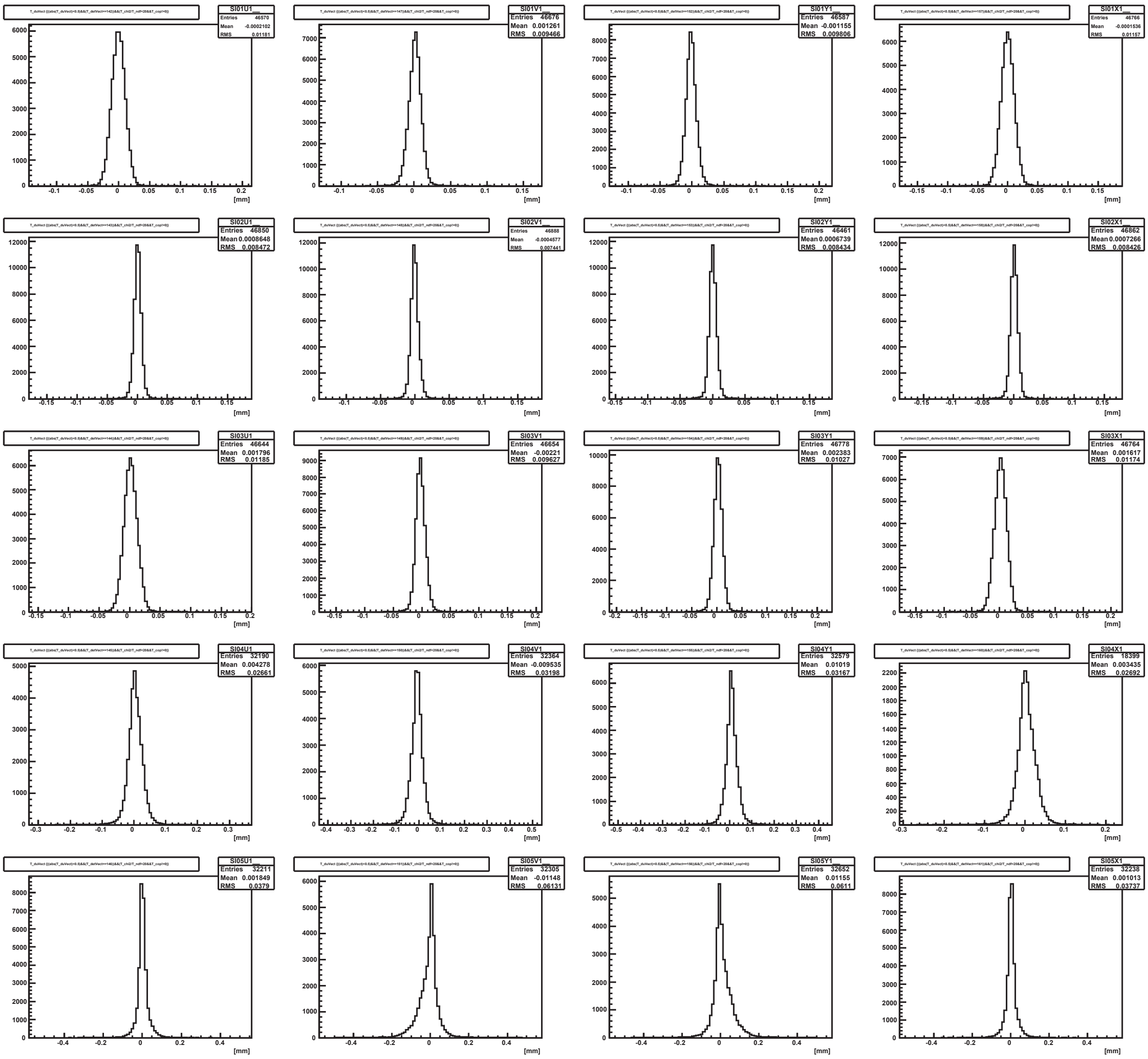

Figure C.1.: Typical residua for the individual silicon planes with muon beam (route enlargement and position uncertainty set to 0.0050 and 0.0025 respectively)

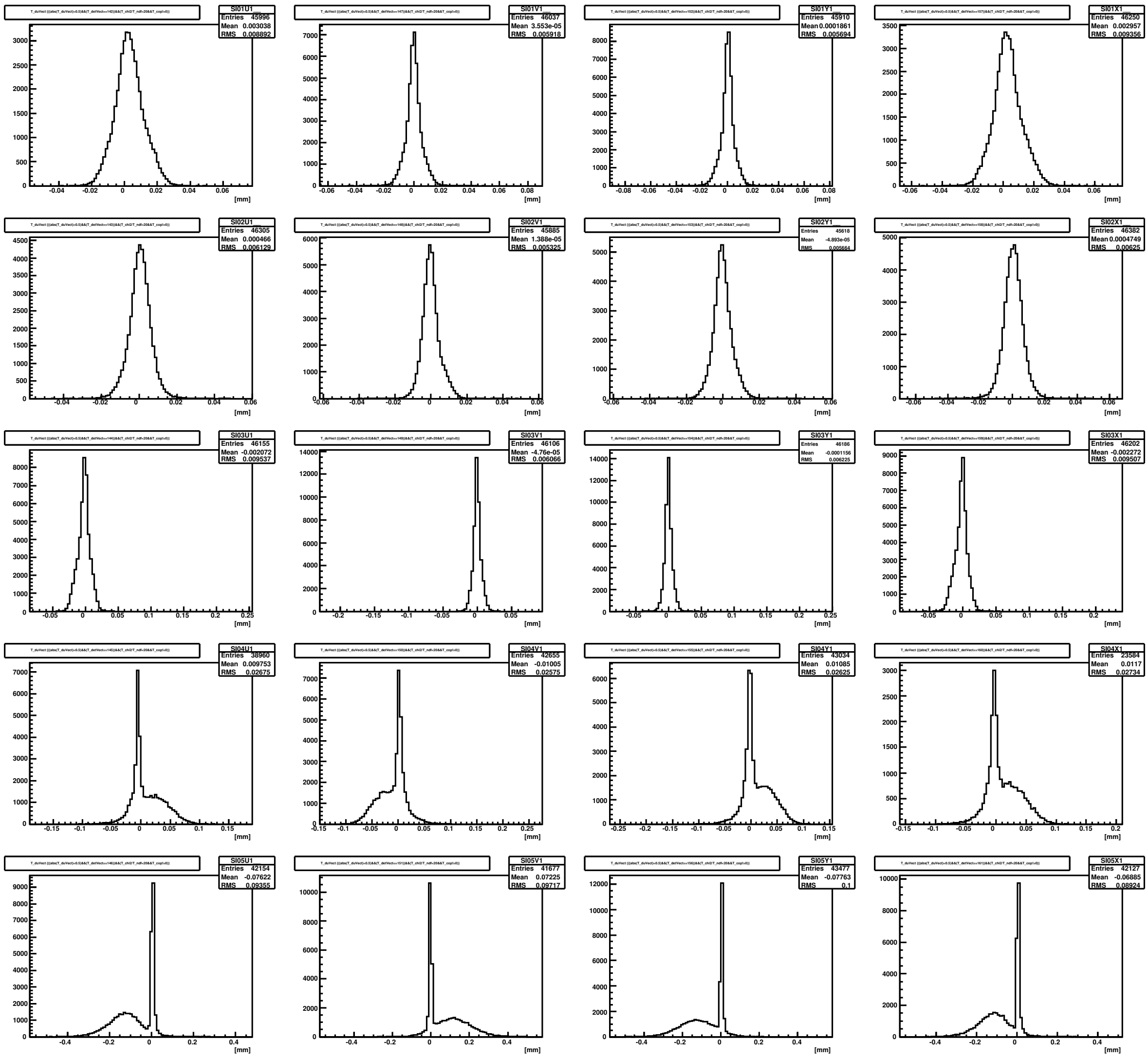

Figure C.2.: Typical residua for the individual silicon planes with muon beam (route enlargement and position uncertainty set to zero)

C.1.2. Plane shifts

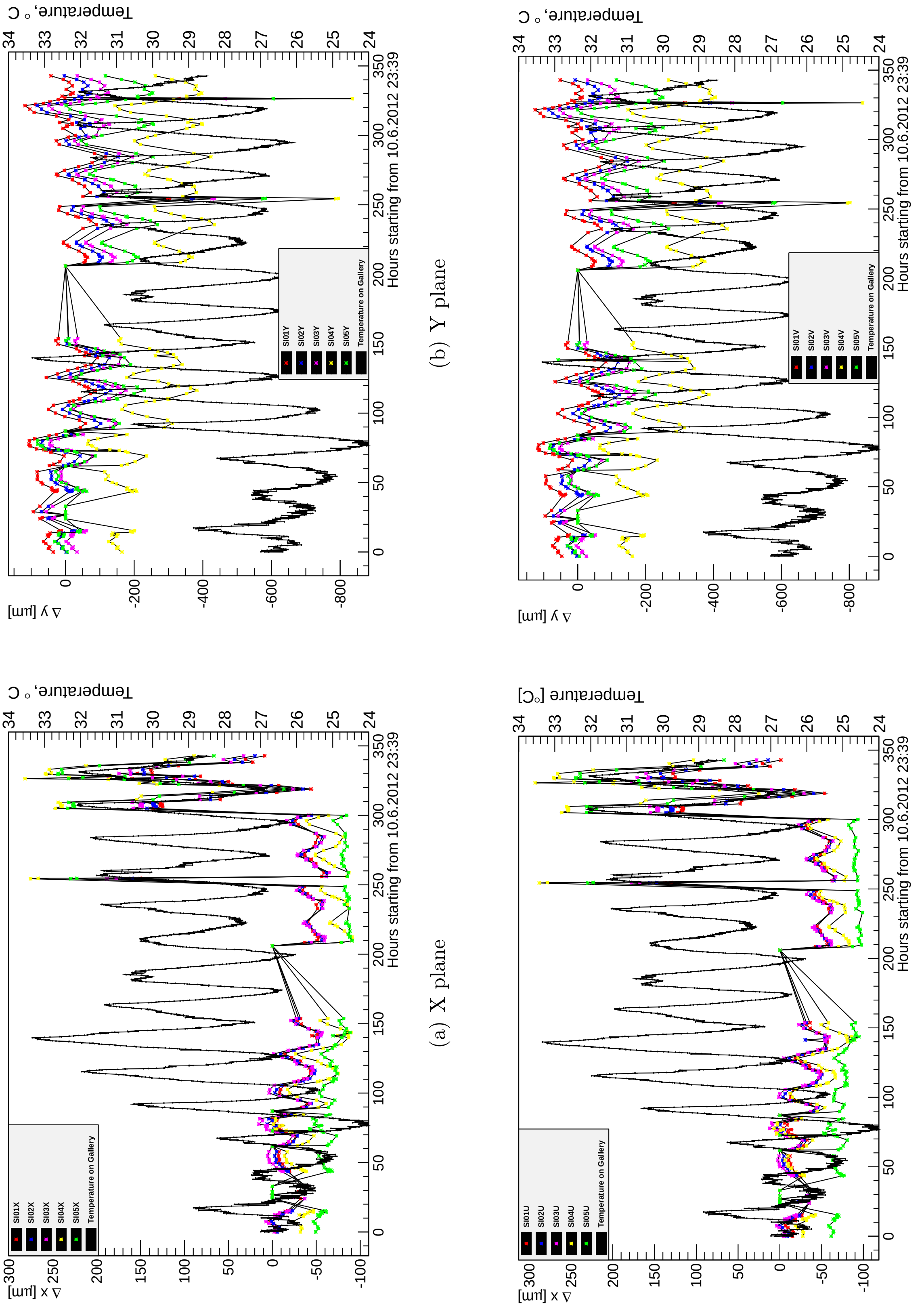

(a) X plane

(b) Y plane

(c) U plane

(d) V plane

Figure C.3.: Plane shifts W24

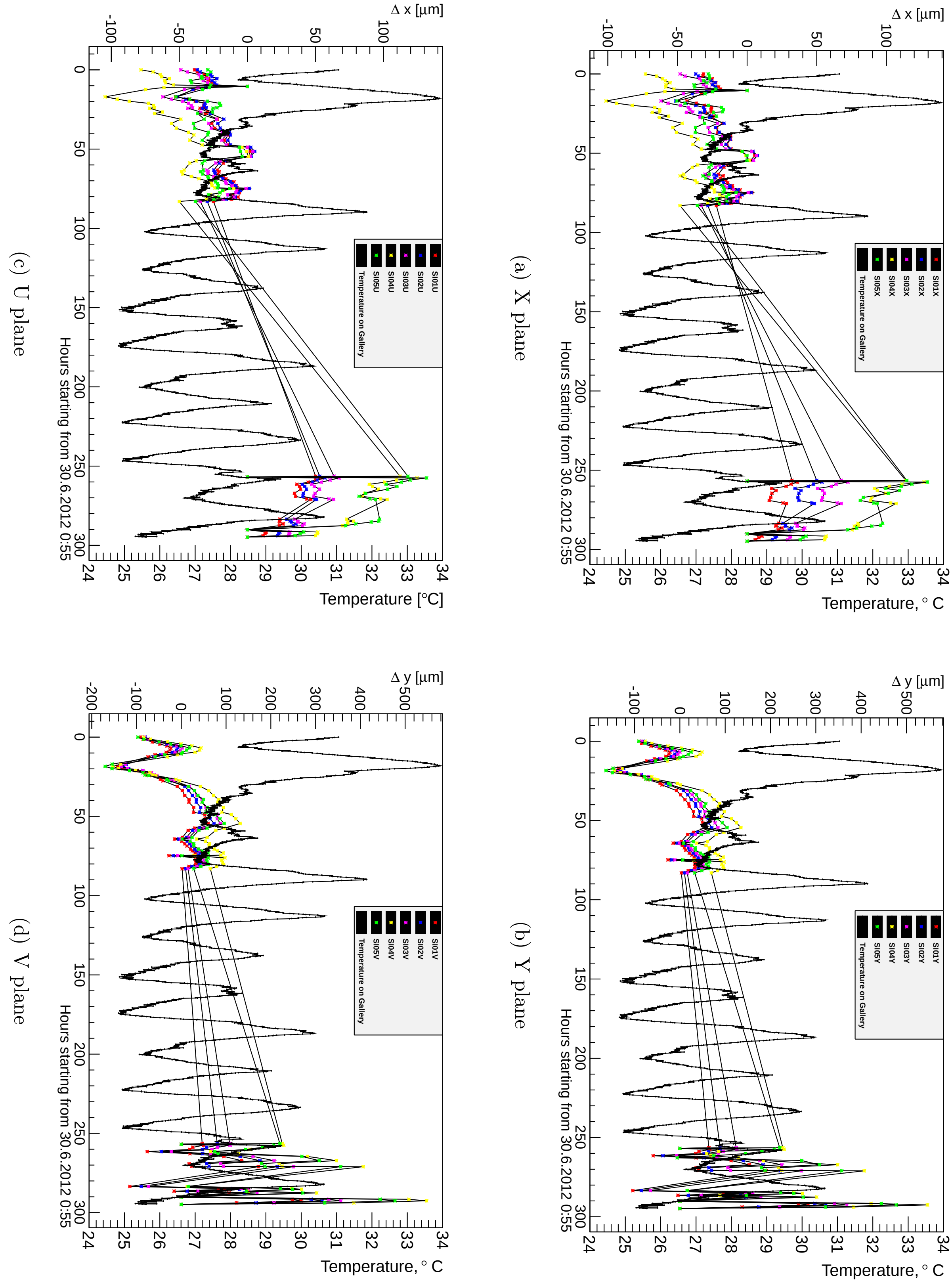

Figure C.4.: Plane shifts W26

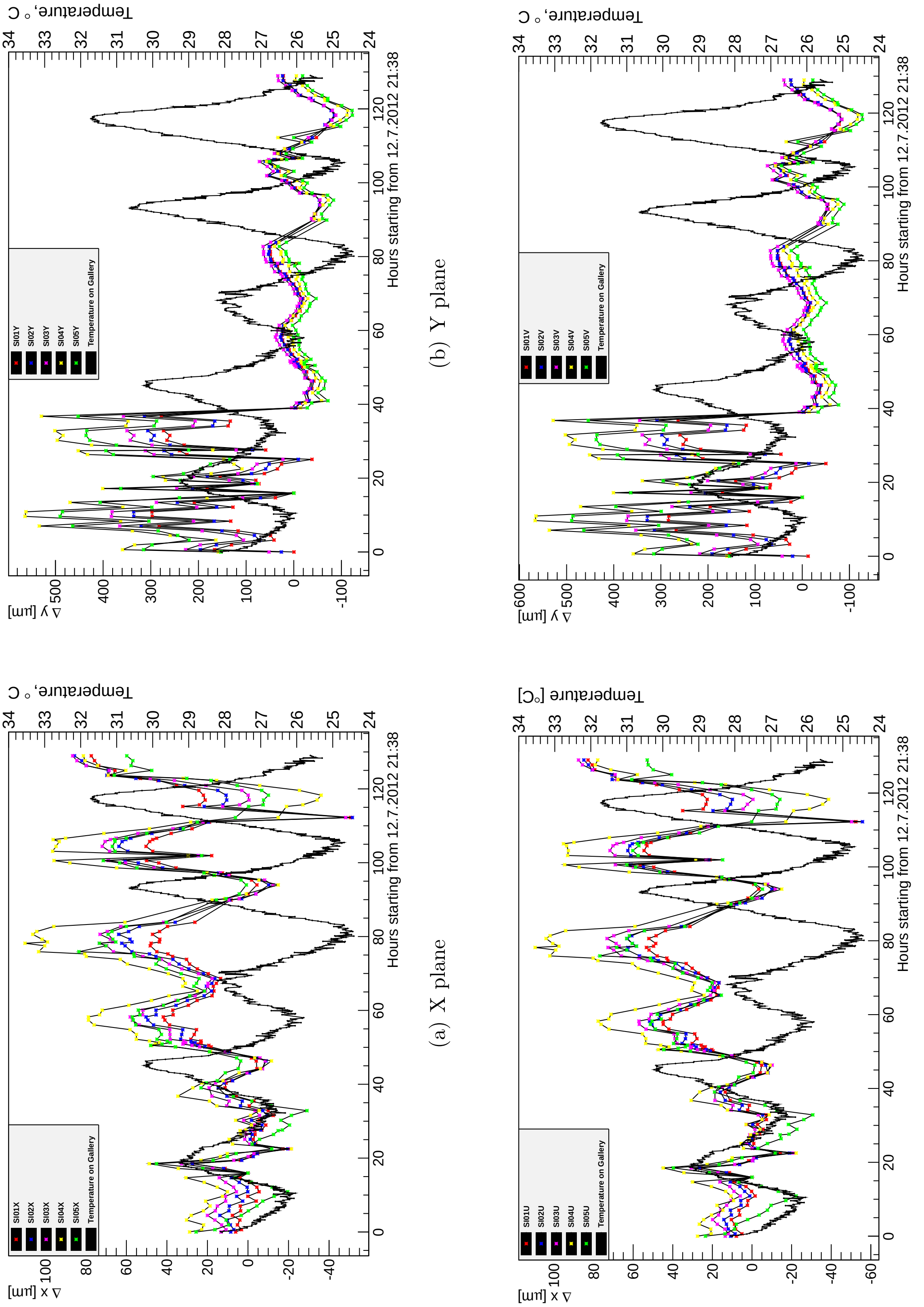

(a) X plane

(b) Y plane

(c) U plane

(d) V plane

Figure C.5.: Plane shifts W28

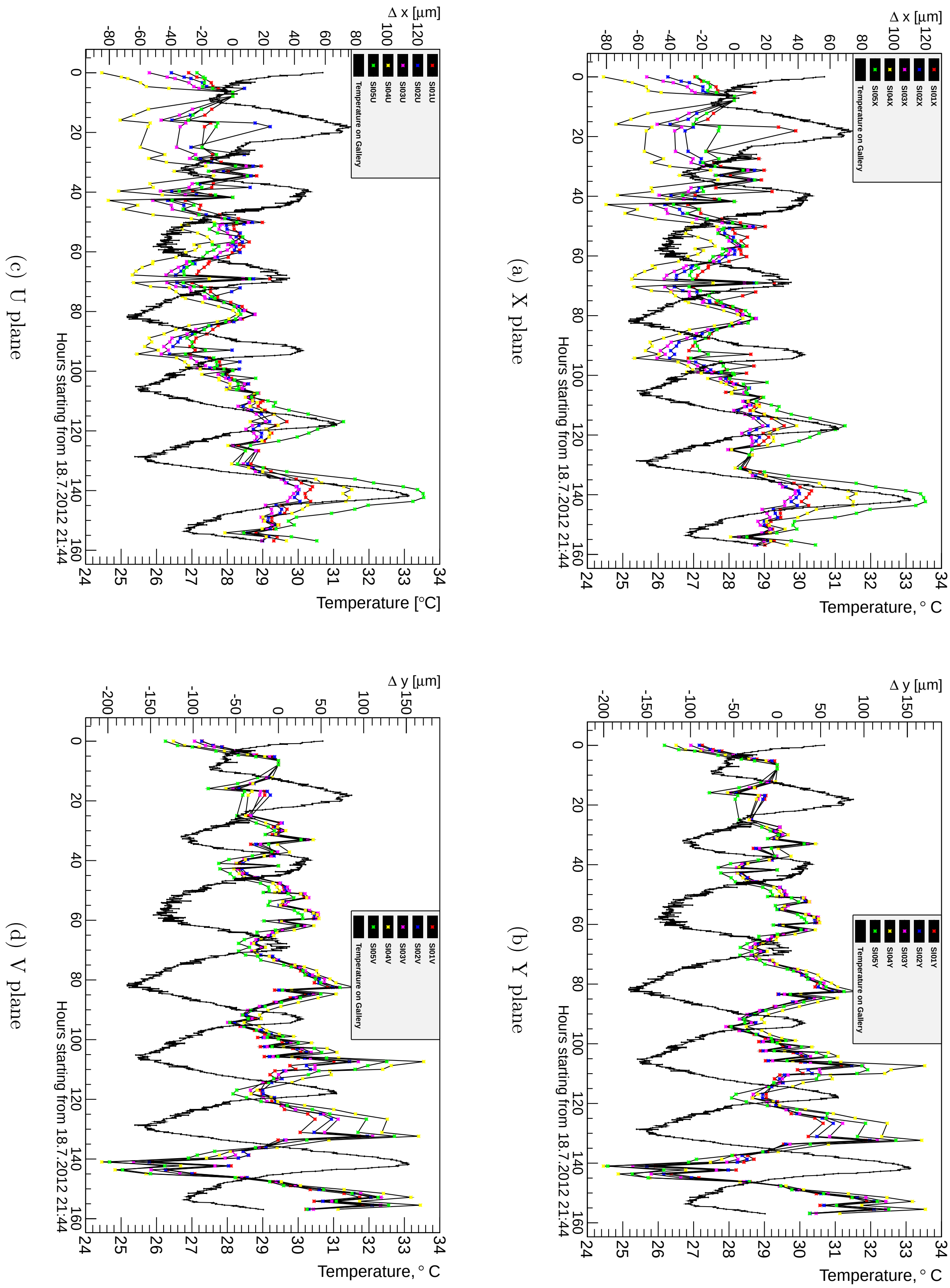

(a) X plane

(b) Y plane

(c) U plane

(d) V plane

Figure C.6.: Plane shifts W29

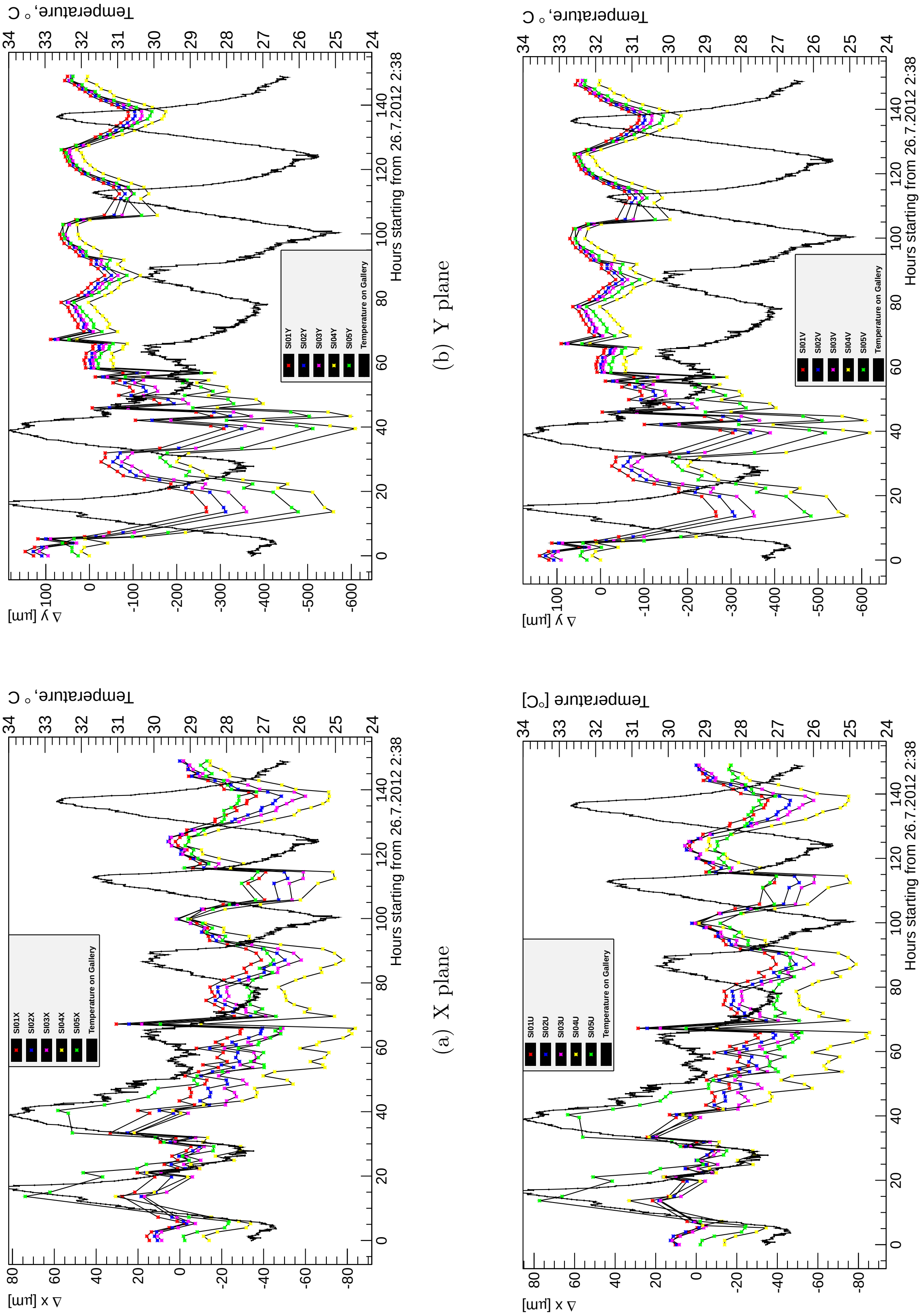

(a) X plane

(b) Y plane

(c) U plane

(d) V plane

Figure C.7.: Plane shifts W30

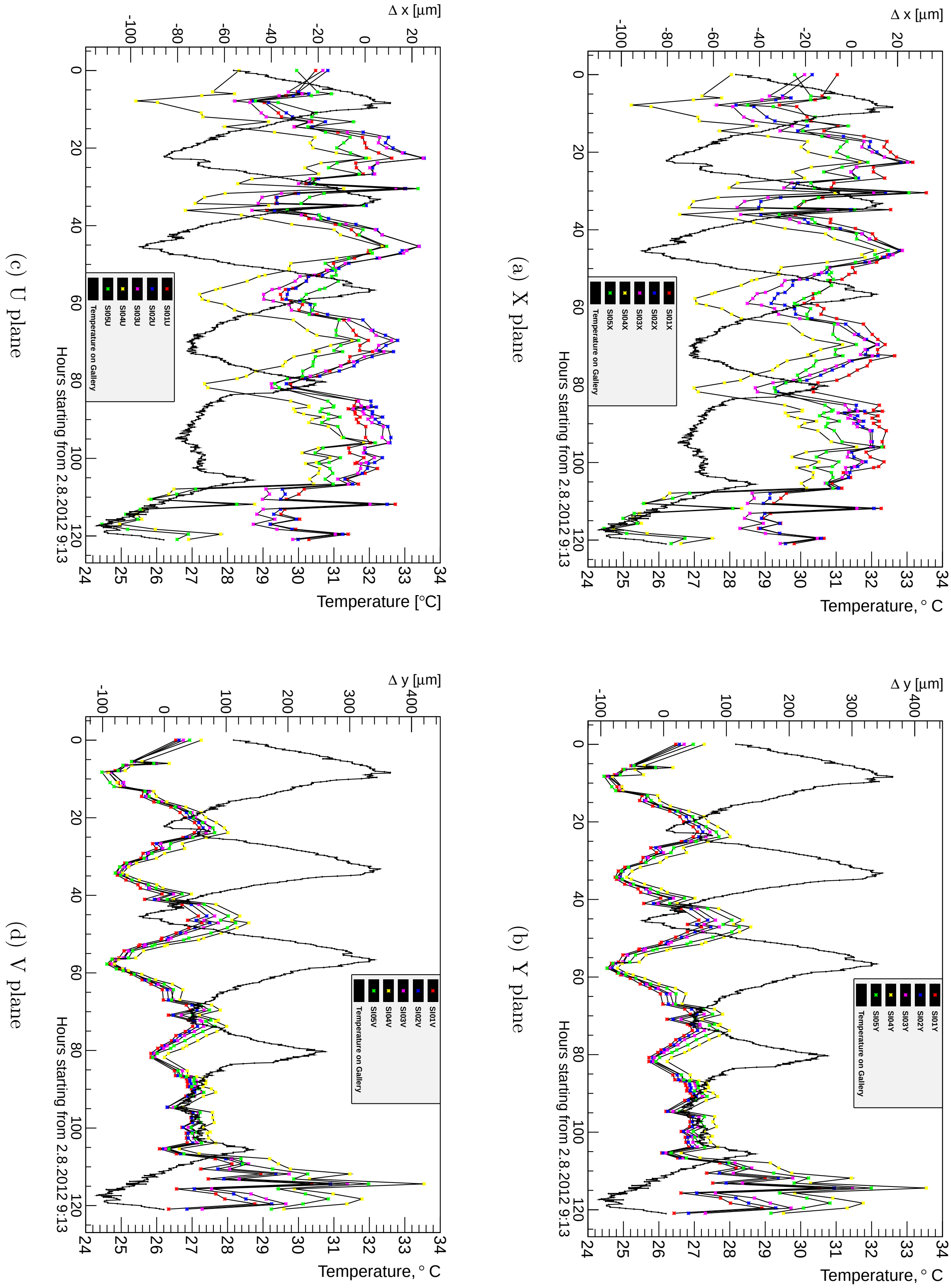

Figure C.8.: Plane shifts W31

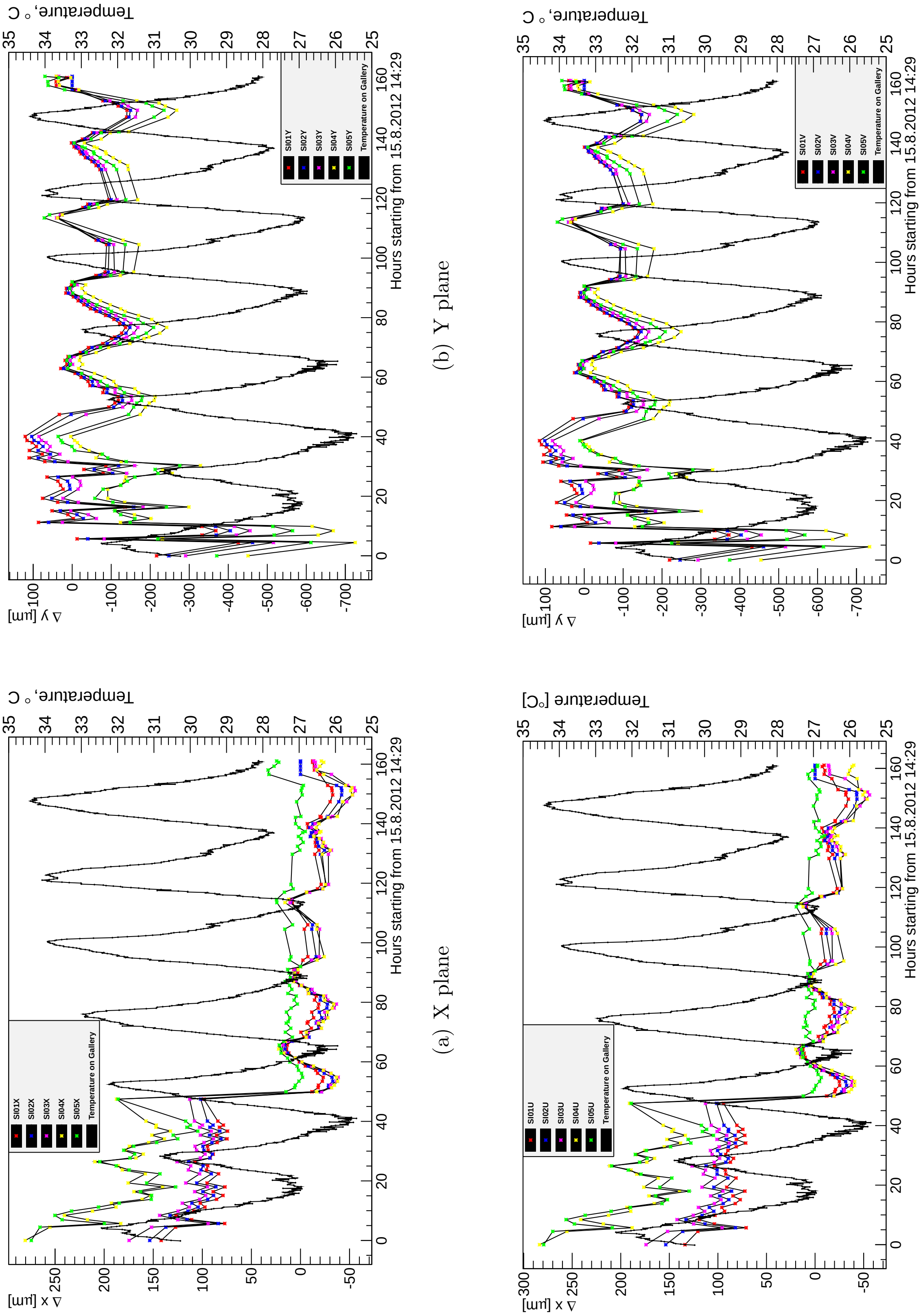

(a) X plane

(b) Y plane

(c) U plane

(d) V plane

Figure C.9.: Plane shifts W33

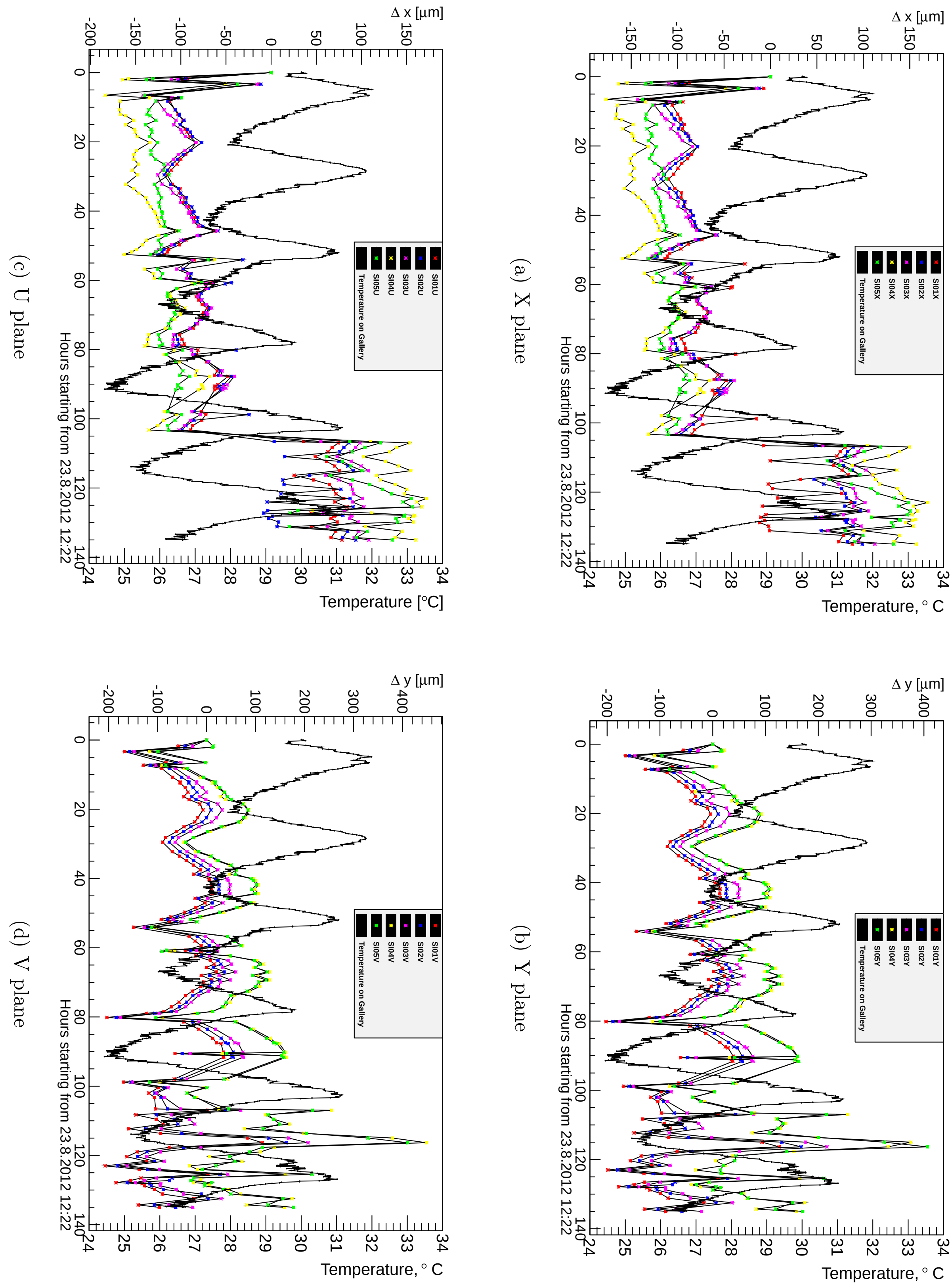

(a) X plane

(b) Y plane

(c) U plane

(d) V plane

Figure C.10.: Plane shifts W34

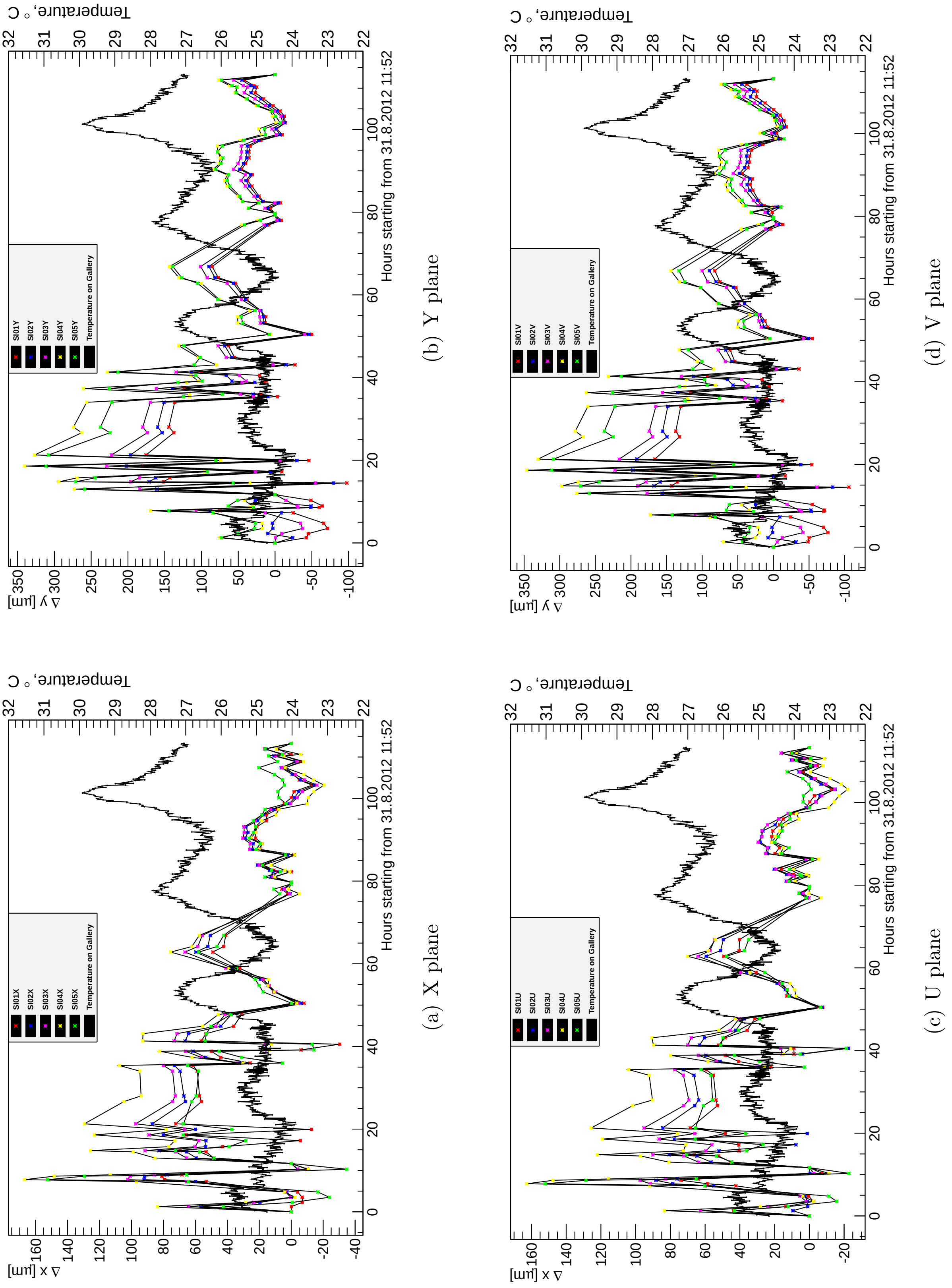

(a) X plane

(b) Y plane

(c) U plane

(d) V plane

Figure C.11.: Plane shifts W35

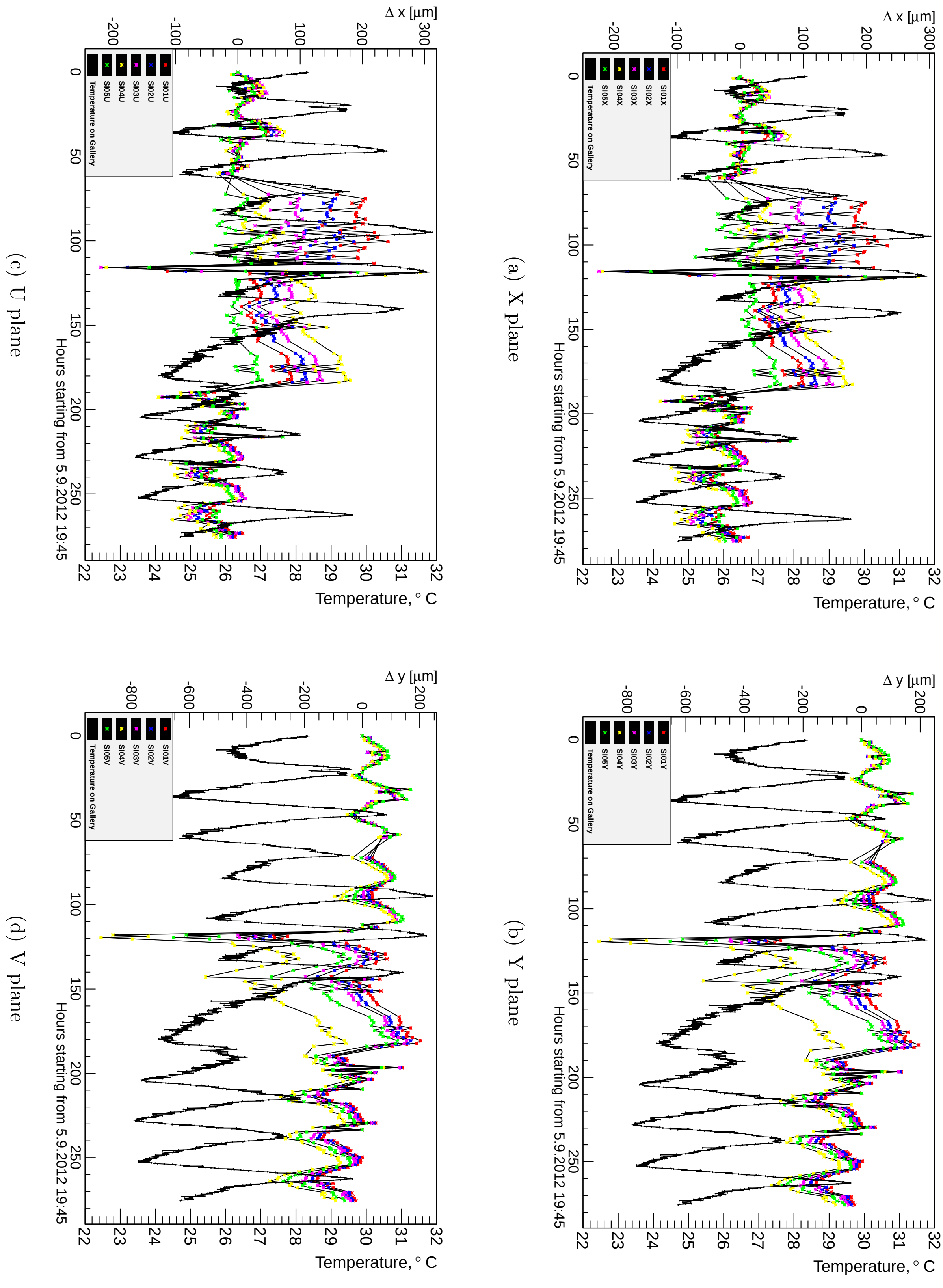

(a) X plane

(b) Y plane

(c) U plane

(d) V plane

Figure C.12.: Plane shifts W36

C.2. Option files

C.2.1. Tracking option files

The run by run alignment presented in Chapter 6 was done with modified CORAL option files. The following tables specify the changes with respect to the standard option file for the 2012 Primakoff run `trafdic.h2012.opt`.

Option	Explanation
`TraF dCut [84] .0050`	Silicon route enlargement is set to 0.0050
`TraF dCut [85] .0025`	Silicon cluster uncertainty is set to 0.0025
`TraF ReMode [26] 1`	Bridging over target ON

Table C.1.: Special options in `traf.2012.fi01.opt`

Option	Explanation
`TraF dCut [84] .0050`	Silicon route enlargement is set to 0.0050
`TraF dCut [85] .0025`	Silicon cluster uncertainty is set to 0.0025

Table C.2.: Special options in `traf.2012.phys.opt`

Option	Explanation
`TraF dCut [84] .0050`	Silicon route enlargement is set to 0.0050
`TraF dCut [85] .0025`	Silicon cluster uncertainty is set to 0.0025
`TraF DetNameOff FI01`	Fiber FI01 excluded from tracking

Table C.3.: Special options in `traf.2012.sil.opt`

C.2.2. Alignment option files

The following tables specify the dectector planes used/excluded or fixed in the various alignment steps of the run by run alignment. The z-position is fixed for all detector planes.

Option	Detector plane
`align useDets`	`SI FI`
`align excludeDets`	`FI05 FI08 DC GM GP MM MP PA PB MA MB ST DW`
`fix U`	`FI05 FI08`
`fix T`	`FI05 FI08 SI04X SI04Y`
`fix P`	`FI05 FI08 SI`

Table C.4.: Settings in `align.2012.fi01.opt`

Option	Detector plane
`align useDets`	`SI FI GM GP MM`
`align excludeDets`	`DC MP PA PB MA MB ST DW`
`fix U`	`GM04X1 GM04Y1 GM10X1 GM10Y1`
`fix T`	`GM04X1 GM04Y1 GM10X1 GM10Y1 GP**P`
`fix P`	`GM04X1 GM04Y1 GM10X1 GM10Y1 SI`

Table C.5.: Settings in `align.2012.phys.opt`

Option	Detector plane
`align useDets`	`SI`
`align excludeDets`	`FI  DC GM GP MM MP PA PB MA MB ST DW`
`fix U`	`-`
`fix T`	`SI04X SI04Y`
`fix P`	`SI01X SI01Y SI03X SI03Y`

Table C.6.: Settings in `align.2012.silicon.opt`

Bibliography

[1] The COMPASS Collaboration. A PROPOSAL FOR A COMMON MUON and PROTON APPARATUS for STRUCTURE and SPECTROSCOPY. *CERN/SPSLC 96-14 / SPSC/P 297*, 1996.

[2] CERN. Cern accelerator complex. `http://cdsweb.cern.ch/record/1260465`.

[3] P. Abbon et al. The COMPASS experiment at CERN. *Nuclear Instruments and Methods in Physics Research A, 577, 455-518*, 2007.

[4] J. Ellis and R. Jaffe. Sum rule for deep inelastic electroproductions from polarized protons. *Physical Review D9, 5*, 1974.

[5] B. Grube. *A Trigger Control System for COMPASS and A Measurement of the Transverse Polarization of* Λ *and* Ξ *Hyperons from Quasi-Real Photo-Production.* PhD Thesis, Technische Universität München, 2006.

[6] The COMPASS collaboration. Measurement of the spin structure of the deuteron in the DIS region. *Physics Letters B 612, 154-164*, 2005.

[7] The COMPASS collaboration. Spin asymmetries A_1^d and the spin-dependent structure functions g_1^d of the deuteron at low values of x and Q^2. *Physics Letters B 647, 330-340*, 2007.

[8] The COMPASS collaboration. The deuteron spin-dependent structure function g_1^d and its first moment. *Physics Letters B 647, 8-17*, 2007.

[9] The COMPASS collaboration. The polarised valence quark distribution from semi-inclusive DIS. *Physics Letters B 660, 458-465*, 2008.

[10] The COMPASS collaboration. Flavour separation of helicity distributions from deep inelastic muon-deuteron scattering. *CERN-PH-EP/2009-008*, 2009.

[11] The COMPASS collaboration. A new measurement of the Collins and Sivers asymmetry on a transversely polarized deuteron target. *Nuclear Physics B 765, 31-70*, 2007.

[12] The COMPASS collaboration. Collins and Sivers asymmetries for pions and kaons in muon-deuteron DIS. *Physics Letters B 673, 127-135*, 2009.

[13] The COMPASS collaboration. Experimental investigation of transverse spin asymmetries in muon-p SIDIS processes: Collins asymmetries. *arXiv:hep-ex/1205.5121v1*, 2012.

[14] The COMPASS collaboration. Experimental investigation of transverse spin asymmetries in muon-p SIDIS processes: Sivers asymmetries. *arXiv:hep-ex/1205.5122v1*, 2012.

[15] A.-M. Dinkelbach. *Precision Tracking and Electromagnetic Calorimetry Towards a Measurement of the Pion Polarisabilities at COMPASS*. PhD Thesis, Technische Universität München, 2011.

[16] T. Nagel. *Measurement of the Charged Pion Polarizability at COMPASS*. PhD Thesis, Technische Universität München, 2012.

[17] The COMPASS Collaboration. COMPASS-II proposal. *CERN-SPSC-2010-014 / SPSC-P-340*, 2010.

[18] T. Nakano et al. Evidence for a Narrow S=+1 Baryon Resonance in Photoproduction from the Neutron. *Phys. Rev. Lett. 91, 012002*, 2003.

[19] S.-K. Choi. Observation of a Narrow Charmoniumlike State in Exclusive $B^{\pm} \rightarrow K^{\pm}\pi^{+}\pi^{-}J/\psi$ Decays. *Phys. Rev. Lett. 91, 262001*, 2003.

[20] C. Alt et al. Evidence for an Exotic S=-2, Q=-2 Baryon Resonance in Proton-Proton Collisions at the CERN SPS. *Phys. Rev. Lett. 92 4, 042003*, 2004.

[21] The COMPASS collaboration. Search for the $\phi(1860)$ pentaquark at COMPASS. *CERN-PH-EP-2005-009.*

[22] The COMPASS collaboration. Observation of a $J^{PC} = 1^{-+}$ exotic resonance in diffractive dissociation of 190 GeV/c π^- into $\pi^-\pi^-\pi^+$. *Phys. Rev. Lett., 104(24), 241803*, 2010.

[23] P. Abbon et al. The COMPASS Setup for Physics with Hadron Beams. To be published.

[24] A. Austregesilo. Commissioning and Performance of a Prototype PixelGEM Detector for COMPASS. Diploma Thesis, Technische Universität München, 2007.

[25] S. Huber. Development of a digital trigger for electromagnetic calorimeter. Diploma Thesis, Technische Universität München, 2010.

[26] T. Nagel. Cinderella: an online filter for the COMPASS experiment. Diploma Thesis, Technische Universität München, 2005.

[27] CERN. The root webpage. `http://root.cern.ch`.

[28] W. R. Leo. *Techniques for Nuclear and Particle Physics Experiments.* Springer-Verlag, 1994.

[29] J. Friedrich. Private communications.

[30] R.M. Wagner. Commissioning of Silicon Detectors for the COMPASS Experiment at CERN. Diploma Thesis, Technische Universität München, 2001.

[31] K. Borer et al. Charge collection effciency of irradiated silicon detector operated at cryogenic temperatures. *Nuclear Instruments and Methods in Physics Research A, 440, 5-16*, 2000.

[32] K. Bicker. Construction and commissioning of a cooling and support structue for the silicon detectors for the COMPASS experiment. Diploma Thesis, Technische Universität München, 2011.

[33] P. Zimmerer. Performance of cryogenic silicon microstrip detectors at the COMPASS experiment. Diploma Thesis, Technische Universität München, 2011.

[34] R. H. Richter et al. Strip detector design for ATLAS and HERA-B using two-dimensional device simulation. *Nuclear Instruments and Methods in Physics Research A, 377, 412-421*, 1996.

[35] I. Abt et al. Double-sided microstrip detectors for the high radiation environment in the HERA-B experiment. *Nuclear Instruments and Methods in Physics Research A, 439, 442-450*, 2000.

[36] W. Schmidt-Parzefall. HERA-B: An Experiment to study CP violation at the HERA proton ring using an internal target. *Nuclear Instruments and Methods in Physics Research A, 368, 124-132*, 1995.

[37] V. M. Pugatch et al. Radiation hardness of the HERA-B silicon microstrip detectors. *Il Nuovo Cimento A, 112, 1383-1390*, 1999.

[38] I. Abt et al. Irradiation tests of double-sided silicon strip detectors with a special guard ring structure. *IEEE Transactions on Nuclear Science, 43, 1113-1118*, 1996.

[39] L. L. Jones et al. Design and results from the APV25, a deep sub-micron CMOS front-end chip for the CMS tracker, 2001.

[40] M. Leeb. Optimization of the Clustering and Tracking Algorithms of the Silicon Microstrip Detectors for the COMPASS Experiment. Diploma Thesis, Technische Universität München, 2011.

[41] L. L. Jones. *APV25-S1 User Guide - Version 2.2.* `http://cdsweb.cern.ch/record/1069892/files/cer-002725643.pdf`.

[42] Bibus Metals AG. *MONEL® Alloy 400 datasheet.*

[43] B. Grube. The Trigger Control System and the common GEM and Silicon Readout for the COMPASS Experiment. Diploma Thesis, Technische Universität München, 2001.

[44] M. Wiesmann. *A Silicon Microstrip Detector for COMPASS and a first Measurement of the transverse Polarization of L-Hyperons from quasi-real Photo-Production*. PhD Thesis, Technische Universität München, 2004.

[45] UHU GmbH & Co. KG. *UHU plus endfest 300 datasheets*.

[46] S. Grabmüller. Private communications.

[47] W. Polifke and J. Kopitz. *Wärmeübertragung*. Pearson Studium, 2005.

[48] P. Abbon et al. Read-out electronics for fast photon detection with COMPASS RICH-1. *Nuclear Instruments and Methods in Physics Research A, 587, 371-387*, 2008.

[49] Honeywell. *LLE 101000 data sheet*.

[50] H. Pereira and J.-M. Le Goff. Compass spectrometer alignment. *COMPASS Note 2003-4*, 2003.

[51] J.-C. Gayde. COMPASS POSITION OF SI RAILS AND DETECTORS. `https://edms.cern.ch/file/1221874/1/COMPASS_SI_SIRails_06Mar2012.pdf`.

[52] V. Blobel and C. Kleinwort. A NEW METHOD FOR THE HIGH-PRECISION ALIGNMENT OF TRACK DETECTORS. *arXiv:hep-ex/0208021*, 2002.

[53] A. Austregesilo. Private communications.

[54] T. Stempfle. Private communications.

Own contributions

This thesis was created at the chair of Prof. Stephan Paul at the Technische Universität München within the framework of the COMPASS experiment at CERN, Geneva.

I started my thesis in November 2011, already familiar with the silicon hardware from one and half year's time as a technical student, with working on an improved phase separator for the silicon stations. In November, I participated in the dismounting of the silicon stations at CERN after the 2011 run under the direction of Karl Bicker. Furthermore, I assisted Karl Bicker and Cedric Pedron (CEA Saclay) in implementing a new fill regulation for the Valve Box at COMPASS.

The work on an improved separator was based on the separator which was introduced by Karl Bicker in his diploma thesis and resulted, after several months of preparatory work, in the modular Phase Separator. The phase separator was operated successfully and may be used for the silicon detectors at COMPASS. Moreover, further possible improvements of the present design have been proposed.

In parallel, I started working on the water cooling system for the repeater cards of the COMPASS silicon microstrip detectors, which was inspired by the cooling system of the front-end electronics of the RICH detector at COMPASS. With this PLC-controllable cooling system, it is now possible to keep the repeater cards at a constant temperature level all over the year and to easily control the system via the ANIBUS-system, which is already used for controlling and monitoring the cooling of the silicon microstrip detectors with liquid nitrogen.

During spring 2012 I spent eight weeks at CERN (and many more days in Munich) in order to prepare and install the upstream stations and the conical cryostat at COMPASS. I further took my shift- and GEMSi-On-Call-duties during that time. Throughout the whole beam time in 2012 I shared the responsibility for the CryoSil-On-Call service with Karl Bicker. In September and October, I spent two more weeks at CERN for dismounting and re-installing the silicons during the changeover from the Primakoff to the DVCS spectrometer set-up.

From May on, I was doing the alignment of the COMPASS spectrometer for the Primakoff program as well as the run by run alignment of the silicon detectors under the supervision of Alex Austregesilo. I further did the time calibration for the COMPASS silicon microstrip detectors in 2012.

Acknowledgments

First of all I would like to thank Prof. Stephan Paul for giving me this interesting subject. I really enjoyed working in his group.

Big thanks go to Dr. Jan Friedrich and Dr. Stefanie Grabmüller for sharing their tremendous knowledge about COMPASS and silicon detectors with me. Furthermore, I kindly acknowledge the valuable input of Dr. Friedrich for the phase separator and his persistency. His believe in the phase separator project ultimately made it a success. Special thanks go to Dr. Grabmüller for her assistance with the time calibration for the silicon detectors.

I gratefully acknowledge the help of Karl Bicker. Whenever being at CERN, he was a great help with his knowledge about COMPASS and the silicon detectors. Furthermore, I would like to thank him for his support on the water cooling system; especially for the lessons on PLC programming.

I further want to thank Cedric Peron and Jean-Yves Rousse from CEA Saclay for the implementation of the PLC code of the water cooling system.

Special thanks go to Alex Austregesilo for introducing me to the spectrometer alignment and always being a helpful source of information and solutions for all kinds of problems.

All the technical students who worked with me on this project did a tremendous job and I thank them all for their effort.

My sincerest thanks go to Alex Austregesilo, Karl Bicker and Dr. Friedrich for proofreading this thesis.

Last but not least I would like to thank my parents for their support.